Thermoresponsive Behaviour of Selected Mixed Metal Oxides

Michelle Sibonokuhle Nyoni

A dissertation submitted in fulfillment of the requirements for the degree of Master of Science to the Faculty of Science, University of Witwatersrand, Johannesburg

Supervisor: Prof. D.G. Billing

Co-Supervisor: Dr. P.J. Franklyn

School of Chemistry

September 2013

Declaration

I declare that this thesis is my own unaided work. It is being submitted for the Degree of Master of Science in the University of Witwatersrand, Johannesburg. It has not been submitted before for any degree or examination in any other University

……...

Signature of Candidate

on the…….day of……..2013 at……

Abstract

Low-to-negative thermal expansion is an important property for materials in a wide range of applications including space applications, microwave components, construction, mirrors, dental fillings and high precision ion dilatometers. Powder X-ray diffraction (PXRD) has been used to investigate the thermoresponsive behavior of $Nb_{6.7}W_{10.3}O_{47}$, $Ta_{14.8}W_{1.2}O_{46}$, $Ta_{16}W_{18}O_{94}$ and $BaPbO_3$.

Calibration and benchmarking of the diffractometer was performed to ensure accurate results are obtained. Continuous Online X-ray Analysis (COXA) enabled the close monitoring of phase transitions, changes in any lattice parameters in response to thermal stimuli. When COXA is coupled with Rietveld refinement, coefficients of thermal expansion (CTE) could be determined accurately.

The tungstates were synthesized using a precipitation reaction and heat treatment from chlorides of the metals ($NbCl_5$; $TaCl_5$) and tungstic acid (H_2WO_4). The products, $Nb_{6.7}W_{10.3}O_{47}$, $Ta_{14.8}W_{1.2}O_{46}$ and $Ta_{16}W_{18}O_{94}$, underwent a COXA analysis within the temperature range 30 ˚C to 900 ˚C.

$Nb_{6.7}W_{10.3}O_{47}$ has a mean volumetric CTE of 6.704 x 10^{-6} ˚C^{-1}, and therefore has low positive thermal expansion. The tantalum tungstates were found to have low positive thermal expansion as well. $Ta_{14.8}W_{1.2}O_{46}$ and $Ta_{16}W_{18}O_{94}$ have mean volumetric CTEs of 2.101 x 10^{-5} ˚C^{-1} and 9.851 x 10^{-6} ˚C^{-1}.

$BaPbO_3$ underwent two phase transitions between 30 ˚C and 550 ˚C from orthorhombic Imma to I4/mcm to cubic Pm-3m. The transition from Imma to I4/mcm took place at 270 ˚C. The phase transition from I4/mcm to Pm-3m took place at 390 ˚C.

“*In loving memory of my mother, Senzeni Ndlovu*”

Acknowledgements

I would like to express my deepest gratitude to the following groups of people as they journeyed and assisted me with this research. It would not have been possible without you.

- My supervisor, Dave G. Billing and co-supervisor Paul J. Franklyn for challenging and believing in me. Thank you for introducing me to the awesome technique that is PXRD.
- My dad, Ndabanengi B. Nyoni, for encouraging me to realize my own potential and to utilize the opportunities that I have been given.
- My colleagues in the XRD group, Natsayi, Hazel, Wilson, Rob and Kersty. Thank you for putting up with me.
- The LOONIES Gatehouse group for open doors when I needed a different opinion or just needed to talk.
- My friends who are just too many to name. Thank you for your continued support, love and prayers.
- My mini-army of proofreaders, Soon Jong, Andrew, Natsayi and Samantha. Thank you for your commitment and meticulous attention to detail.
- My family which is also too big to name individually. Thank you for your support.
- To the Lord Almighty for His constant love, strength and grace that He constantly lavished upon me.
- The School of Chemistry and the University of Witwatersrand for providing the facilities for this research.
- The DST/NRF Centre of Excellence in Strong Materials (CoESM) for the financial assistance.

Table of Contents

List of Figures

List of Tables

Glossary of Abbreviations

AS	Atmospheric Sintered
CIF	Crystallographic Information File
COXA	Continuous Online X-ray Analysis
CTE	Coefficient of Thermal Expansion
GOF	Goodness of Fit
GSAS	General Structure Analysis System
HP	Hot Pressed
HWHM	Half Width Half Maximum
ICDD	International Center for Diffraction Data
ICSD	International Crystal Structure Database
LTE	Low Thermal Expansion
NIST	National Institute of Standards
NTE	Negative Thermal Expansion
PDF	Powder Diffraction File
PSD	Point Source Detector
PXRD	Powder X-ray Diffraction
RHP	Reactive Hot Pressed
SC-XRD	Single Crystal X-ray Diffraction
SOP	Standard Operation Procedures
TTB	Tetragonal Tungsten Bronze
VT-PXRD	Variable Temperature Powder X-ray Diffraction
XRD	X-ray Diffraction
ZTE	Zero Thermal Expansion
3D	3-dimensional

Chapter One: INTRODUCTION

Thermoresponsive behaviour of materials is interesting and leads to a wide range of applications. This study will be looking at the thermoresponsive behaviour of some selected mixed metal oxides. The selected mixed metal oxides studied are barium plumbate, niobium tungstate and tantalum tungstates. These were suspected to possess low-to-negative thermal expansion. In situ Variable Temperature Powder X-ray Diffraction (VT-PXRD) is the technique used to investigate the thermoresponsive behaviour. Possibly the most unique or counter-intuitive thermoresponsive behaviour is negative thermal expansion.

This chapter introduces the concept of thermal expansion with reference to the applications and importance of this property.

1.1 Thermal Expansion

Almost all known materials respond through some physical change to thermal stimulation (Forbes, 2011). The enhanced amplitude of thermal vibration at higher temperatures is one of the reasons why solids expand on heating (Cahn, 1997). Formally the coefficient of thermal expansion (hereafter referred to as CTE), α, is the change in volume or linear dimension per degree of change in temperature (Chu et al., 1986a). Thermal expansion is an important inter-atomic potential dependent physical property as it is closely related to thermal shock resistance of materials.

Cracking due to thermal changes is a real problem in industry and therefore low thermal expansion is very important. The crack formation observed in brittle materials result

from anisotropic thermal expansion and thermal shock (Wolfenstine, 1998). Thermal shock resistance is inversely proportional to the CTE. Hence, the higher the CTE the poorer the thermal shock resistance of the material. Rapid heating or cooling will result in cracks due to the resultant temperature gradients that form. Reduction of temperature gradients assists in decreasing the stresses and thermal distortion within a structure (Chu et al., 1986a).

Grain size is an important property as microcracking occurs until a particular critical grain size. Beyond this critical grain size, microcracking will not be observed (Wolfenstein, 1998). Microcracking may also be caused by large anisotropic thermal expansion and this leads to hysteresis loops being observed with low thermal expansion curves. These hysteresis loops, with low thermal expansion, occur because of formation and healing of internal microcracks. Although the presence of hysteresis loops is from the formation and healing of internal microcracks, low thermal expansion is the cause of microcrack formation. It was observed that hysteresis was eliminated when there was controlled grain growth (Wu et al., 1987).

Materials which expand on heating have a positive thermal expansion coefficient and conversely those that ‘contract’ on heating have a negative thermal expansion. Isotropic expansion is observed when a material expands evenly with respect to all crystallographic axes when heated, as is normally seen in cubic materials. When materials expand to different extents, this is known as anisotropic expansion.

Some of the material compounds that have been used as thermal-shock-resistant materials include aluminium titanate, cordierite and spodumene ceramics (Wu et al.,

1987). Aluminium titanate ceramics are appropriate for use as thermal-shock-resistant materials because they have a negligible thermal expansion coefficient, excellent chemical resistance and low thermal conductivity and have been used in diesel engine exhaust systems as soot particulate filters (Barrios de Arenas, 2012; Kim, 2010) . Cordierite and spodumene have been used in ceramic cookware as thermal-shock-resistant materials. The properties that make these compounds appropriate include their low coefficient of thermal expansion, reasonable cost and low water absorption to name a few (Junlar et al., 2011).

Formally the CTE is defined as follows:

Coefficient of linear thermal expansion:

$$\boldsymbol{\sigma_m} = \frac{(\frac{L_2 - L_1}{L_0})}{T_2 - T_1} \qquad (1.1)$$

$$= \frac{1}{L_0} (\frac{\Delta L}{\Delta T}) \qquad \text{where L = length and T = temperature}$$

Coefficient of volumetric expansion:

$$\boldsymbol{\alpha} = \frac{1}{V} (\frac{\delta V}{\delta T})_p \qquad (1.2)$$

where V = volume and T = temperature and subscript p = constant pressure (Hahn, 1970; Makhura, 2009)

Dilatometry and X-ray Diffraction (XRD) are two of the techniques that are used for the determination of thermal expansion of materials (Holcombe, 1980; Wu et al., 1987). It is important to know the coefficients of thermal expansion of materials as this may lead to

a wide range of interesting and important applications as has been shown with materials like aluminium titanate, cordierite and spodumene.

1.1.1 Negative Thermal Expansion (NTE)

Negative thermal expansion is when a material contracts when thermal stimulation is applied. This phenomenon is also known as thermal contraction (Cahn, 1997). The most well known example of NTE is the increase in the density of water between 0 and 4 ˚C. When a graph of the density of water versus temperature is plotted, the CTE is obtained from the gradient of this graph. The gradient for the temperature from 4 ˚C to 0 ˚C is seen to be less than zero and therefore this confirms that water experiences negative thermal expansion. This property is critical to the livelihood and preservation of aquatic life during very cold weather (Barrera et al., 2005; Balashov & Orlov, 1983). An example of the use of negative thermal expansion is seen in the fitting of a fastener. The fastener can be heated and inserted into a hole and when it cools down, it will expand to fill the hole as long as the material used to make the fastener has negative thermal expansion (Sigmund & Torquato, 1996).

Thermal contraction is a function of structure and not necessarily the chemical constitution of a material. Many of the most interesting examples happen at very low temperatures and only become observable after the development of highly sensitive techniques of measurement (Barrera et al., 2005). When negative thermal expansion is based on the unit cell dimensions decreasing as temperature increases, this is called intrinsic NTE. This may be either isotropic or anisotropic, i.e. the contraction observed

may occur in either one, two or in all three crystal dimensions. Crystallites with highly anisotropic thermal expansion may undergo an overall negative thermal expansion though the unit cell actually increases with temperature. When these crystallites are consolidated at high temperatures, microcracks form on cooling. These microcracks reclose on heating and this leads to extrinsic negative thermal expansion (Sleight, 1998). Anisotropic NTE is observed when during heating, unit cells of materials are actually expanding in some directions, while contracting in other directions. This results in an overall small volume contraction with increasing temperature (Korthuis et al., 1995).

Sleight (1998) suggested four mechanisms by which intrinsic negative thermal expansion in oxides can occur. The first mechanism accounts for the NTE behaviour that has been observed in some AMO_3 oxides with perovskite structures, just below their cubic-to-tetragonal phase transitions. In this region, the polyhedra become more regular with increasing temperature and therefore the average metal-oxygen (M-O) distances in the polyhedra decreases (Sleight, 1998). Less anion-anion repulsions are experienced as the polyhedral become more regular.

The second mechanism relates to the normal positive thermal expansion of some specific M-O bonds. The common factor observed in the materials with this mechanism is that they have hexagonal structures and therefore show anisotropic thermal expansion. This mechanism can explain expansion in one or two dimensions but there are no known examples showing this leading to a negative volume thermal expansion based on unit cell changes (Sleight, 1998).

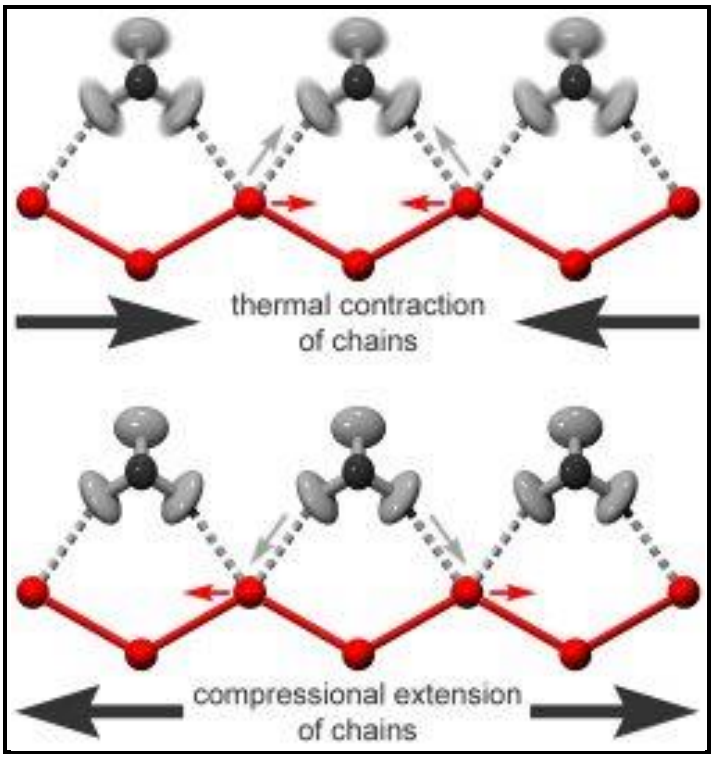

<u>Figure 1.1:</u> Illustration of how anisotropic thermal expansion occurs with methanol monohydrate. Molecules shown vibrating as there is thermal contraction of the chains leading to negative thermal expansion (Anisotropic Thermal Expansion, 2013).

The third mechanism is based on interstitial cations changing sites as a function of temperature within a network. Important factors associated with this mechanism include ionic conductivity as well as the relationship between the locations of the interstitial cations as a function of temperature (Sleight, 1998).

The final mechanism proposed in literature depends on the transverse thermal motion of oxygen in M-O-M linkages (Sleight, 1998). At low temperatures the O-O distance in CO_2 decreases with increasing temperature due to the bending mode in this molecule. Similarly metal-oxygen-metal (M-O-M) units can decrease in the M-M distance with increasing temperature (Korthuis et al., 1995). Sufficiently strong M-O bonds will show

negligible thermal expansion. Oxygen's average displacement increases with temperature and therefore in such a strongly bonded unit, the vibration of oxygen is perpendicular to a line joining the two metal atoms. If the average M-O-M angle is 180˚ then the metals atoms will be pulled closer together as the oxygen vibration increases. This results in the lattice shrinking in size (Sleight, 1998). The M-O bond must be highly covalent as this will lead to the thermal expansion of the M-O bond being very small and the thermal motion of oxygen being small in the direction of the M-O bonds (Korthuis et al., 1995). One of the limitations that have been found for this mechanism is the temperature range limit within which this mechanism occurs. It does not tend to include room temperature and this limits its application because of the limited temperature range within which negative thermal motion is observed (Sleight, 1998).

Cahn (1997) suggested that an essential pre-condition for thermal contraction in oxides is a framework lattice of strong metal-oxygen bonds containing two-coordinated bridging oxygens. Another cause of thermal contraction is if the density of states at the Fermi energy changes sharply with energy so that there is a large number of overlapping bands. Thermally contracting crystals are crystallographically cubic and therefore in a polycrystal, no internal stresses are generated by non-matching shape changes of neighbouring grains with increasing temperature (Cahn, 1997).

A key application for NTE materials is when they are used as components of composites with a specific desired overall thermal expansion value. The composites may be oxide-based, polymer or metal (Sleight, 1998). Some of the uses cover the range from precision instruments to casserole dishes and stove-tops (Barrera et al., 2005). A commercial application of NTE materials is as components of dental fillings, for

example, due to their expansion on cooling. The mismatch between the teeth and the fillings is suggested to be the most common reason for failure (Cahn, 1997; Sleight, 1998). Another example is the use in astronomical telescope mirrors, when these materials are mixed with normal isotropic ceramics they generate zero thermal expansion and therefore reduce the tendency of microcracking because the product will now posses excellent thermal shock resistance (Cahn, 1997; Holcombe, 1980). NTE materials are sometimes used in their pure form as well.

Some examples of materials that possess negative coefficients of thermal expansion are tantalum tungstates, ZrW_2O_8, La_2O_3, plastically deformed Invar (Fe-Ni alloys), lithium aluminosilicates, silicon and α-$TaVO_5$. From the literature studied, the tantalum tungstate that was found to have largest negative CTE is $Ta_{16}W_{18}O_{94}$ (Sigmund & Torquato, 1996; Chu et al., 1986a, 1986b).

1.1.2 Low Thermal Expansion (LTE)

Ultra-low and zero thermal expansion composites can be synthesised from mixing a metal and a negative expansion ceramic compound. A number of applications exist for materials with low and zero thermal expansion. These applications include parts of ultra-high precision machine tools like high precision ion dilatometers, space telescopes, microwave components, bridges, piping systems and mirrors (Chu et al., 1986b; Sigmund & Torquato, 1996). Successful optimal performance of some systems relies on individual parts' thermal expansion (Chu et al., 1986a).

Chu et al. (1986a) carried out a study to synthesise a metal matrix composite that could be used in space and would possess a low CTE, be isotropic and have high thermal conductivity. Due to the desired composite needing to possess a low CTE, it was determined that a small positive CTE metal matrix plus large negative CTE ceramic particles would be most appropriate. The metal matrix used was a tantalum tungstate while the ceramic particles used were Super Invar. Invar is an Fe-Ni-Co alloy and when it has improved temporal stability, it is Super Invar. However, a drawback to utilising these compounds for large structures is their potential low flexural strength and low thermal conductivity. At the conclusion of the study, it was determined that the Super Invar and $Ta_{16}W_{18}O_{94}$ would form the constituent phases of the ultra-low CTE composite which was successfully produced and found that the CTE of 1.1 x 10^{-6} $^{\circ}C^{-1}$ matched the expected value calculated from theory (Chu et al., 1986a). Holcombe (1980) compiled a study to rank and list a few properties of oxides that had low thermal expansion. The collection includes oxides with CTE's that range from 8.8 x 10^{-6} $^{\circ}C^{-1}$ to -5.1 x 10^{-6} $^{\circ}C^{-1}$. This range shows that when literature refers to low thermal expansion; it includes NTE compounds as well. In the study melting points, porosities, phase analyses and chemical analyses were also determined along with the CTEs. A range was produced in this study for the thermal expansion coefficients. In decreasing order, the ranges are intermediate (4 – 9 x 10^{-6} $^{\circ}C^{-1}$), low (1 – 4 x 10^{-6} $^{\circ}C^{-1}$) and very low (< 1 x 10^{-6} $^{\circ}C^{-1}$) (Holcombe, 1980). An example of a very low thermal expansion material is Ta_2WO_8 which has a CTE of 0.5 x 10^{-6} $^{\circ}C^{-1}$ (Wu et al., 1987).

Some materials that were found to have ultra-low thermal expansion include materials like Invar Fe-Co alloy, graphite-X (where X is carbon or polymer), composites graphite-

Mg and fused silica. All these materials possess CTEs less than 1.0 x 10^{-6} $^{\circ}C^{-1}$. The Invar alloys reflect isothermal while graphite composites reflect anisotropic dimensional changes (Chu et al., 1986a).

1.1.3 Role of thermal expansion

In this study, the thermoresponsive behaviour of barium plumbate, niobium tungstates and tantalum tungstates was investigated. These materials were suspected to possess low-to-negative thermal expansion coefficients and phase transitions. The thermal responsive behaviour will be investigated using in situ Variable Temperature Powder X-ray Diffraction (in situ VT-PXRD)

1.2 References

UCL Earth Sciences. Image of Anisotropic Thermal Expansion. http://www.ucl.ac.uk/es/news/esnews/2011/2011-02-08 (Last accessed 06 March 2013)

Balashov, D. B., Orlov, V.P.; *Zh. Fiz. Khim.* **1983**, 57, 2465

Barrera G. D., Bruno J. A. O., Barron T. H. K., Allan N. L.; *J. Phys.: Condens. Matter* **2005**, 17, R217-R252

Barrios de Arenas, I. Reactive Sintering of Aluminum Titanate, Sintering of Ceramics – New Emerging Techniques. http://www.intechopen.com/books/sintering-of-ceramics-new-emerging-techniques/reactive-sintering-of-aluminum-titanate (Last accessed 06 March 2013)

Cahn, R. W.; *Nature* **1997**; 386, 22-23

Chu, C. N., Saka, N., Suh, N.P.; *J. Eng. Mater. Technol.* **1986**, 108, 270-274(a)

Chu, C. N., Saka, N., Suh, N.P.; *J. Eng. Mater. Technol.* **1986**, 108, 275-278(b)

Forbes R. P.; Ph.D. Thesis, University of the Witwatersrand, Johannesburg, **2011**

Hahn, T.A.; *J. Appl. Phys.* **1970**, 41, 5096

Holcombe, C.E. Jr.; *American Ceramic Society Bulletin* **1980**, 59, 1219

Junlar, P., Saengchantara, W.T., and Wasanapiarnpong T.; *Pure and Applied Chemistry International Conference* **2011** *(PACCON2011);* 561-564

Kim, I.J.; *Journal of Ceramic Processing Research* **2010**, 11, 411-418

Korthuis, V., Khosrovani, N., Sleight, A. W., Roberts, N., Dupree, R., Warren, Jr. W. W.; *Chem. Mater.* **1995**, 7, 412-417

Makhura, N.B.; M.Sc. Dissertation, University of the Witwatersrand, Johannesburg, **2009**

Sleight, A. W.; *Current Opinion In Solid State & Materials Science* **1998**, 3, 128-131

Sigmund, O., Torquato, S.; *Appl. Phys. Letters* **1996**, 69, 3203-3205

Wolfenstein, J.; *Critical Grain Size for Microcracking During Lithium Insertion,* Technical Report No. ARL-TN-129, U.S. Army Research Laboratory: Adelphi, MD, **1998**

Wu, J.Z., Ota, T., Yamai, I.; *Journal of Materials Science* **1987**, 22, 2816-2822

Chapter Two: BACKGROUND

In this project, powder X-ray diffraction was the principle technique used, actually almost exclusively.

2.1 Powder X-ray Diffraction (PXRD)

PXRD is an attractive characterization technique for materials because:

- It is a non-destructive technique unlike some other characterization techniques.
- It is also considered to be a fast technique.
- It doesn't involve excessive sample preparation time.

When compared to Single Crystal XRD (SC-XRD), PXRD is advantageous because reasonable-sized single crystals are difficult to grow. It is one of the important techniques used in material science and solid state chemistry. For qualitative analysis, PXRD works because all materials possess a unique characteristic diffraction pattern and this can be considered the material's "fingerprint", hence it characterizes the material using its "fingerprint". One of the key disadvantages of PXRD versus single crystal X-ray diffraction is the compression of the three dimensional diffraction pattern into a one dimensional diffraction pattern causing a loss of some of the structural information (Kaduk, 2008).

Measurement of XRD traces as a function of T allow for thermal expansion coefficients to be calculated directly from the diffraction patterns obtained from the sample without requiring a reference material like in the case of dilatometry (Evans et al., 1996; 1997). Dilatometry measures the samples displacement with increasing temperature using a

reference material and the material of interest. It can therefore be used to validate the X-ray diffraction results though in the case of polycrystalline materials, it will only provide average thermal expansion of the bulk instead of the thermal expansion as associated with the crystallographic lattices (Payzant, 2008). Diffraction techniques can measure change in the crystal lattice parameters as a function of temperature (Makhura, 2009; Kaduk, 2008).

PXRD is also useful for quantitative phase analysis. It has been suggested that diffraction is one of the only methods which can identify and quantify compounds from obtained diffraction data (Pecharsky & Zavalij, 2003). Therefore the ability to quantify phases means that PXRD can give relative concentrations. Quantitative deductions are made based on the weight fraction of a phase in a mixture being proportional to the product of the scale factor. If a mixture is made up of crystalline components and each phase has been identified, then the weight fraction W of phase θ is:

$$W_\theta = \frac{S_\theta (ZMV)_\theta}{\sum_i^n S_i (ZMV)_i} \qquad (2.1)$$

where S = Rietveld scale factor

Z = Number of formula units per unit cell

M = Mass of the formula unit

V = Unit cell volume

Primarily quantitative diffraction analysis depends on unique sets of diffraction-peak positions and intensities for each crystalline component, no interference resulting from the diffraction patterns of the components overlapping and most importantly, the intensity of each component in the pattern being proportional to the amount present (Hill & Howard, 1987).

The intensity of the diffraction peak is an important component in understanding the properties of the material being studied. The measurement of the intensity of a point is easier than calculating the intensity of the point (Kaduk, 2008). By definition the integral area under the peak is the intensity of the peak. Though the intensity relies on the arrangement in the unit cell and ionic state of the atoms, there is a contribution from the geometry of the instrument used. A number of factors are associated with the intensity of a particular peak and therefore are important (Pecharsky & Zavalij, 2009). The formula that summarises the various factors that make up the observed intensity of a peak is:

$$I_{hkl} = S \times P_{hkl} \times L_{\theta} \times P_{\theta} \times A_{\theta} \times T_{hkl} \times E_{hkl} \times \left| F_{hkl} \right|^2 \qquad (2.2)$$

where I : integral intensity

P : multiplicity factor

L : Lorentz polarization factor

T : Preferred orientation factor

A : Absorption multiplier

E : Extinction factor

S : Scale factor

F : Structure factor

2.1.1 Structure factor (F)

The structure factor is best described by:

$$F_{hkl} = \sum f_n \exp [\, 2\pi i (hx + ky + lz) \,] \qquad (2.3)$$

The F_{hkl} is usually represented as the modulus $|F_{hkl}|$. The structure factor is a ratio of the amplitude of the wave scattered by all the atoms in a unit cell over that scattered by one electron. This ratio comes about because the scattered beam is affected by the atomic arrangement (x, y, z). The relationship between the structure factor and the intensity of the diffracted beam is: $I = |F|^2$ (McCusker et al., 1999). The contribution of a phase to the overall intensity profile is accounted for by the structure factor (Pecharsky & Zavalij, 2009).

2.1.2 Multiplicity factor (P)

This factor describes the number of symmetrical equivalent reflections. Symmetrical equivalent reflections arise from differently oriented several sets of hkl planes while they have the same F^2 and d spacing values. If the reflection planes have the same F^2 and d values then the multiplicity factor is based on the quantity of variations of the ±h, ±k and ±l. The multiplicity factors vary depending on the crystal system. The highest multiplicity for orthorhombic, tetragonal and cubic systems is 8, 16 and 48 respectively.

2.1.3 Lorentz polarization factor (Lp)

This factor results from multiplying two corrective factors and is one of the critical experimental quantities that influence intensity with respect to the diffraction angle of x-rays (Reynolds, 1986). This is done because both these factors depend on experimental conditions and not on the structural model. The two corrective factors are the Lorentz factor and the polarization factor. The Lorentz correction answers for the period of time a crystal is diffracting any specific scattering beam. This means the Lorentz factor relies on both the diffraction geometry and the Bragg angle. The polarization correction, on the other hand, arises from partial polarization of radiation from it being 'monochromatized' by the crystal's reflection.

Therefore in frequent situations each factor is defined as:

Lorentz factor is $\frac{\mathbf{1}}{\mathbf{sin}(\mathbf{2}\boldsymbol{\theta})}$

Polarization factor is $\frac{(\mathbf{1}+\boldsymbol{A}\boldsymbol{cos}^{\mathbf{2}}\,\mathbf{2}\boldsymbol{\theta})}{(\mathbf{1}+\boldsymbol{A})}$

Therefore the Lorentz-polarization factor, Lp is $\frac{(\mathbf{1}+\boldsymbol{A}\boldsymbol{cos}^{\mathbf{2}}\,\mathbf{2}\boldsymbol{\theta})}{(\mathbf{1}+\boldsymbol{A})\,\mathbf{sin}\,\mathbf{2}\boldsymbol{\theta}}$

where A is $\cos^2 2\theta_M$ & the monochromating crystal's Bragg angle is θ_M (IUCr dictionary, 2012; Reynolds, 1986).

2.1.4 Sample absorption

Sample absorption is another important factor that needs to be taken into consideration. It is best described as:

$$I_{diffracted} = I_{incident} \exp(-\mu t) \quad (2.4)$$

Where μ represents the linear absorption coefficient

t represents the thickness of the sample

The units for the absorption factor are cm^{-1} (McCusker et al., 1999).

2.1.5 Scale factor (S)

Determination of the scale factor accurately is important as it leads to accurate extraction of structure factors and possible approximation of the overall thermal parameter. According to Riello et al. (1998) several methods exist, for crystalline powder diffraction, to scale its relative structure factors. The limitation is that a large number of factors need to be taken into consideration and therefore though the methods exist, they are not common. With direct methods, a normalization factor is applied in the early stages of the Rietveld refinement that leads to better extraction of structure factors and approximation of the scale factor (Riello et al., 1998).

2.1.6 Extinction Factor

Extinction affects intensity and may lead to systematic errors. Extinction can either be primary or secondary. The former refers to extinction that occurs within a single crystal while the latter results from a ray reflecting off one crystal and being reflected off a second crystal. The formula for the determination of the extinction factor is:

$$\mathbf{I_m = y \,.\, I_{kin}} \quad (2.5)$$

where I_m is the measured intensity, I_{kin} is the theoretical kinematic intensity and factor y < 1, it is only unity when there is no extinction.

With symmetrical Bragg geometry, I_{kin} is defined as (Tomov, 2005):

$$\mathbf{I_{kIn}} = \frac{PIoQS}{2\mu} \qquad (2.6)$$

where I_o = incident beam intensity

S = cross-section of the beam

Q = reflectivity per unit cell volume

μ = ordinary linear absorption coefficient

P = texture factor

2.1.7 Preferred Orientation (T)

Preferred orientation results from crystals not orienting randomly but rather in a preferred manner and this usually occurs with needle-like and plate-shaped crystals (Pecharsky & Zavalij, 2003). This is important because it affects the diffraction pattern obtained from the sample. Three different functions can be used to describe the preferred orientation experienced by the sample. The functions are the generalized spherical harmonics, a pole density distribution using an inverse pole figure and the March-Dollase function (Kim et al., 2003). The TOPAS software (Coelho, 2007) that is used in this research to refine models used from the powder patterns obtained uses the Spherical harmonics function. This function is more complex than the other two and has

been seen to be more effective (Kim et al., 2003). It is based on the measuring the pole density distributions of a number of diffraction peaks.

Temperature is important in our research because variable temperature (VT-) PXRD forms the core analysis technique for understanding the thermo responsive behaviour of the compounds being investigated. The varying temperatures, that the compounds are exposed to, cause them to experience thermal vibrations. These vibrations affect the resultant powder pattern observed. The changes observed include shifts in the 2θ positions as the unit cell expands or contracts, an increase in the intensity of the background scattering and finally a decrease in the intensity of the diffraction peaks (McCusker et al., 1999).

2.2 Continous On-line XRD Analysis (COXA)

This is also known as In situ Variable-Temperature XRD analysis (VT-XRD). Interest in this has resulted from it being one of the major modern advances of powder diffraction for material science (Cranswick, 2008). The various reactions and transformations that take place in a furnace or in a vessel during a solid-state synthesis or reaction have to date been poorly characterized and therefore this technique can assist in solving many “mysteries”. In situ PXRD gives a clearer view of the phase formation that takes place during solid-state synthesis because reactions can be followed, showing the various intermediates formed or presence of any competing reactions. This technique can also provide insight into phases that are not stable at ambient pressure, study of the interaction of phases as well as deviations in phases in a non-ambient environment. Modifications on-line can also give the optimized conditions for the final crystalline

product (Cranswick, 2008). Reactions can also be manipulated and the effects monitored even when the starting and end products are the same as those from reactions without the modifications. Information may also be obtained that may assist in the isolation of the intermediate product. It also allows lattice expansion studies and kinetic studies to be carried out on the behaviour of materials with varying temperatures, pressures, time and chemical environments. Other variations can include relative humidity; gas partial pressure or chemical loading on the structure (Payzant, 2008). The data that is obtained from a COXA analysis is subjected to the same concerns faced in the data collection of conventional data. Experiments that involve gas being passed over or through your sample possess the main issue of ensuring that the powder is not blown away at the start, during or at the end of the experiment. The diffraction data given out of an in situ run is a single raw file which contains all the data for the various scans.

Thermal expansion is an important aspect of this research and so COXA analysis is an important technique in the investigation of this property of the materials of interest. X-ray diffraction provides crystallographic coefficients rather than those of the bulk and this makes the technique suitable for these studies. X-ray diffraction is known to provide high precision coefficients and therefore this should be true of the thermal expansion coefficients. The issue with precision is that it doesn't guarantee accuracy of the coefficients. The key sources of errors when it comes to thermal expansion is the 2θ zero error as well as sample displacement. These errors can both be corrected for in the refinement process.

2.3 X-ray Powder Diffraction Diffractometers

Two x-ray diffractometers were employed namely a Bruker D8 Advance and a Bruker D2 Phaser. Majority of the data and quantitative analyses presented are from the Bruker D8 Advance.

The Bruker D8 Advance diffractometer was used to perform the variable temperature in situ diffraction experiments in the fitted Anton Par XRK 900 reaction chamber. The Anton Paar XRK 900 is a high temperature reaction chamber for X-ray diffraction lab based experiments up to a maximum temperature of 900 °C (Anton Paar, 2005). This reaction chamber is composed of the sample holder, the lid-supported furnace and the housing. The lid is used to deliver current to the heating elements as well as housing the sockets for the thermocouple. The housing is attached to the goniometer (Rayner, 2011). Other components of the D8 are the Bruker VANTEC-1 PSD detector, Cu X-ray source, secondary beam nickel filter, primary and secondary soller slits. The Cu X-ray tube source gives $CuK\alpha_1$ and $CuK\alpha_2$ radiation. Within the reaction chamber there is a heating stage which operates in the 30 ˚C to 900 ˚C temperature range. It heats at a maximum rate of 0.3 ˚C.sec^{-1}. A thermocouple is within the chamber to measure and control the sample temperature. Around the furnace of the XRK900 is a heat shield which is surrounded by cooling water jacket. The incident and reflected x-rays interact and are reflected, from the sample in the furnace respectively, through beryllium windows in the heat shield. Where the beryllium windows are, the housing has transparent capton foil that is aligned directly with the windows (Rayner, 2011). Experiments in the chamber were carried out under ambient conditions or with various gases being passed over the samples. The chamber allows for gases to be passed

through the sample but in this study, the gases were only passed over the sample. The gas pressure within the reaction chamber can reach a pressure of 10 bar, however in this study gas pressure was kept at atmospheric conditions. The reaction chamber allowed the performance of solid state and solid state-gas experiments. The experiments are possible because of the design of the chamber which is designed to allow a homogenous flow of reaction gas over the sample as well as adequate heating to prevent condensation of reaction gases. It is of the assumption that this ensures that there are no temperature gradients within the sample that is being analysed.

A Macor® sample holder was utilised for all the experiments carried out in the D8 Advance diffractometer. Macor® is a material that composes of 45% borosilicate matrix glass and 55% fluorophlogopite mica crystal. It is a white, odourless, non-porous machineable glass-ceramic material that can withstand temperatures up to a 1000 ˚C and therefore shows resistance to chemical damage as well as good chemical resistance to temperature change within the range of ambient temperature to 1000 ˚C. It shows very little thermal expansion and is an excellent insulator at high temperatures (Macor, 2013). When the sample holders were used, a solid platinum foil disc was placed in the sample holder before the sample was loaded instead of the Macor® frit. This minimised interaction of the sample holder with the sample. The sample holders have an internal diameter of 11 mm and can hold a sample of approximately 1.5 mm thickness. Sample preparation involved loading the sample holder using a spatula, and pressing the sample down with a glass slide to ensure the right height and appropriate packing. Unlike with the desktop Bruker D2 Phaser samples, preferred orientation is

more likely due to this sample preparation technique especially if the sample contains needle-shaped or plate-like crystallites.

The Bruker D2 Phaser is a low power desktop diffractometer. Like the D8, it also has a Cu x-ray source, a secondary nickel filter, primary and secondary soller slits. Unlike the D8 Advance, it has Bruker LynxEye PSD detector. The sample holders used for analysis in the D2 Phaser are made of Perspex. If a small amount of sample was being analyzed a zero background aligned silicon disc would be contained in the Perspex sample holder. The primary beam in both systems contains $K\alpha_1$ and $K\alpha_2$ radiation as neither is equipped with primary beam monochromators.

The specifications of the two diffractometers are:

Table 2.1: Bruker D2 Phaser desktop instrument details

Goniometer Radius	141.1 mm
X-ray Source Tube Type	Copper/ Cobalt
Type of Detector	LynxEye PSD
Primary and Secondary Soller Slits	2.5 mm
X-ray Generator: Voltage and Current	30 kV & 10 mA
Monochromator	Nickel Filter
Detector 2θ Angle Range	5˚

Table 2.2: Bruker D8 Advance instrument details

Goniometer 1˚ & 2˚ radii	250 mm
X-ray Source Tube Type	Copper
Type of Detector	VÅNTEC-1 PSD
Primary and Secondary Soller Slits	2.5 mm
Receiving Slit	10.6 mm
Fixed Divergence Slit (FDS)	0.6 mm
X-ray Generator: Voltage and Current	40 kV & 40 mA
Detector 2θ Angle Range	3°
Nickel Filter	Yes

2.4 Rietveld Refinement

Before 1978, this method was known as the 'full pattern refinement' method. This whole-profile method used for structure refinement was first formulated by Hugo Rietveld (1969). This method was used assuming that the crystallites were randomly oriented (Rietveld, 1969). There were limitations to the implementation of the method due to lack of sufficient computer power to execute refinements and the development of functions to describe peak profiles. This led to the implementation taking place in the mid-1980s (Kaduk, 2008).

Rietveld considered that neutron diffraction was a direct method that gave a smooth curve as the sum total of constituent Gaussian peaks on a smooth background (Rietveld, 1967). The formulation of the Rietveld refinement method resulted from two

important observations. Firstly, each data point is an equally valid least-squares quantity. Secondly, intensities calculated from the model can be used for distribution of the intensities of a group of overlapping peaks (Kaduk, 2008). Prior to the introduction of this whole-profile method, analysis of a single peak at a time was the method used for diffraction data. When the Rietveld refinement method was formulated, it was to be applied to low-resolution diffraction data. In the modern implementation of Rietveld refinement, it involves a wide variety of factors that are considered.

The quality of the data collected or used is critical to the successful use of this method. It is highly possible to determine the structural parameters from a well resolved powder diffraction pattern, but overlapping reflections that are inherently present hinder the complete use of the information that is available to carry out a refinement of the structural parameters (Rietveld, 1967). Some factors that are considered prior to the data collection include geometry, quality and calibration of the diffractometers used as well as appropriate sample preparation and parameters, such as the counting time and slit sizes, used for actual PXRD measurements. If appropriate measures are taken with the data collection, Rietveld refinement is a powerful technique for extracting structural details from powder diffraction data (McCusker et al., 1999). With Rietveld full pattern refinement there is the possibility that diverging solutions and ‘false’ minima may be found and therefore chemically sensible models should be used. The order in which the refinement is carried out is also important. When the Rietveld refinement has been carried out and completed, the results of the agreement between the observed and calculated patterns are presented in the form of agreement indices and as a difference curve.

Bruker DIFFRAC EVA (2010) software is used to carry out a search match, which helps characterize a diffraction pattern obtained from a material of interest. The search match process involves comparisons between the observed diffraction patterns against those of known compounds in the Powder Diffraction File (PDF-2) database which is owned by the International Centre for Diffraction Data (ICDD, 2013). The PDF-2 database is used within the EVA software whereas there is also an International Crystal Structure Database (ICSD) that is accessible online (2013). The ICSD numbers associated with the compounds in the PDF can then be used in the search engine of the online ICSD to download the CIF files of interest. Once a match is made, a crystallographic information file (CIF) is obtained from the ICSD website from <http://icsd.fiz-karlsruhe.de/>. The CIF file is used to generate the starting model for the refinement process. Therefore the Rietveld refinement fits a model to the data and the Rietveld algorithm minimises the weighted sum of squared differences between the observed and computed intensity values by optimising the model function (Toby, 2006). Rietveld refinement is never fitting data to a model. Peak positions, thermal displacement and atom positions are determined using the unit cell dimensions. These dimensions calculate the diffraction pattern which is used in the Rietveld refinement (Hill & Howard, 1987). The Rietveld refinement process involves refinement of atomic positions and lattice, profile and background parameters. The peak shape comes about as the result of characteristics of the X-ray beam, the parameters used for the experiments, the shape and size of the sample (Makhura, 2009). A number of factors affect the peak intensities. These include structure factors, Lorentzian polarization factor, atomic displacement, absorption and preferred orientation (McCusker et al., 1999). Rietveld refinement strives to take into

account these factors and to rectify them so as to present the most accurate representation of the sample being analysed. The use of high resolution or synchrotron sources is found to reduce instrumental factors to the point where they become insignificant (Makhura, 2009).

A number of Rietveld refinement programs are available. Some are commercial and others are free. The Rietveld refinement results presented in this study were carried out using the commercial Bruker TOPAS 4.2 software (Coelho, 2007). Some of the other Rietveld programs are listed in Table 2.

Table 2.3: Available Rietveld refinement software

Commercial	**Free**
MDI Jade	GSAS (General Structure Analysis System)
PANalytical HighScore Plus	LHPM-Rietica
MDI Ruby	Fullprof
	Simref
	BGMN
	MAUD

Rietveld refinement can be carried out sequentially or via parametric refinement (Styles et al., 2010; Stinton & Evans, 2007). Stinton and Evans described a methodology called ‘parametric Rietveld refinement’ (Stinton & Evans, 2007). This methodology allowed any parameter to be described by a single overall value or by describing its evolution

throughout the data collection by a function and can be simultaneously refined from a large body of diffraction data (Stinton & Evans, 2007). Advantages of parametric fitting are i) fewer free variables are used for data fitting; ii) the use of an entire data set will determine certain parameters that will avoid false minima and reduce derived uncertainties; iii) possibly reduced standard uncertainties in parameters leading to higher precision of the refined parameters and iv) non-crystallographic quantities experimental temperature and rate constants can be refined (Stinton & Evans, 2007). Parametric refinement also finds application in understanding the origins of low and even negative thermal expansion of various materials. Sequential fitting refinement is the method used in this research and it uses the output of a previous refinement as the input for the next refinement. Its advantage is that if a phase change occurred, the input model can be modified accordingly without the loss of information or the need to begin the refinement again (Styles et al., 2010).

TOPAS can be used in one of two operation modes. These are the graphical user interface (GUI) and the Launch mode. The GUI mode is mainly associated with sequential refinement whereas the Launch mode is associated with parametric refinement. The advantage of TOPAS is that simultaneous refinement of the parameters can take place without causing divergence of the model or generation of false minima. This software also supports the relative quick analysis of a large amount of data collected at various temperatures (Makhura, 2009). In this study, the graphical user interface mode of TOPAS was used for the Rietveld refinements carried out.

Quantitative analysis of polycrystalline mixtures can be carried out using the Rietveld method without needing standards or laborious experimental calibration procedures

(Lutterotti & Scardi, 1992; Hill & Howard, 1987). This is advantageous as it permits the determination of phase abundance without a need for prior calibration with an actual standard. It uses the crystal structure parameters to directly calculate the peak intensities (Hill & Howard, 1987). It also allows for the determination of the amorphous and crystalline content in mixtures that have multiple phases. The product of the scale factor is proportional to the weight of a phase in a mixture and the weight fraction of a phase can be calculated as long as all the phases are identified and crystalline (Hill & Howard, 1987). Rietveld refinement can also include texture contributions, residual stresses, and microstructure contributions. This is important because these affect the integrated intensities, peak positions and peak shape respectively (Lutterotti & Gialanella, 1998). Systematic errors may arise as a consequence of preferred orientation and this will therefore affect the quality of the quantitative results obtained. How the sample is packed as well as spinning the sample may help alleviate the effects of the preferred orientation before the refinement step. Compared with other approaches Rietveld refinement uses all the peaks in a pattern instead of selecting some peaks and basing the refinement on those relative peaks only (Pecharsky & Zavalij, 2003).

A polynomial is usually used to describe the background (Lutterotti & Gialanella, 1998)

Cystallite size is described by the Scherrer equation

$$\boldsymbol{\tau = \frac{0.9\lambda B}{cos\theta}} \tag{2.7}$$

The B factor varies dependent on whether or not it is described as having the

Lorentzian or Gaussian function. Crystallite size can also be determined from the Bragg equation. The crystallite calculated from this equation is the average crystallite size. The finite width of a diffracted peak results from crystallites of finite size.

There are a number of factors that define the profile for each reflection. These factors are the intensity, the peak shape and the angular position. The effects of the instrumental and structural features on the sample are approximated in the profile shape function (Pecharsky & Zavalij, 2003). There are a number of peak profiles which are defined by the half-width at half maximum (HWHM) as well as the Gaussian content in the Pseudo-Voight function which is known as the shape parameter. Two of the most widely used profile shape functions are the Pseudo-Voigt and the Pearson VII. The peak profiles defined by these parameters are the Pearson VII, Pseudo-Voigt and the Voigt function (Lutterotti & Gialanella, 1998). Pseudo-Voigt function is a combination of Lorentzian and Gaussian components plus a function resulting from the axial divergence of the diffracted beam at low angle. The additional function describes the peak symmetry (Ahtee et al., 1984). Pearson VII has the advantage in that it gives the better approximation for Cu Kα peak shape.

Two possible extraction methods can be used to acquire information required for a structural refinement. These are the Le Bail (1988) and the Pawley (1981) method. The Le Bail method can be used when a partial structural model is available. A major consequence of a partial structural model is significant deviations of the calculated intensities from observed intensities. The Le Bail method is a structure-free approach that adjusts the intensities of the reflections to fit the observed ones in order to obtain initial values that will be used for the profile parameters (Le Bail et al., 1988). When this

method is used in refinement, it is found to extract a list of integrated intensities for structure determination from powder pattern as an added advantage. Basically the Le Bail refinement is based on the original Rietveld method for determining observed structure-factor magnitude (McCusker et al., 1999). The Pawley (1981) method is a method that minimises the sum of squares of the differences between the calculated and observed profiles. It enables the estimated standard deviations of the reflection intensities to be more accurately estimated. With refinements, initial values for profile parameters can be determined regardless of which of these two methods is used. Once a reliable structural model has been established, the parameters can be further refined (McCusker et al., 1999).

The order in which the refinement is carried out is very important. The strategy should involve refinement of the most important variables first, followed by the rest of the refinable variables until an adequate solution is found. Some of the parameters that can be refined include the scale factor, background, lattice parameters, zero shifts or specimen displacement, preferred orientation, isotropic temperature factor B and other profile parameters (Pecharsky & Zavalij, 2003; Makhura, 2009).

One way of rectifying varying sample displacement errors is to refine it along with the lattice parameters as it will vary at the different temperatures. In the data collection step, sample displacement errors can be minimised by collecting the data over a wider 2θ range. A calibration curve can be generated by plotting the refinement resultant values versus temperature and so the displacement for each point can be seen clearly. From the graph, it will reflect clearly which data points do not need to be refined and therefore should be fixed. The 2θ zero error could be minimized through careful alignment of the

diffractometer by using a National Institute of Standards and Technology (NIST)-certified standard. This is not an error that appears often after the alignment has been carried out the first time (Payzant, 2008).

2.4.1 Agreement indices

R factors are important in Rietveld analysis as they are used to reflect if the refinement is good enough (Toby, 2006).

Toby (2006, page 67) stated that “there is no simple way to distinguish a good fit from one that is just plain wrong based on R factors or other discrepancy values” (Toby, 2006). This statement reflects that though there are a number of Rietveld indices, there isn’t an absolute measurement for refinement quality. This can be seen when small error index values are obtained for wrong models with poor quality data rather than for excellent models with high quality data. The agreement indices are strongly dependent on the signal-to-noise ratio and on the relative amount ‘background only’ regions (Hill & Fischer, 1990). Therefore one of the key reasons that these indices are not absolute measures is because they measure the fitting of the background as well as structural model. Thus the important factor is whether or not the model is chemically reasonable (Toby, 2006). The best fit usually occurs when the square of the residual is minimised.

Some distinctive properties of the various R factors:

R is basically a quantity that is minimized during fitting procedures or least squares.

R weighted pattern (R_{wp})

R_{wp} is a quantity that is weighted in order to emphasize intense peaks over background. This value may be misleading in cases where high backgrounds are observed because the R_{wp} value, though small, is due to a large proportion of intensity being accounted for by the background though using a poor structural model. Basically the Rwp is the square root of the quantity minimised scaled by the weighted intensities. If R_{wp} approaches R_{exp}, that is considered to be a 'good' refinement (Young, 1993).

$$\mathbf{R_{wp}} = \left[\frac{\boldsymbol{wi}\,(\boldsymbol{Yoi}-\boldsymbol{Yci})^2}{\sum_i \boldsymbol{wi}(\boldsymbol{Yoi})^2}\right]^{1/2} \qquad (2.8)$$

where w_i = weight function

y_{oi} = intensity observed at point i

y_{ci} = calculated intensity at point i

R expected (R_{exp})

R_{exp} is a quantity that evaluates the quality of the data and therefore estimates the best possible R_{wp} for a data set. The best possible R_{wp} would come about as a result of an ideal model which would accurately predict the y_{oi} value. R_{exp} is therefore the expected R value from an ideal model.

$$\mathbf{R_{exp}} = \frac{\boldsymbol{N}-\boldsymbol{P}}{\sum_i \boldsymbol{wiYoi}^2} \qquad (2.9)$$

where N = number of observed data points

P = number of least-squares variables (variance)

It is therefore important for the number of the data points to be significantly larger than the number of least-squares variables so that the subtraction can be negligible.

Profile R-factor (R_p)

R_p is the unweighted profile R-factor but is not used often as it is not considered very useful (Kaduk, 2008).

$$\mathbf{R_p} = \frac{\sum_i |Yoi - Yci|}{\sum_i Yoi} \quad (2.10)$$

R Bragg (R_B)

R_{Bragg}, also expressed as R_B, is a quantity that attempts to modify the r for a specific phase. (Young, 1993; Makhura, 2009). It is the measure of the validity of the crystal structure model (Hill & Fischer, 1990).

$$\mathbf{R_B} = \frac{\sum_k |I_{ko} - I_{kc}|}{\sum_k |I_{ko}|} \quad (2.11)$$

where I_{ko} = integrated 'observed' intensity of reflection k

I_{kc} = calculated intensity

The limitation for the reliability of the R_{Bragg} is it fails when the peaks being analysed and described have serious unmodelled asymmetry and long tails. The results of these observations are the exclusion of part of the peaks from the intensity estimate (Toby, 2006).

Goodness of Fit (χ^2)

Goodness of fit is described as the ratio between R weighted pattern and the R expected. If the model utilised in a refinement is of poor quality the χ^2 will start out large and will decrease as the agreement between the model and the data improves. There are some limits that guide the use and interpretation of refinement indices. These

include the fact that the smallest value for R_{wp} is the R_{exp} value and the fact that χ^2 should never be lower than 1 because this suggests that there has been an error in scaling or data conversion (Toby, 2006). When the goodness of fit is at unity, this reflects an excellent refinement.

$$\chi^2 = \frac{R_{wp}}{R_{exp}} \tag{2.12}$$

When common factors are cancelled out, the equation is reduced to:

$$\chi^2 = \left[\frac{WSS}{N-P}\right] \tag{2.13}$$

where WSS = minimum weighted sum of squares – weighted residual value

Three possible errors have been suggested for χ^2 values being largely greater than 1 are:

- Incorrect model was used.
- σ has been underestimated or incorrectly weighted though suitable model was used.
- Model used possessed systematic errors.

Good quality data can give very large χ^2 values when there is a high ratio of signal to noise or when a position-sensitive detector is used. If good data has been collected, the results can be reported as long as suitable explanations accompany the publication as to why the χ^2 is high (Kaduk, 2008).

There are ways in which the refinement indices can be improved. χ^2 is affected by the length of time spent collecting the data. When counting times are increased, this increases the statistical precision of the diffraction measurement and therefore results in

the R_{exp} decreasing. Longer counting times also increase the difference between the R_{wp} and the R_{exp} and this gives an even larger χ^2 even though the fitted model has improved (Toby, 2006).

Pawley (1981) and Le Bail (1988) fits are methods that fit a pattern using global parameters instead of a structural model. The results of these fits can be used in comparison to the results of the Rietveld refinement to determine the value of the agreement indices obtained from the Rietveld method. If the values vary significantly, this suggests possible errors with the structural model (Kaduk, 2008).

The Lorentz-Polarization factor depends on various aspects of the instrument. These include the positioning of the sample, angle of the monochromator, the geometry of the instrument, the size of the beam and on the detector used (Lutterotti & Gialanella, 1998).

When the diffraction angles are large, Rietveld refinement can still produce good approximations of the scale factors when there is a small degree of preferred orientation. This is due to the averaging out of the effects (Hill &Howard, 1987).

The absorption factor is dependent on the thickness of the sample. The absorption of thin samples is dependent on the 2θ (McCusker et al., 1999).

Rietveld refinement has been found to be useful in resolving challenges like anisotropic broadening caused by crystallite size and strain. Two approaches were discussed in a paper by Popa (1998) to deal with anisotropic broadening.

In summary, in this investigation the X-ray data was collected on the Bruker D2 Phaser and the Bruker D8 Advance diffractometers. The data was analyzed using Bruker DIFFRAC EVA software version 3 (2010). The Rietveld refinements of the data were carried out using the TOPAS software version 4.2 (Coelho, 2007) modelling package.

The order in which the refinement is carried out is important. Of the materials studied in this research, the refinement was carried out in this order:

- Chebychev background 2^{nd} order
- Scale
- Lattice parameter
- Crystallite size
- Peak shape function
- Preferred orientation
- Sample displacement \ zero shift \ sample height correction
- Absorption

If need be, the thermal isotropic factor (B_{eq}) is refined as well.

All the crystal structure diagrams were generated using Crystal Impact's Diamond software (Pennington, 1999). This software provides crystal and molecular structure visualization. The product operates using the CIF files that have either been downloaded from the online ICSD or have been generated from the refinements done.

2.5 References

Ahtee, M., Unonius, L., Nurmela, M., Suortti, P.; *J. Appl. Cryst.* **1984**, 17, 352

Anton Paar XRK 900 User Manual, Anton Paar GmbH, **2005**

BGMN: http://www.bgmn.de/ (Last accessed 14 March 2013)

Coelho, A. A.; *TOPAS* **2007**, V 4.2, Bruker AXS

Cranswick, L. M. D.; An Overview of Powder Diffraction. In *Principles and Applications of Powder Diffraction,* Clearfield J., Reibenspies J. & Bhuvanesh N.; Blackwell **2008**, 7-9

DIFFRAC.EVA: *The Next Era in Phase Analysis*, Bruker AXS, Karlsruhe, **2010**

Diamond version 3: http://www.crystalimpact.com/ (Last accessed 15 March 2013)

Evans, J.S.O., Mary, T.A., Sleight, A.W.; *Journal of Solid State Chemistry* **1997**, 133, 580-583

Evans, J.S.O., Mary, T.A., Vogt, T., Subramanian, M.A., Sleight, A.W.; *Chem. Mater.* **1996**, 8. 2809-2823

Fullprof: http://www.ill.fr/sites/fullprof/ (Last accessed 14 March 2013)

GSAS: http://www.ccp14.ac.uk/ccp/ccp14/ftp-mirror/gsas/public/gsas/ (Last accessed 14 March 2013)

Hill, R.J., Howard, C.J.; *J.Appl. Cryst*. **1987**, 20, 467-474

Hill, R.J., Fischer, R.X.; *J. Appl. Cryst.* **1990**, 23, 462-468

ICDD, *The International Centre for Diffraction Data*: http://www.icdd.com (Last accessed 07 March 2013)

ICSD, International Crystal Structure Database, Karlsruhe,

http://icsd.fiz-karlsruhe.de/ (Last accessed 15 March 2013)

IUCr dictionary: http://reference.iucr.org/dictionary/Lorentz%E2%80%93polarization_correction (Last accessed 14 September 2012)

Kaduk, J.A.; Structure Refinement In *Principles and Applications of Powder Diffraction;* Clearfield A., Riebenspiens J. & Bhuvanesh N.; Wiley and Sons, Blackwell publishing, United Kingdom, **2008**, 310-364

Kim, Y.I., Nahm, S.H., Jung M.J.; *Materials Letters* **2003**, 57, 3653-3659

Le Bail, A., Duroy, H., Fourquet, J.L.; *Mater. Res. Bull.* **1988**, 23, 447-452

LHPM-Rietica: http://www.rietica.org (Last accessed 14 March 2013)

Lutterotti, L., Gialanella, S.; *Acta Mater.* **1998**, 46, 101-110

Lutterotti, L., Scardi, P. ; *J. Appl. Cryst.* **1992**, 25, 459-462

Macor®: Corning speciality materials, *Lighting and Materials,* http://www.corning.com/docs/specialtymaterials/pisheets/Macor.pdf (Last accessed 07 March 2013)

Makhura, N.B.; M.Sc. Dissertation, University of Witwatersrand, **2009**

MAUD: http:www.ing.unitn.it/~maud/ (Last accessed 15 March 2013)

McCusker, L.B., Von Dreele, R.B., Cox, D.E., Louer, D., Scardi, P.; *J. Appl. Cryst.* **1999**, 32, 36

MDI Jade &Ruby: http://www.materialsdata.com/ (Last accessed 07 March 2013)

PANalytical HighScore Plus: http://www.panalytical.com/index.cfm?sid=212 (Last accessed 07 March 2013)

Pawley, G.S.; *J. Appl. Cryst.* **1981**, 14, 357-361

Payzant, A.E.; *In-situ* Diffraction Experiments In *Principles and Applications of Powder Diffraction;* Clearfield A., Riebenspiens J. & Bhuvanesh N.; Wiley and Sons, Blackwell publishing, United Kingdom, **2008**, 372-376

Pecharsky, V.K., Zavalij, P.Y.; *Fundamentals of Powder Diffraction and Structural Characterization of Materials*, Kluwer Academic Publishers, Boston, **2003**

Pennington, W.T.; *J. Appl. Cryst.* **1999**, 32, 1028

Popa, N.C.; *J. Appl. Cryst.* **1998**, 31, 176-180

Rayner, M.K.; Ph.D. Thesis, University of Witwatersrand, Johannesburg, **2011**

Reynolds, R.C.; *Clays and Clay Minerals* **1986**, 34, 359-367

Riello, P., Fagherazzi, G., Canton P. ; *Acta Cryst.* **1998**, A54, 219-224

Rietveld, H.M.; *Acta Cryst.* **1967**, 22, 151-152

Rietveld, H.M.; *J. Appl. Crystallogr.* **1969**, 2, 65

Simref: http://www.uni-tuebingen.de/uni/pki/simref/simref.html (Last accessed 14 March 2013)

Stinton, G.W., Evans, J.S.O.; *Journal of Applied Crystallography* **2007**, 40, 87-95

Styles, M.J., Riley, D.P., Madsen, I.C, Kisi E.H. **2010**, "Parametric Rietveld Refinement Applied to In Situ Diffraction Studies" *34th annual condensed matter and materials meeting* http://www.aip.org.au/info/sites/default/files/cmm/2010/p18.pdf

Toby, B.H.; *Powder Diffraction* **2006**, 21, 67-70

Tomov, I.; *Archives of Metallurgy and Materials* **2005**, 50, 147-157

Young R.A., **1993**, "*The Rietveld Method",* Oxford Science Publication, 95-96

Chapter Three: INSTRUMENTAL CONSIDERATIONS

3.1 Standard Operation Procedure (SOP)

3.1.1 Sample preparation for run on the D8 Advance

A Macor® (2013) sample holder was used with a platinum disc inserted in it before the sample was loaded. This was done to avoid metal absorption and interaction between the sample and the Macor® sample holder. A sample residue collector was made from aluminium foil and was placed so as to avoid getting any sample trapped in unwanted areas of the sample holder chamber or the holder itself. Once the sample holder had been packed, the sample was ready to be placed in the reaction chamber of the XRK900. The thermocouple and the spinner cables are attached to the sample holder and they needed to be attached to the reaction chamber. When screwing in the sample holder, it was important to ensure that the grey spinner cable was at the front and the colourless thermocouple cable was at the back. It was checked that the green cable was attached to the temperature measurement slot and that the red cable was attached to the heater socket as seen in Fig 3.1. Once all the cables had been attached and the sample holder had been screwed in tightly, the D8 Advance doors could be closed. The various components of the D8 Advance reaction chamber, which is also referred to as the Anton Paar XRK900, that have been mentioned are shown in Fig 3.2. The rest of the chapter is written as a handbook.

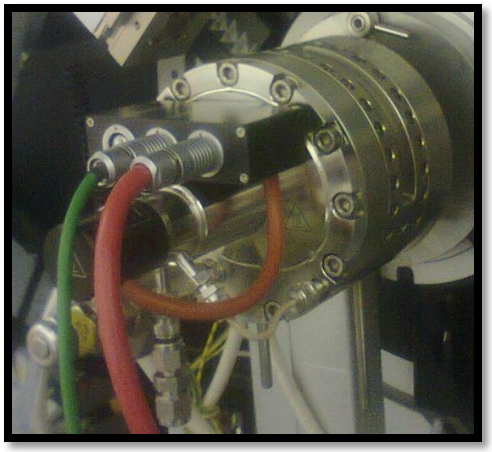

Figure 3.1: The green and red cables attached in the correct temperature measurement slot and heater socket respectively.

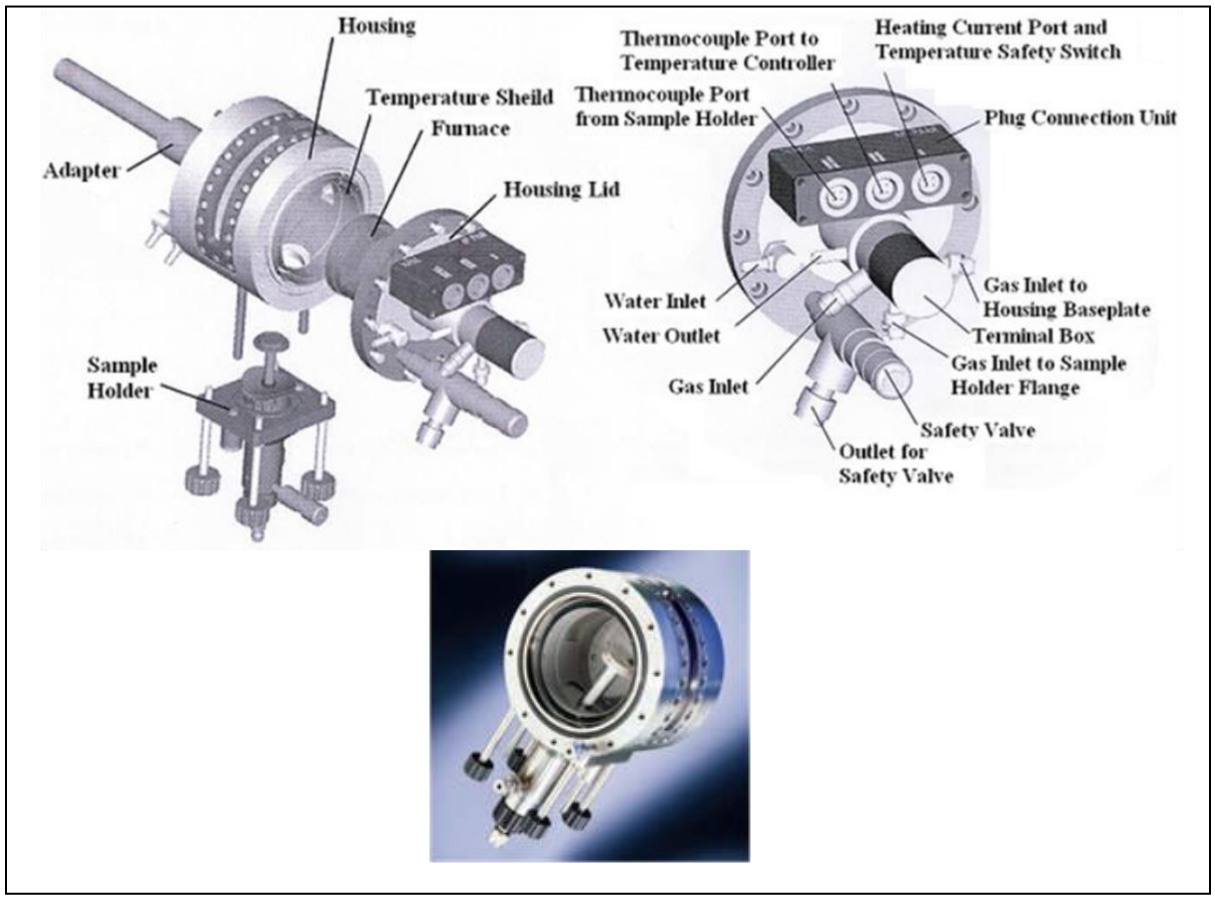

Figure 3.2: Schematic diagrams of the various components of the Anton Paar XRK900. Bottom diagram shows how the Macor® sample holder sits within the reaction chamber.

3.1.2 Setting up experimental parameters

XRD Wizard is the program that is used to set up the dql file. The dql file is the file that contains the experimental parameters and settings. The steps for the setup of the dql file are as follows:

- Open the XRD Wizard Icon, select New then XRD Non Ambient
- Click on Methods, then XRD Non Ambient then enter the details:
  - Operator : Michelle
- Check the Diffractometer Settings
- Check the Beam optics
- Check that the Detector Selection is PSD Vantec with a 3˚ window setting
- Click on the Method tab to expand window and enter:
  - Scan parameters
  - Check the generator
  - Check the
  - Enter the Z value in the drives section.

The Z value is usually determined through the use of National Institute of Standards and Technology (NIST) Silicon standard reference material 640c (SRM_640c, 2012). There are published values for where the peaks should be and therefore a peak can be used to ensure that the sample is at the accurate height for analysis otherwise the resultant pattern will have shifted peaks. The NIST Silicon peak usually used for this is the two theta 28.4409˚ peak. This peak belongs to the {111} silicon reflection. The process involves a trial and error setup by entering various values and carrying out data scans

focusing on the selected reflection. Once the right value has been found, it can now be used for creating a new dql file when setting it up or adjusting an existing value in a dql that may have been set up already.

- Click the Profile Table and create the temperature profile that the experiment must follow. After entering all the information needed here, check for any exclamation marks that signal an error or a possible problem in the profile.
- The profile can now be saved as a dql file ready for use by the XRD Commander that controls the diffractometer. A graphical representation of the profile may be viewed by clicking on Profile Table.

Note: It is advisable to exit the screen and reopen the file to check that there are no errors and that all the information that was entered is accurate.

3.1.3 How to run an experiment on the Bruker D8 Advance

This is all carried out using the XRD Commander program. To begin an experiment click on Jobs, then on Create Jobs. Enter the sample name, like $BaPbO_3$ based on what you will be analysing, into the Sample ID section. In the Parameter file section, select the dql that was created using the XRD Wizard. In the Raw file section, enter the destination and the file name that the resultant powder pattern should be saved as. In the Script section, select Measure.vbs and in the Mode section, select QL. Once all this information has been entered, open the bottom front panel of the D8 diffractometer and turn on the heater and the cascade. Once these have been turned on, then select Start and begin the experiment.

If gases are being used in the run, it is important that a room temperature pattern be run first without any gas flowing, and then run another scan with the gas flowing. Once this is done, compare the intensities of the peaks as well as whether or not the pattern looks the same. Doing this before the start of the VT-experiment shows if the gas has blown off some of your sample or not. The gas flow rate used in the experiments that utilised gas flow in this study was 1 $ml.sec^{-1}$.

3.2 Benchmarking and Calibrating the Bruker D8 Advance Diffractometer and XRK

Benchmarking and calibrating instruments is important as it minimises systematic errors in primary and derived results. Additionally it would provide an early warning of a potentially serious problem. Benchmarking was carried out at the beginning of this work and therefore all the data presented is based on the benchmarked configuration of the instrument.

The Bruker D8 Advance is equipped with a VÅNTEC PSD detector that was used with an angular opening of 3˚ 2θ though the detector can collect data up to 12˚ 2θ window range. This value was selected as it gave the best compromise between resolution and intensity. In the event that a wider angular opening is used, then a loss of resolution is observed though shorter data collection periods are possible.

Other instrumental parameters also needed to be optimised and for this, the National Institute of Standards and Technology (NIST) LaB_6 standard reference material was

used. The material is deep violet in colour and has a fine powder texture. This sample is also referred to as standard reference material 660a (SRM_660a, 2012). This sample is accompanied by a certification detailing the preparation as well as the careful determination of the cubic lattice parameter (4.1569162 Å) using a Cu incident X-ray beam of λ = 1.5405929 Å. A copy of the certificate can be obtained from NIST on the internet (SRM_660a, 2012).

LaB_6 is appropriate for investigating the effects of varying fixed divergence slits, count time and step size due to its inherently narrow diffraction lines. An important unique property of LaB_6 is that it shows instrument broadening and does not show sample broadening. This investigation was carried out to obtain the best combination of count time and size of the fixed divergence slits to give optimum collection time with the best resolution.

The {110} reflection of the LaB_6 was measured using four different slit sizes while keeping the count time constant. It was observed that narrower slits gave better Cu $K\alpha_1/K\alpha_2$ doublet resolution while the loss in intensity was severe. The conclusion of this investigation was that the 0.02 mm slit gave the best compromise between intensity and resolution. The 0.6 mm slit would only be necessary in cases where the sample is investigated in conditions that weaken the X-ray beam or if the sample itself diffracts poorly.

Counting time also has an effect on the resolution of the Cu $K\alpha_1/K\alpha_2$ doublet. With this investigation, the slit size of 0.02 mm was used while varying the counting time. It was observed that better resolution of Cu $K\alpha_1/K\alpha_2$ doublet was seen when the counting time

was increased. The conclusion of this investigation illustrated that though all the measurements carried out gave partial resolution, only the counting time 0.75 s/ 0.014˚ 2θ gave two distinguishable peaks and therefore acceptable resolution of the Cu $K\alpha_1/K\alpha_2$ doublet.

The next investigation was for a suitable step size. It was found that the smaller the step size, the better the resolution. Based on all these investigations all measurements used a 0.6 mm fixed divergence slit, with a count time of 0.5 s and a 0.028˚ 2θ step size. Though the optimal values were not used as determined, the best compromise is found when these values are used.

After obtaining the optimal step size, count time, fixed divergence slit size and angular opening of the VÅNTEC detector, an investigation was performed to reliably determine the line position with both precision and accuracy. The NIST LaB_6, SRM_660a (2012), was used for this investigation as well. Some potential causes for incorrect line positions include misalignment of the diffractometer's goniometer, sample specific deviations like atomic dislocations as well as strain caused lattice parameter changes. The investigative study involved a Rietveld refinement of the NIST LaB_6 SRM_660a (2012). In the study, a total of 9 independent parameters were refined: one histogram scale factor, crystallite size, one lattice parameter, a single fundamental peak shape parameter describing the overall peak shape profile, a second order Chebychev background polynomial, a description for absorption correction and zero set point correction.

The results of this refinement showed that the diffraction data has large 2θ dependence and it fits a second order polynomial. 130˚ 2θ gave the largest peak deviation. The lattice parameter deviation of the NIST LaB_6 was found to be a negligible -0.029% while the peak position deviation was a negligible 0.030%. Therefore it was concluded that the contribution of the instrument to shifts in line positions is minimal and so the instrument alignment is acceptable.

The D8 Advance is set up with a Göbel mirror and a 2.5˚ Söller slit on the primary beam side as well as a 2.5˚ radial Söller slit on the secondary beam side for all powder X-ray analysis carried out on the D8 for this study.

3.2.1 Investigation of the Bruker D8 Advance with XRK

Variable temperature X-ray analysis is an important technique in this study and therefore in order to draw the most reliable conclusions, the temperature reported by the XRK had to be calibrated. The calibration involved checking the accuracy of the temperature.

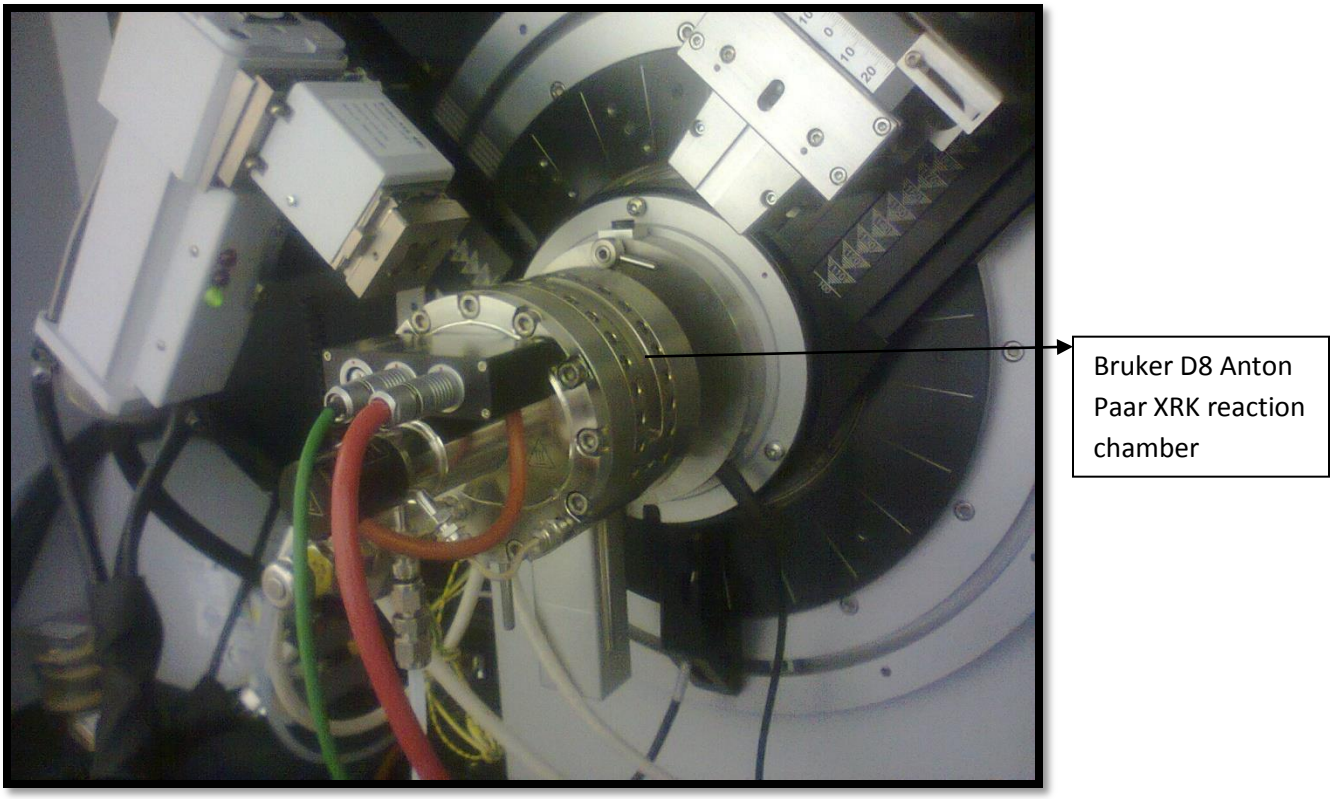

Figure 3.3: Picture of the Bruker D8 XRK diffractometer showing the Anton Paar reaction chamber which heats up to a maximum temperature of 900 ˚C.

The thermocouple is located approximately 2 mm from the outer edge of the sample holder. The distance, though small, leads to the possible difference in the recorded temperature of the thermocouple compared to the actual temperature of the sample in the sample holder. NIST 640c silicon standard reference material (SRM_640c, 2012) was used for the calibration of the thermocouple because its thermal properties including its thermal expansion coefficient are well known (Okada & Tokumaru, 1984). The NIST 640c silicon has a simple cubic crystal structure. A variable temperature dataset was collected from 30 ˚C – 900 ˚C. The first two data scans were at 30 ˚C and 50 ˚C from there, data was collected every 50 ˚C. Once the sample was at 900 ˚C, the system is allowed to cool down and a final data scan was collected at 30 ˚C. The final

scan at 30 °C was done to investigate what phase of silicon was obtained after all the variable temperature measurements.

Phase verification was carried out using the Bruker DIFFRAC EVA software (2010) and Rietveld refinement was carried out using the TOPAS (Coelho, 2007) software. It was confirmed that the powder was one pure phase of silicon with the space group Fd-3ms. This one phase of the standard silicon powder was observed at all the temperatures as well as in the final scan carried out after cooling.

The Rietveld refinement of the data that was obtained was carried out sequentially. The parameters that were refined are the 2^{nd} order Chebychev background function, scale factor, unit cell parameter, crystallite size, fundamental approach for peak shape parameters, sample displacement correction and absorption.

The refinement showed good correlation with the results presented by Okada and Tokumaru (1984) as reflected graphically in Fig 3.4. In their investigation, they investigated the precise determination of the thermal expansion coefficient and the lattice parameter of silicon between 27 ˚C and 1227 ˚C. The results of the refinement between the observed data and that presented by Okada and Tokumaru gave an average R_{wp} of 12.680 and an average χ^2 of 1.68. A graph was plotted to represent the small difference in the lattice parameters observed and those that were documented by Okada and Tokumaru (1984).

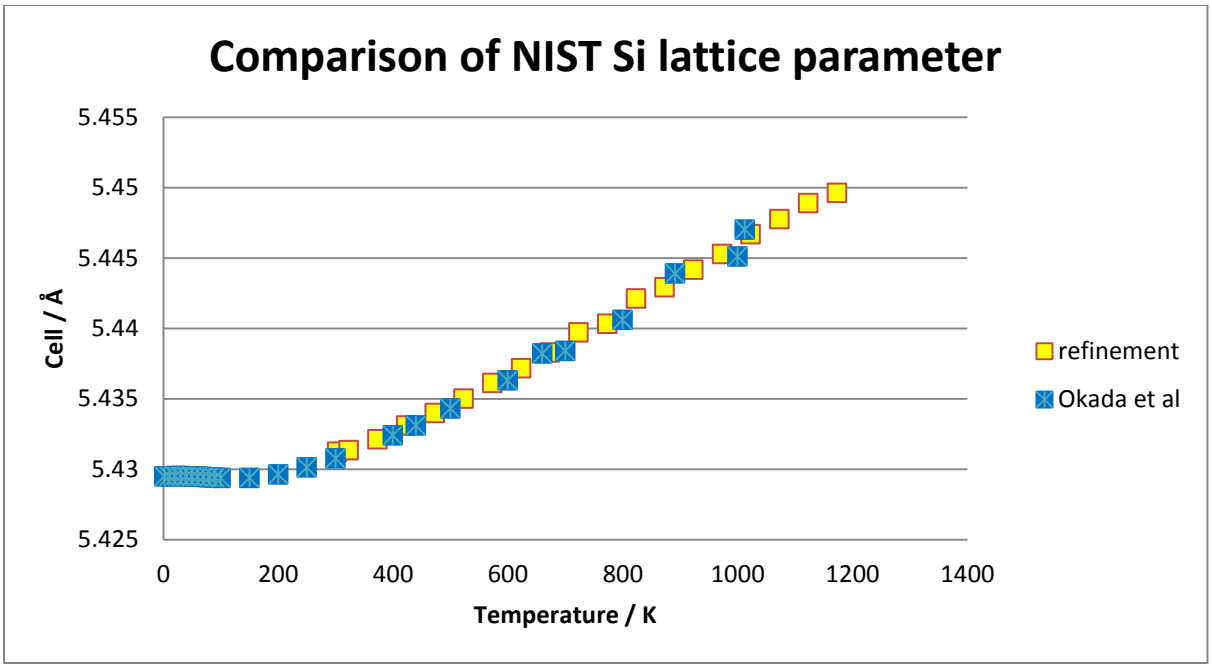

Figure 3.4: A plot of the observed NIST Si SRM 640 diffraction data over the 0-1200 K range compared with the Okada & Tokumaru (1984) experimental Si lattice parameter over the 300-1500 K against temperature.

The results obtained from the calibration of the XRK showed that the instrument was recording reliable temperatures that could be reported as accurate.

3.3 References

Coelho, A.A.; *Topas v4.2: General Profile and Structure Analysis Software for Powder Diffraction Data,* Bruker AXS, Karlsruhe, **2007**

DIFFRAC.EVA: *The Next Era in Phase Analysis,* Bruker AXS, Karlsruhe, **2010**

Macor®: http://www.astromet.com/macor.htm (Last accessed 15 March 2013)

National Institute of Standards and Technology (NIST) Silicon Standard Reference Material 640c (SRM_640c), https://www-s.nist.gov/srmors/view_detail.cfm?srm=640c (Last accessed 10 September 2012)

National Institute of Standards and Technology (NIST) LaB_6 Standard Reference Material 660a (SRM_660a) https://www-s.nist.gov/srmors/view_detail.cfm?srm=660a (Last accessed 10 September 2012)

Okada, Y., Tokumaru, Y.; *Journal of Applied Physics* **1984**, 56, 314-320

Chapter Four: Thermal responsive behaviour of a Niobium Tungstate

4.1 Introduction

Previous research relating to the preparation and the properties of materials in the tungsten-oxide system, also known as niobium tungstates or tungsten niobates includes reports by Van Uitert et al. (1968) and Winter & Clarke (2007). A number of niobium tungstates structural studies found that many of these are based upon a tetragonal tungsten bronze (TTB) subcell (Winter & Clark, 2007; Fourquet et al., 1988). In essence the tetragonal bronze structure is based on a two-dimensional network made up of corner-sharing octahedra which extend by corner sharing into the third direction. The result of these networks is the formation of 3-, 4- and 5-membered rings which become tunnels or channels extending throughout the structure. The tunnels may be empty, partially filled or fully filled and this leads to some interesting properties (Van Uitert et al., 1968; Yu et al., 2008). Various cations may fill these tunnels and the choice of cation is dependent on the coordination of the cation that it will have as well as the size of the tunnel (Stephenson, 1968). The TTB structure itself is made up of a framework of corner sharing octahedra that has tunnels of pentagonal, trigonal and square shapes extending along the short crystallographic c axis, shown in Figure 4.1 (Krumeich et al., 2000). The TTB type is a ReO_3-related structure type and thus associated with tunnels of different shapes appearing in the framework of the corner sharing MO_6 octahedra. The TTB structure type was assigned due to the incorporation of metal atoms in the

tunnels implying a reduction when compared to WO_3 (Sayagués et al., 1999). Obayashi and Anderson stated that "the skeletal framework of tetragonal tungsten bronze structure is almost always perfect" (Obayashi & Anderson, 1976, page 82).

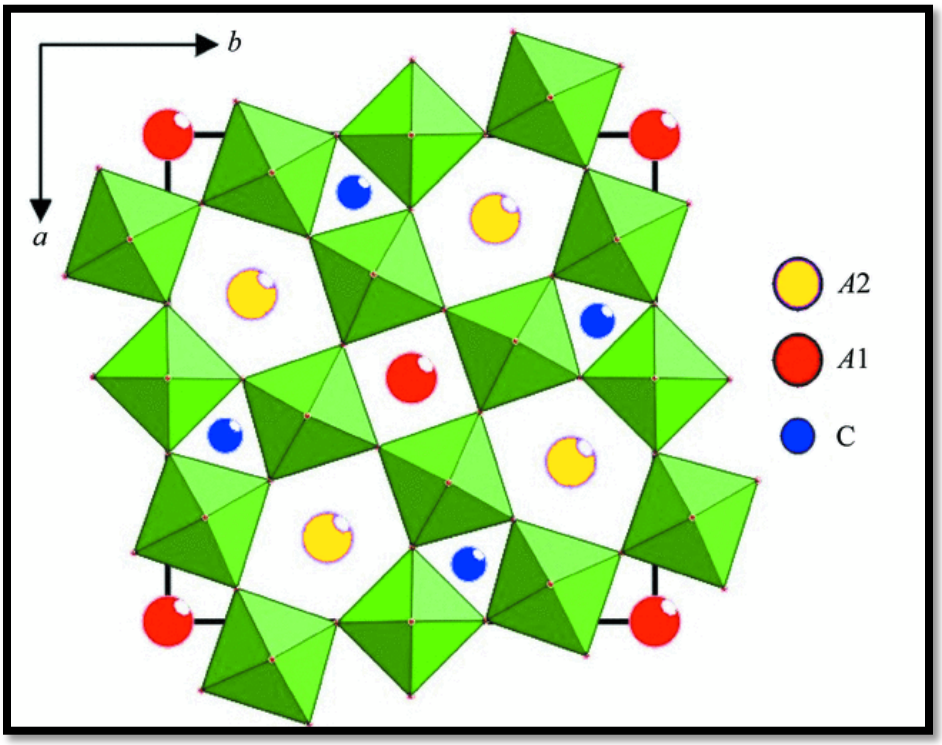

Figure 4.1: Illustration of the crystal structure of the Tetragonal Tungsten Bronze (TTB). The A2, A1, C show the pentagonal, square and trigonal tunnels respectively that are all present in the TTB structure.

Stephenson suggested that single phase Nb/W oxides from the $Nb_2O_5.WO_3$-WO_3 region of the phase diagram are believed to have superstructures based upon the TTB in which case, some of the pentagonal tunnels are occupied by metal and/or oxygen atoms. As the pentagonal tunnels are filled, the structure becomes distorted, its

symmetry elements degenerate and the unit cell becomes larger in multiples of the basic tetragonal subcell (Stephenson, 1968).

Krumeich et al. (2000) found that they were able to synthesise the $Nb_8W_9O_{47}$ superstructure. It was reported that this material has an orthorhombic structure and crystallized in the $P2_12_12$ space group to give a threefold superstructure of the tetragonal tungsten bronze (TTB) type. This material represented a very stable phase in the pseudo-binary system Nb_2O_5/WO_3 and consequently, the structure was favoured in other systems as long as the oxygen/metal ratio is 47:17. One of the key features of this structure is that if the M-O chains occupy the pentagonal tunnels, then the tunnels are almost regular pentagons whereas if they are not occupied, they are more distorted. The shifting of the atomic position out of the (001) and (002) planes cause the observed distortion of the polyhedra and varying M-O distances in the c-axis direction (Krumeich et al., 2000)

Boyd et al. (1980) used a niobium tungstate, approximately represented as $W_9Nb_8O_{47,}$ as an electrochromic material in an electro-optical device. They patented this device because it reflects colour changes that are induced electronically. An electrochromic material is a material that is susceptible to colour change due to application of an electric field and the colour change remains in the absence of the electric field. The colour change from the niobium tungstate ranges from a dark blue to a pale yellow. Applications of this material include its use in flat screen displays and optical filters (Boyd et al., 1980).

Sayagués et al. (1999) carried out experiments where their $Nb_7W_{10}O_{47}$ was heated by an electron beam in a gas atmosphere. The gases used in these experiments were O_2, He, H_2. Though these reactions generated a new niobium tungsten oxide, it was observed that the reaction did not alter the TTB superstructure. Though the TTB structure was maintained, some rearrangements of the empty and filled pentagonal columns occurred. The difference observed was the increase in the proportion of pentagonal tunnels occupied by metal-oxygen strings. During the irradiation, the change in the niobium tungsten oxide product is seen in that; part of the tungsten oxide was being etched away and condensing as small particles near the irradiated crystallite. It was suggested that the product obtained from the reaction was not thermodynamically stable but is rather kinetically stable (Sayagués et al., 1999).

A variety of synthetic methods for the preparation of niobium tungstates have been suggested in various studies carried out by different research groups. Krumeich et al. (2000) synthesised the $Nb_7W_{10}O_{47}$ superstructure by heating the molar ratio 3: 10: 1 of Nb_2O_5, WO_3 and NbO_2 with an $HgCl_2$ mineralizer at 1250 ˚C for three days (Krumeich et al., 1995 & 2000). England et al. (1982) synthesised a variety of Nb_2O_5-WO_3 compounds by weighing appropriate amounts of Nb_2O_5 and WO_3 and sealing them in platinum tubes. These tubes would then undergo heating for any period between 40 hours and 20 days at 1327 ˚C (England et al., 1982). Viccary & Tilley (1993) prepared niobium tungstates using appropriate proportions of Nb_2O_5 and WO_3 as well. Their synthetic technique involved grinding the starting compounds, pressing them in a steel die and heating initially for 11 days at 700 ˚C in a platinum crucible, followed by 4 days at 1200 ˚C (Viccary & Tilley, 1993). Obayashi and Anderson (1976) synthesised a range

of niobium tungstates. Their synthetic technique utilised suitable amounts of WO_3 and Nb_2O_5 which were finely ground and sealed in silica capsules for heating. The heating occurred in 3 stages which were 140 hours at 800 ˚C then 90 hours at 1050 ˚C and finally 94 hours at 1250 ˚C (Obayashi & Anderson, 1976). Makhura (2009) synthesised the mixed phases Nb_2WO_8 and $Nb_8W_9O_{47}$ by initially grinding together WO_3 and Nb_2O_5 and calcining the mixture for 48 hours at 1000 ˚C. The resulting product was pressed into green pellets for 30 secs at 10 bar. The pellets were then heated at 1300 ˚C for 4 hours (Makhura, 2009).

In the present study, the preparation started with $NbCl_5$ and H_2WO_4 and an intermediate product was formed via a precipitation method, followed by thermal treatment to get the final product.

4.2 Synthesis of $Nb_7W_{10}O_{47}$

2.482 g of $NbCl_5$ (yellow crystalline powder) was dissolved in 20 ml of absolute ethanol in a 50 ml beaker and set aside. This gave a yellow initial solution that went colourless as it effervesced. The solution heated up spontaneously showing that, as it dissolved, it underwent an exothermic reaction. 1.140 g of H_2WO_4 (yellow powder) was placed into another 50 ml beaker with 10 ml absolute ethanol. This gave a yellow suspension. To this beaker, NH_4OH was added dropwise while stirring until the H_2WO_4 dissolved. A total amount of 6 ml NH_4OH was added thus resulting in a paler yellow milky solution. The niobium ethoxide ($NbCl_5$ + C_2H_5OH) prepared above was then added to this solution with vigorous stirring and this resulted in a white suspension. White fumes were

given off when the solutions were mixed (Figure 4.2). No other distinct smell was detected as there was a strong smell from the NH_4OH. The mixture was allowed to stand in a fume cupboard for 12 hours to allow the solvent (ethanol) to evaporate.

Figure 4.2: White fumes seen escaping the beaker after the two solutions were mixed while stirring vigorously.

A white precipitate was obtained and it was analysed by PXRD to determine the composition of the precipitate (Figure 4.3). The precipitate underwent heat treatment in order to drive off (decompose) the ammonium chloride precipitate and to crystallise the desired product.

In essence, the $Nb_{7-x}W_{10+x}O_{47}$ compound was successfully synthesised through an initial precipitation method followed by heat treatment. This precipitation method gave a white precipitate product which was analysed by PXRD at room temperature on the Bruker D2 Phaser diffractometer. The resultant powder pattern showed that crystalline

NH_4Cl was present in the precipitate (Figure 4.3) and that the desired product was not observed. This was confirmed through a search match that was carried out using the Bruker DIFFRAC EVA software (2010) for phase identification. The pattern obtained matched the 01-073-0365 from the PDF-2 database (Sirdeshmukh & Deshpande, 1970).

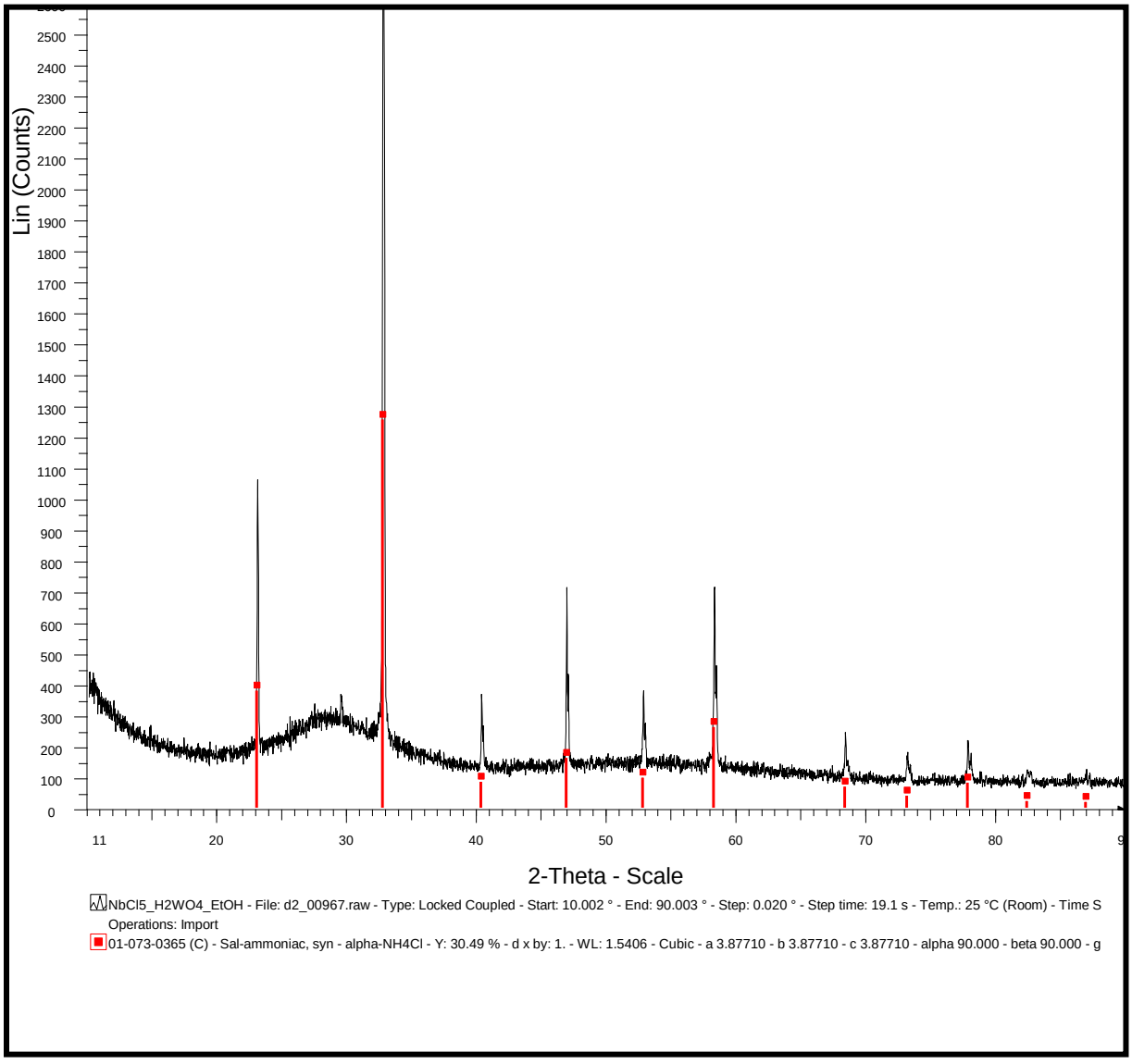

Figure 4.3: PXRD confirmation of the white precipitate as ammonium chloride. Background hump shape is indicative of amorphous or nano-sized materials.

It can only be assumed that the desired $Nb_xW_yO_z$ product is not crystalline or had not formed yet and therefore was not detected by the powder diffraction. A Rietveld refinement was carried out on the room temperature diffractogram measured on the Bruker D2 Phaser diffractometer. The difference curve (Figure 4.4) shows the good correlation between the observed and the calculated patterns confirming that NH_4Cl is present. An amorphous "hump" is seen in the observed pattern. It is proposed to be associated with the desired product and this is seen and explained more clearly in the results of the Continous Online X-ray Analysis (COXA) of the synthesis product. Due to this assumption, the amorphous contribution was excluded in the refinement so the results presented here are relative. The exclusion of the amorphous content peaks was carried out using a function in the TOPAS software (Coelho, 2007) during the Rietveld refinement process.

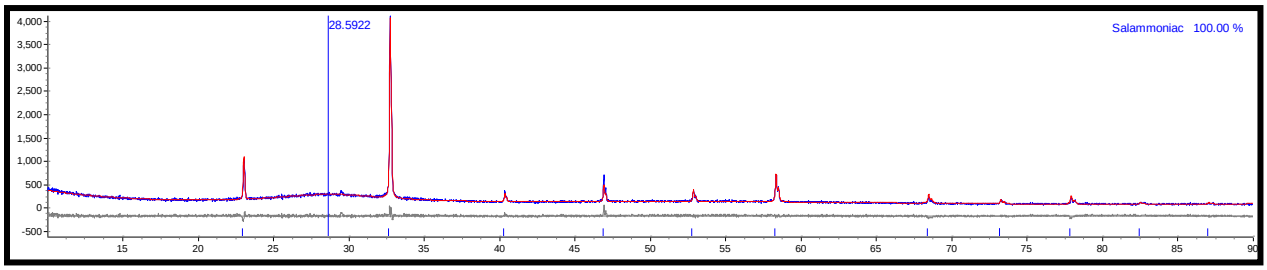

<u>Figure 4.4:</u> TOPAS difference plot output showing the observed pattern (blue), the calculated pattern (red) and the difference curve (grey)

The Sirdeshmukh and Deshpande salammoniac (NH_4Cl) structure was used as the starting model for the refinement (Sirdeshmukh & Deshpande, 1970). Figure 4.4 shows the graphical representation of how well correlated the observed and calculated

patterns are. The χ^2 (goodness of fit) of this refinement is 1.23, the R_{exp} is 7.77 and the R_{wp} is 9.58. Using the formula for the calculation of the goodness of fit, we see that these values are accurate. This best fit is addressed by choosing Pseudo Voigt (PV_TCHZ) peak type with a 4th order polynomial for the background. The refinement did not include any major peaks that could not be accounted for by the model used for the refinement. The space group for the NH_4Cl is Pm-3m (Sirdeshmukh & Deshpande, 1970). The a lattice at the start of the refinement was 3.8771(2) Å and after the refinement was 3.8680(0) Å.

The precipitate was then subjected to an ex situ treatment regimen, in which complete PXRD diffractograms were recorded after heating in intervals of 100 ˚C. This heat treatment showed that the niobium tungstate could be formed at approximately 800 ˚C (Figure 4.5).

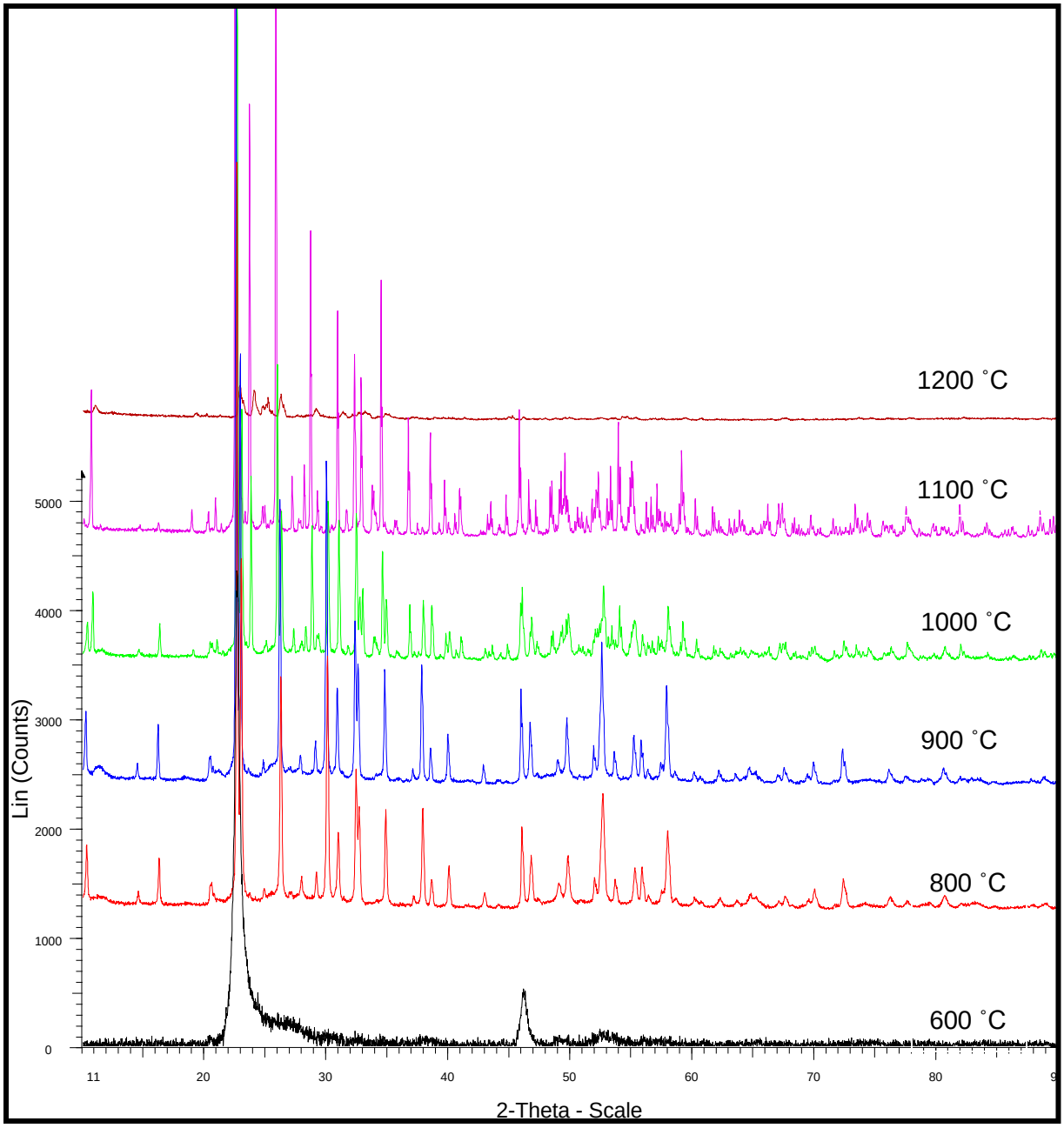

Figure 4.5: Ex situ product scans for heat treated product at 600 ˚C, 800 ˚C, 900 ˚C, 1000 ˚C, 1100 ˚C and 1200 ˚C. Formation of product occurs between 600 ˚C and 800 ˚C. The intensity of the scans was scaled down to 0.333 for the sake of using them clearly for comparison.

This finding showed an approximate temperature of formation of the niobium tungstate.

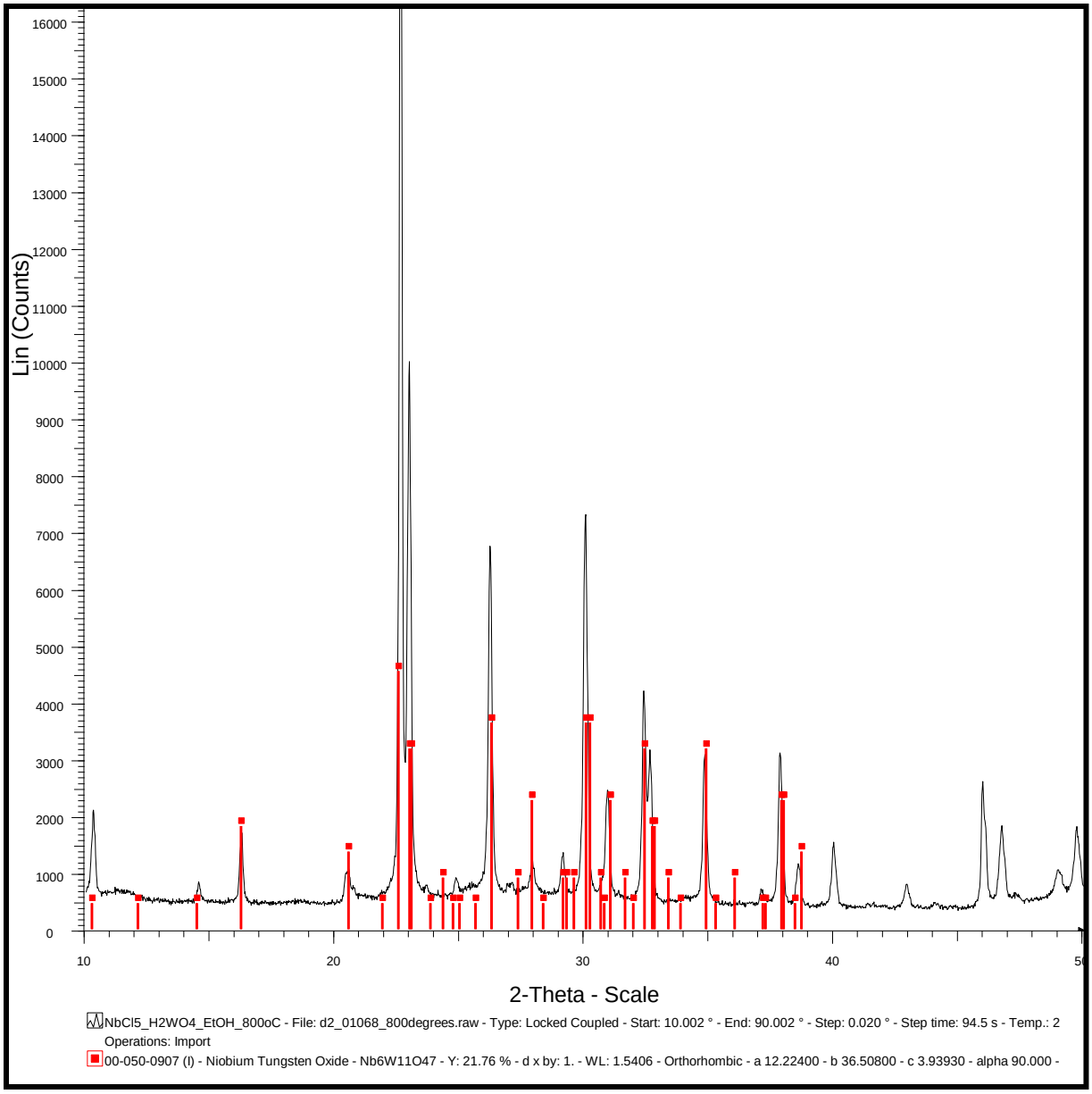

<u>Figure 4.6:</u> Diffractogram showing the measured pattern after heating to 800 ˚C with the matching Krumeich et al. Pattern from the PDF-2 database, recorded on the Bruker D2 Phaser diffractometer (Krumeich et al., 1995).

The phase identification showed that the heated powder contains only one phase and that phase is $Nb_6W_{11}O_{47}$ (Figure 4.6).

4.3 VT-XRD studies on $Nb_{6.7}W_{10.3}O_{47}$

An in situ VT-PXRD experiment was then set up of the heat treated white precipitate. The crystalline NH_4Cl containing white precipitate had been heat treated to 600 ˚C prior to the in situ experiment. This was done to ensure that all the NH_4Cl had been removed from the sample by decomposition as the melting point (decomposition) of NH_4Cl occurs at 338 ˚C (Ammonium chloride, 2012).

The COXA analysis involved heating the sample from 30 ˚C to 900 ˚C with 20 ˚C increments and a powder pattern being recorded at each temperature after the temperature increment. The analysis then included the sample being cooled down at 20 °C per run, from 900 ˚C back to 30 ˚C (Figure 4.7). The PXRD patterns were recorded at the various temperatures with a step size of 0.021˚ on a 10 - 90˚ range. The diffraction data were collected with a step size of 0.5s $step^{-1}$ on a Bruker D8 Advance diffractometer equipped with the Anton Paar XRK 900 reaction chamber and Vantec 1-D detector. A divergence slit of 0.6 mm and a receiving slit of 10.6 mm and Ni filtered Cu Kα radiation (40 kV, 40 mA) was used.

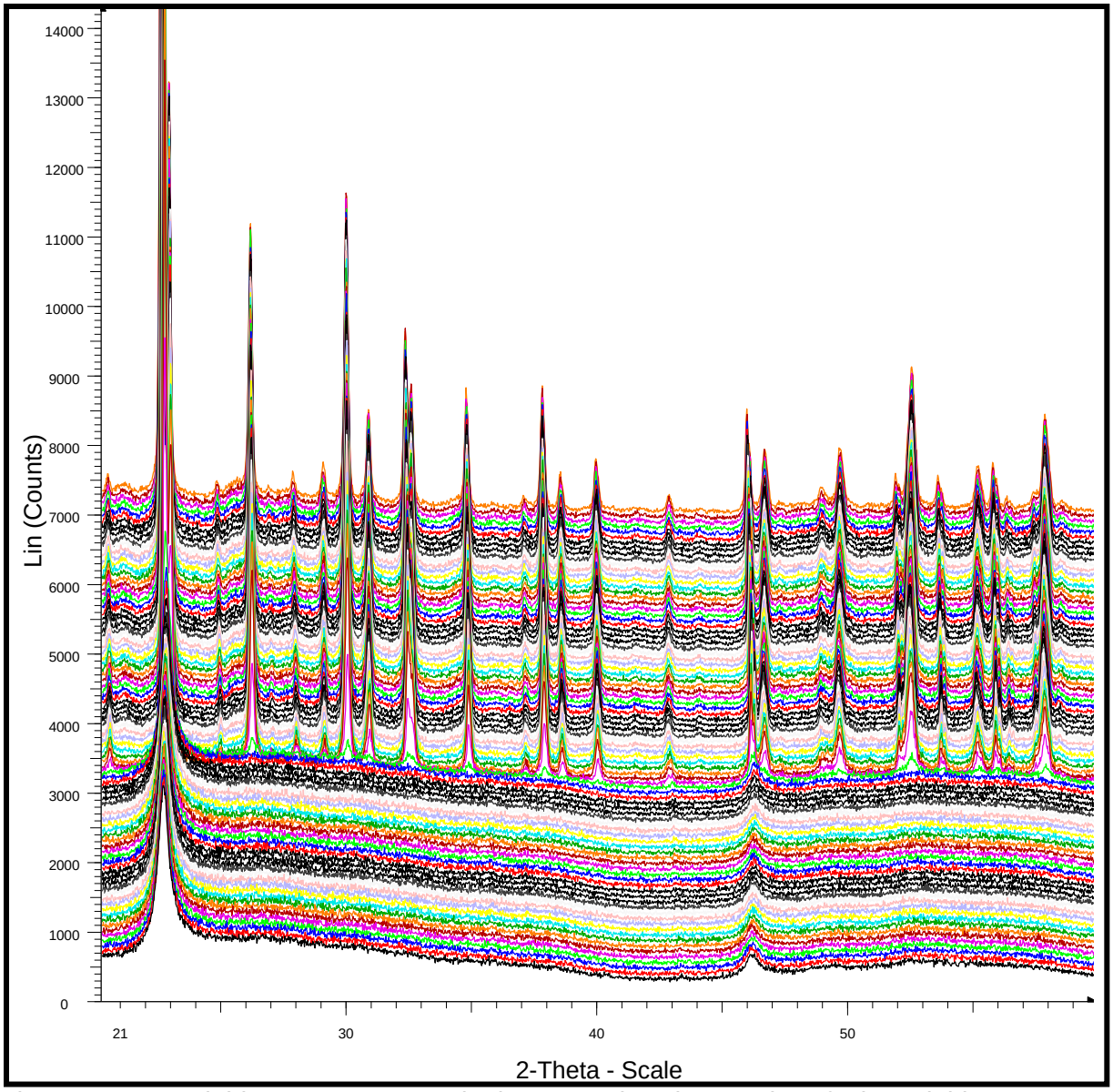

Figure 4.7: Variable Temperature (VT)–XRPD in situ study of the niobium tungstate synthesized. Pattern here shows heating up from 30 ˚C to 900 ˚C and the cooling back down to 30 ˚C using product that had been heated to 600 ˚C prior to the run to drive off all the $NHCl_4$.

Comparison of the final 30 ˚C XRD pattern for the synthesised niobium tungstate with the niobium tungstates in the PDF-2 database showed a match with $Nb_{6.7}W_{10.3}O_{47}$ (00-050-0907) (Krumeich et al., 1995).

The patterns observed from the start of the COXA analysis till 770 ˚C show two broad peaks. The broadness of the peaks suggests that the peaks are the result of amorphous material. If this assumption is accurate, then the patterns observed at higher temperatures result from the crystalline product forming and diffracting better which is why the peaks are sharper.

The COXA analysis showed that the crystallization of the niobium tungstate initiated at 770 °C. This niobium tungstate phase remained stable from its point of formation at 770 ˚C to the maximum temperature (900 ˚C). The phase is stable and does not change during the cooling.

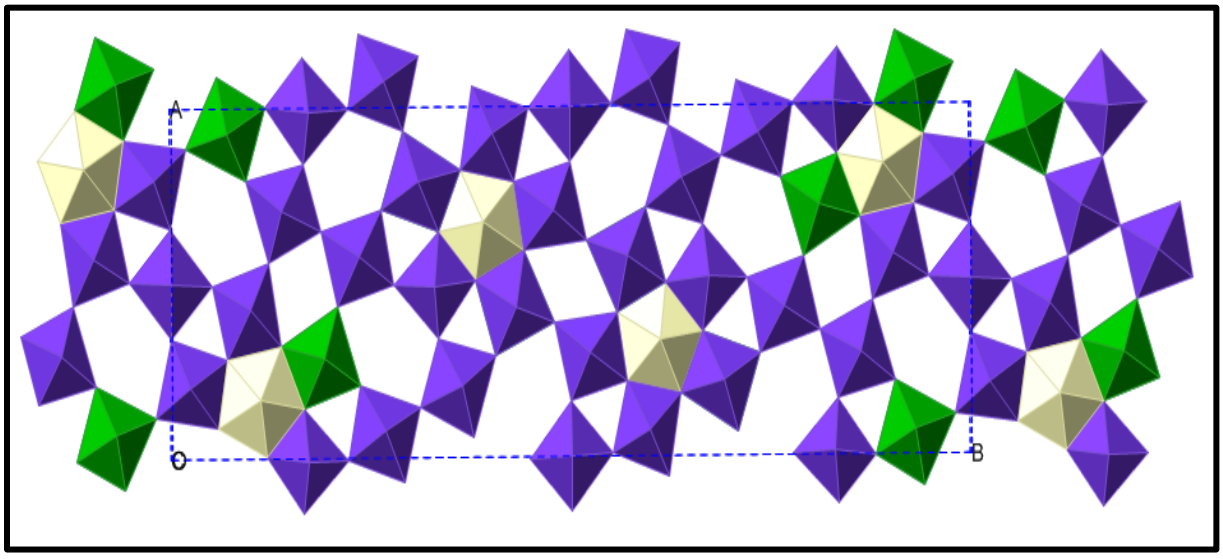

<u>Figure 4.8:</u> $Nb_{6.7}W_{10.3}O_{47}$ showing its TTB structure that has trigonal, square and pentagonal tunnels viewed along the crystallographic c axis.

The crystal structure of the $Nb_{6.7}W_{10.3}O_{47}$ used to generate the structure shown above, in Figure 4.8, had the refined cell parameters a = 12.2567(18) Å, b = 36.633(6) Å & c = 3.9496(6) Å. It crystallises in the orthorhombic space group $P2_12_12$.

Another VT-PXRD experiment was carried out. This experiment used a sample of the niobium tungstate that had been heat treated to 770 ˚C ex situ and where the niobium tungstate product had already formed. This data collection was carried out to investigate the stability of the phase formed as well as to determine the thermal expansion coefficient of the phase.

The heat treatment of the resultant precipitate to 770 ˚C, produced the desired product as shown in Figure 4.9. Figure 4.9 is the room temperature scan of the heat treated product while passing N_2 gas over the sample. This is the sample that was used to investigate the coefficient of thermal expansion (CTE) of the product.

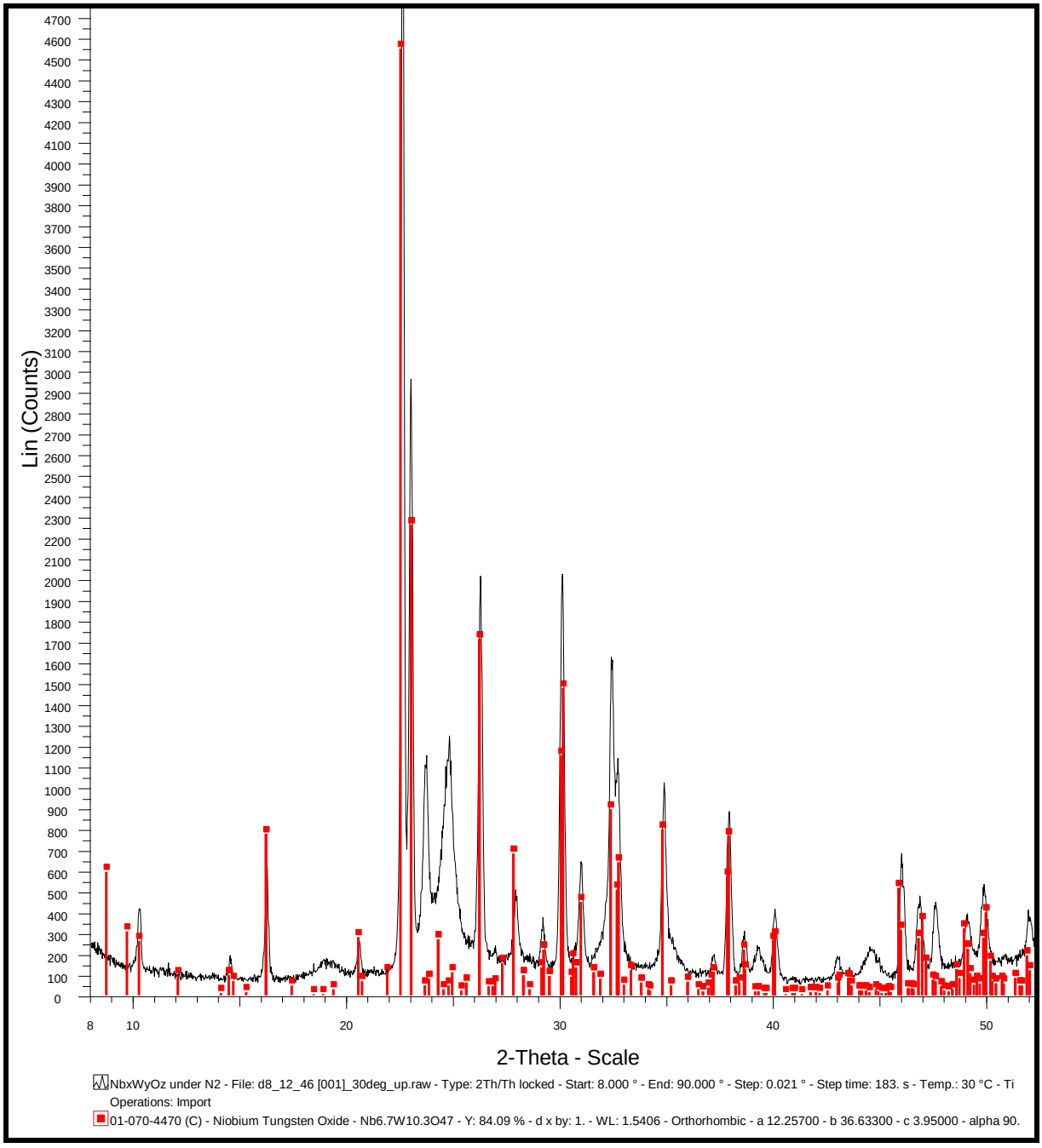

<u>Figure 4.9:</u> Heat treated white precipitate reflecting the synthesis of the desired crystalline product.

A colour change was observed in the material that was heated in situ to 770 ˚C. It went from being a white powder to a dark blue powder. Initially, it was suspected that the

sample had been contaminated but after further investigation, it was found that the colour of the product matched that of the one observed by Krumeich et al. (2000). The difference is that they had synthesised single crystals but the product obtained here was a crystalline powder. The difference observed may have arisen from the different synthesis technique used, though the same product was obtained. This same colour change was also observed by Boyd et al. as stated in their patent in 1980 (Boyd et al., 1980). The most plausible explanation of the colour change is that a reduction occurred during the in situ analysis of the product.

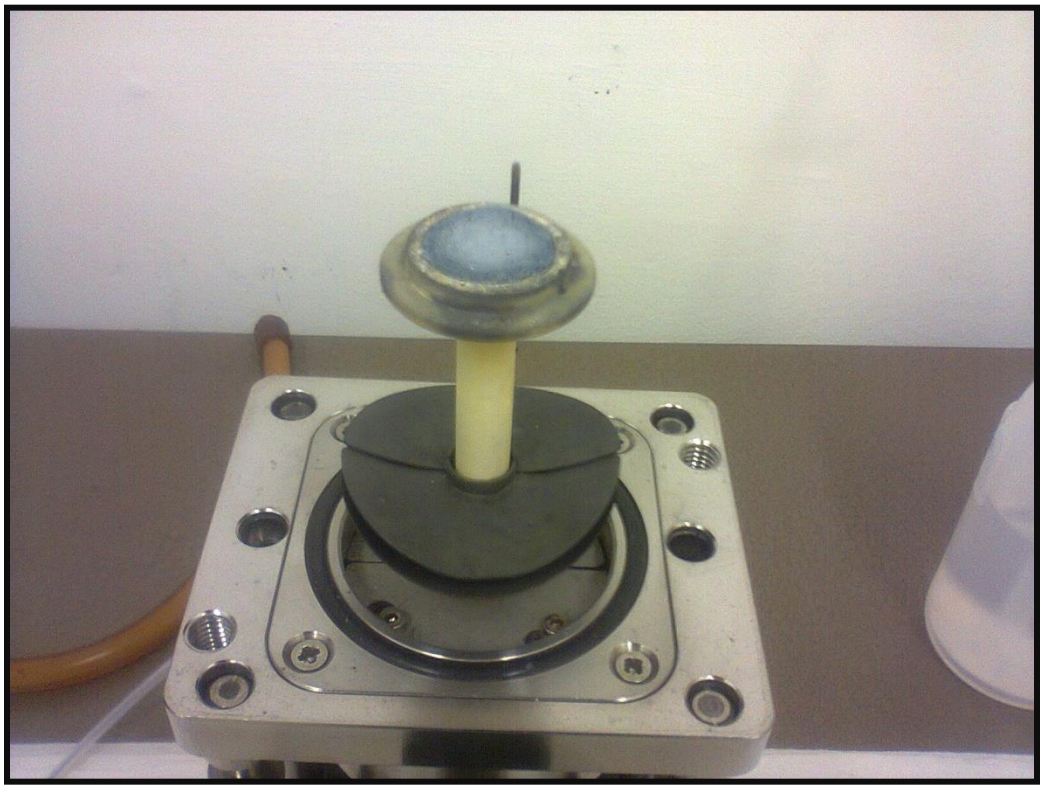

Figure 4.10: Bruker D8 Advance sample holder with the product after the COXA analysis showing the dark blue product.

The Rietveld refinement was carried out to confirm the qualitative observations. The refinement involved use of the $Nb_{6.7}W_{10.3}O_{47}$ as the starting structure (Krumeich et al., 2000). The results of the refinement of the 30 ˚C pattern collected in the Variable Temperature-Powder X-Ray Diffraction (VT-PXRD) experiment are given in the table 4.1.

- Table 4.1: Structural parameter refinement results for $Nb_{6.7}W_{10.3}O_{47}$

Space group	P21212
Lattice parameters	
a (Å)	12.258(2)
b (Å)	36.764(7)
c (Å)	3.942(1)
R_{Bragg}	12.494
R_{wp}	23.18
GOF	3.41
Cell Volume ($Å^3$)	1776.6
Cell Mass	6536.4
Crystal Density (g/cm^3)	6.109

Figure 4.11 and 4.12 show the VT-PXRD data collected from 30˚C up till 900˚C and back down to 30˚C as an overlay and in 3D view respectively. Rietveld refinements allow for reliable determination of the lattice parameters and therefore enable the determination of the thermal expansion coefficient. To facilitate the Rietveld refinement,

the combined data file containing 74 scans was separated into individual scan files using DIFFRAC EVA (2010). This limited accidental error when the refinements were carried out in a sequential manner (Styles et al., 2010). This is when the refined structure model from a scan at a particular temperature was used as the starting structure of the subsequent temperature. As no phase changes were observed, no significant alterations were required as the refinements were carried out. This is why this method is called sequential Rietveld refinement (Styles et al., 2010). The refinement values obtained from the data shown in Figure 4.11 and 4.12 are tabulated in Table 4.2 below.

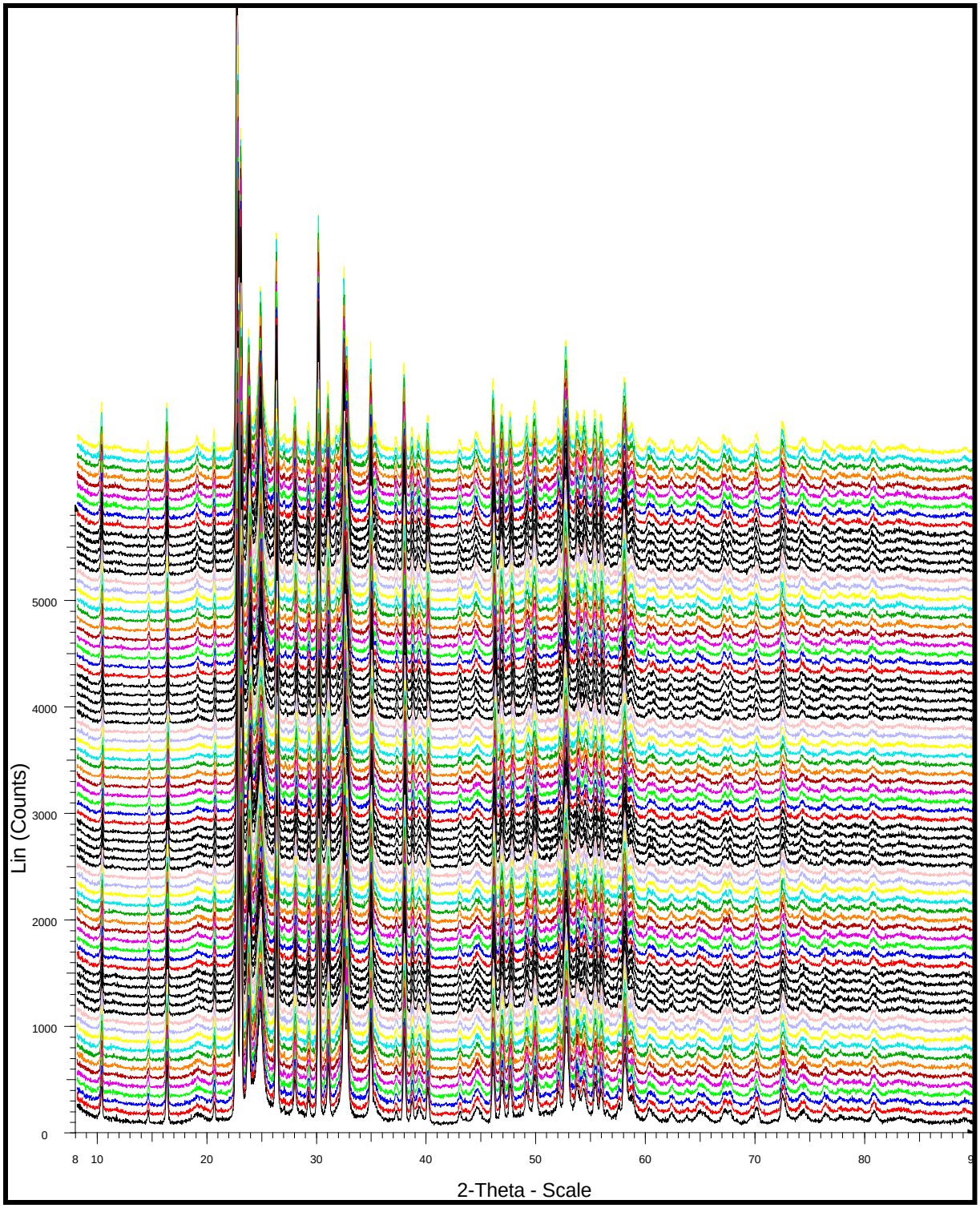

<u>Figure 4.11:</u> Heat treated product's VT-PXRD experiment used to study the thermoresponsive behaviour of $Nb_{6.7}W_{10.3}O_{47}$ to calculate the coefficient of thermal expansion. Starting

temperature is 30 ˚C and increases in 20 ˚C increments up till 900 ˚C then cools down at a rate of 30 ˚C.

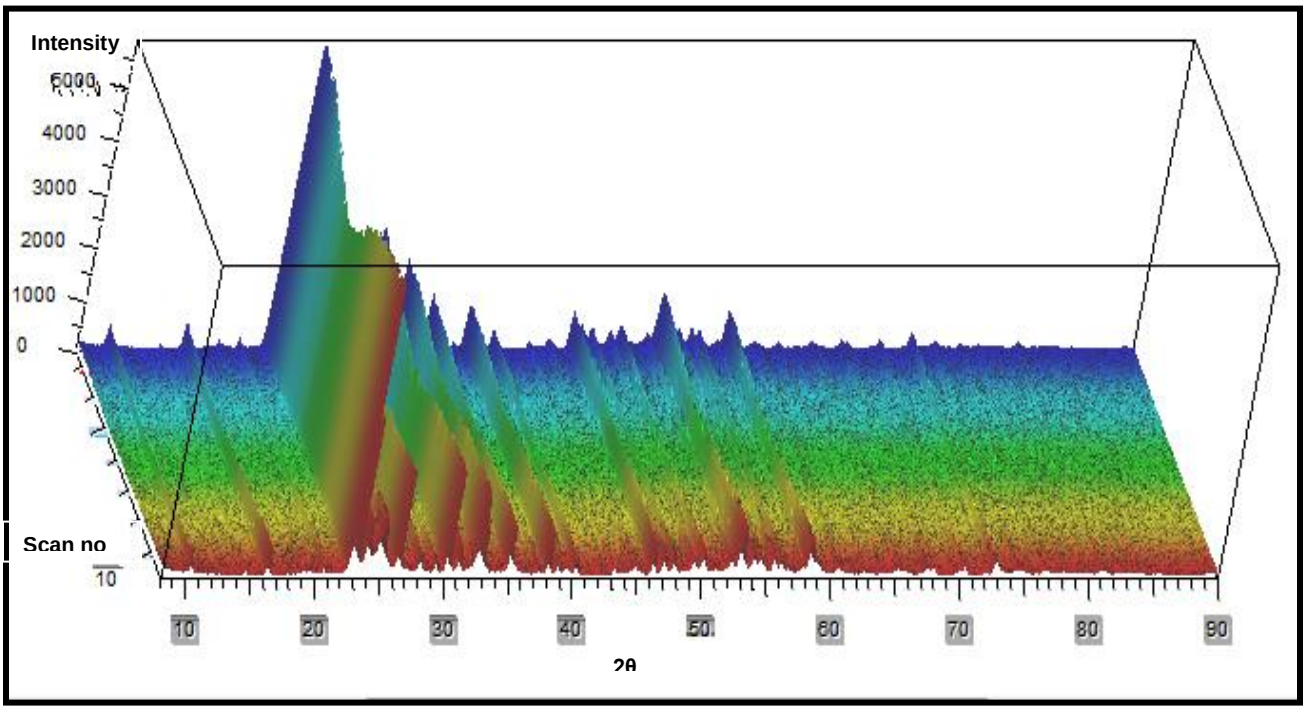

Figure 4.12: 3D view of the $Nb_{6.7}W_{10.3}O_{47}$ thermal expansion VT-PXRD analysis. View shows the absence of any phase changes and the stability of the product throughout the entire variable temperature experiment.

Table 4.2: Rietveld refinement results from the COXA analysis of the raw data d8_12_46.raw, which is the 2nd VT-PXRD experiment.

Temp. (˚C)	a (Å)	b (Å)	c (Å)	Cry size (nm)	GOF	R_{exp}	R_{wp}
30	12.258013(8)	36.766433(5)	3.941974(2)	100.7	3.42	6.8	23.26
50	12.258505(4)	36.767085(5)	3.941832(1)	99.1	3.4	6.79	23.11
70	12.258505(4)	36.767085(5)	3.941832(1)	99.1	3.44	6.81	23.45
90	12.258505(4)	36.767085(5)	3.941832(1)	99.1	3.42	6.82	23.3
110	12.260092(6)	36.769986(7)	3.941423(2)	109.1	3.4	6.83	23.21
130	12.260660(7)	36.769729(1)	3.941238(5)	107.9	3.37	6.85	23.1
150	12.260660(7)	36.769729(0)	3.941238(5)	107.9	3.4	6.85	23.26
170	12.262190(5)	36.770791(9)	3.940694(8)	108.2	3.38	6.87	23.2
190	12.262190(5)	36.770791(9)	3.940694(8)	108.2	3.41	6.88	23.45

210	12.263017(5)	36.771500(5)	3.940282(3)	110.4	3.41	6.9	23.55
230	12.263018(9)	36.771501(9)	3.940280(9)	110.4	3.35	6.91	23.15
250	12.265628(0)	36.784804(1)	3.940487(3)	106.3	3.37	6.92	23.31
270	12.265628(1)	36.784804(0)	3.940487(3)	106.3	3.37	6.94	23.4
290	12.267197(5)	36.787043(6)	3.939978(7)	105.8	3.37	6.96	23.47
310	12.267197(5)	36.787043(7)	3.939978(7)	105.8	3.39	6.98	23.67
330	12.268918(3)	36.795494(7)	3.939397(3)	106.9	3.32	7	23.25
350	12.270217(0)	36.799898(5)	3.939553(6)	102.9	3.36	7.01	23.53
370	12.272869(9)	36.811989(3)	3.939835(4)	102.3	3.34	7.03	23.5
390	12.272869(9)	36.811989(3)	3.939835(4)	102.3	3.33	7.04	23.45
410	12.272869(9)	36.811989(3)	3.939835(4)	102.3	3.31	7.05	23.35
430	12.274573(4)	36.821284(9)	3.939426(8)	102.2	3.31	7.05	23.37
450	12.274573(4)	36.821284(9)	3.939426(8)	102.2	3.3	7.06	23.32
470	12.274573(4)	36.821284(9)	3.939426(8)	102.2	3.32	7.07	23.48
490	12.274573(4)	36.821284(9)	3.939426(8)	102.2	3.29	7.09	23.35
510	12.274573(4)	36.821284(9)	3.939426(8)	102.2	3.31	7.11	23.56
530	12.279741(3)	36.830789(5)	3.940087(3)	113.1	3.23	7.15	23.08
550	12.280757(2)	36.830482(1)	3.939958(1)	110.8	3.24	7.19	23.33
570	12.280648(7)	36.830069(2)	3.939851(7)	111.2	3.19	7.23	23.04
590	12.281774(8)	36.841145(8)	3.940342(2)	138.4	3.19	7.27	23.21
610	12.281774(1)	36.841143(7)	3.940342(0)	138.4	3.18	7.33	23.3
630	12.281849(3)	36.837987(1)	3.939402(2)	140.7	3.14	7.42	23.32
650	12.282336(5)	36.836641(2)	3.939192(1)	143.3	3.09	7.49	23.15
670	12.282494(6)	36.832937(9)	3.938915(1)	143.3	3.1	7.54	23.36
690	12.282513(2)	36.832953(7)	3.938911(4)	143.2	3.11	7.57	23.53
710	12.286153(1)	36.834859(9)	3.938618(4)	147.1	3.05	7.61	23.2
730	12.287600(6)	36.840745(5)	3.938180(8)	150	3.05	7.63	23.29
750	12.287819(2)	36.841261(2)	3.938090(3)	149.9	3.07	7.66	23.54
770	12.291312(2)	36.847906(3)	3.937294(7)	148.3	3.08	7.69	23.67
790	12.291835(5)	36.849188(0)	3.937083(1)	149.3	3.05	7.72	23.54
810	12.295426(0)	36.858908(4)	3.936104(1)	146.9	3.04	7.74	23.55
830	12.295426(0)	36.858908(4)	3.936104(1)	146.9	3.07	7.78	23.87
850	12.304451(7)	36.883269(4)	3.935056(9)	155.3	3	7.78	23.38
870	12.304457(7)	36.883291(6)	3.935055(0)	155.3	3.03	7.81	23.67
890	12.310914(0)	36.901343(2)	3.933816(6)	159.2	3.02	7.83	23.65
900	12.310915(5)	36.901348(1)	3.933816(4)	159.3	3.05	7.84	23.93

The graphical representation of the results shown in Table 4.2:

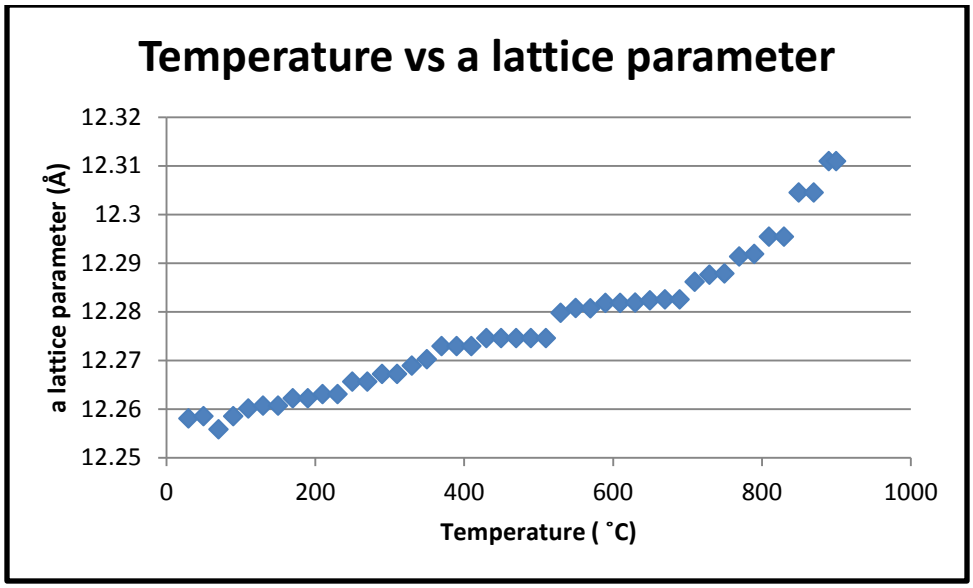

Figure 4.13: Thermal response of the a lattice parameter. The a lattice parameter increases as the temperature increases and therefore has positive thermal expansion.

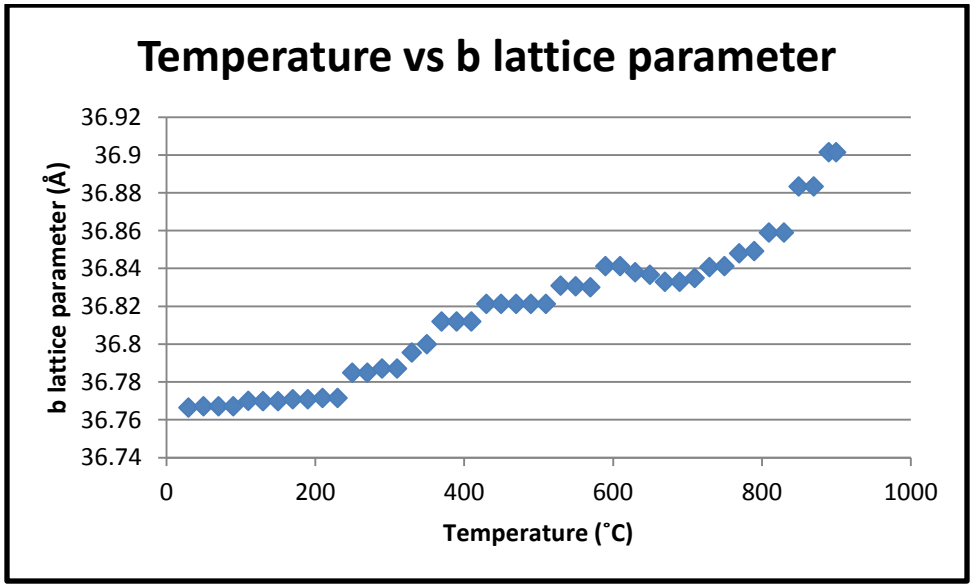

Figure 4.14: Thermal response of the b lattice parameter. The b lattice parameter increases as the temperature increases and therefore has positive thermal expansion. The b lattice parameter has a larger thermal expansion coefficient than the a lattice parameter.

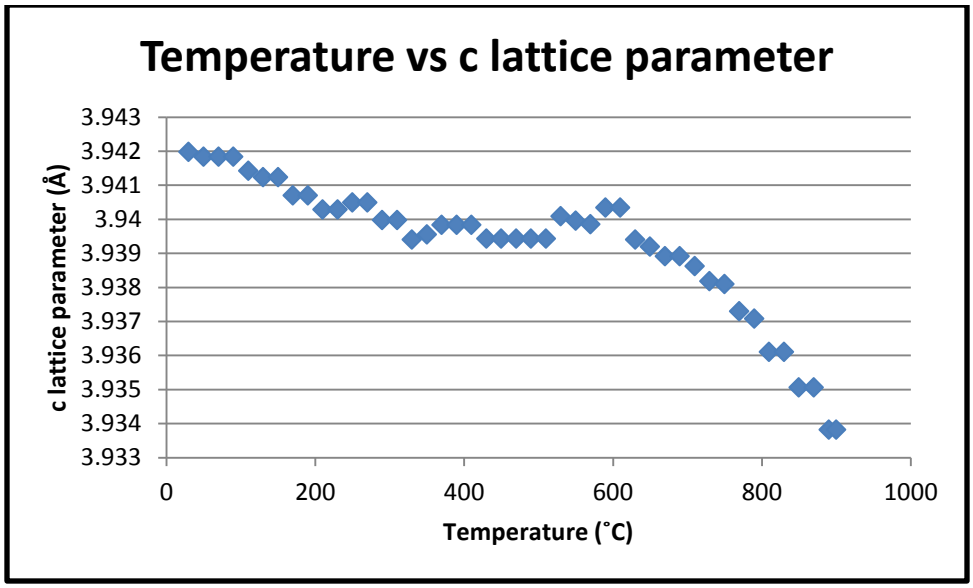

<u>Figure 4.15:</u> Thermal response of the c lattice parameter. The c lattice parameter decreases as the temperature increases and therefore has negative thermal expansion. Unfortunately the negative thermal expansion observed with c axis is not large enough for the product to have an overall negative thermal expansion coefficient.

The overall percentage change in the *a, b* and *c* lattice parameters is 0.43%, 0.37% and -0.21% respectively. Though the *c* lattice parameter decreases in size as the temperature increases, the *a* and *b* lattice parameters increase in length. This is an example of anisotropic thermal expansion. Though there is some thermal contraction, it is not sufficient to overcome the positive thermal expansion observed in the *a* and *b* lattice parameters and so low positive thermal expansion is observed. The niobium tungstate's mean volumetric coefficient of expansion found to be 6.704×10^{-6} $^{\circ}C^{-1}$ falls into the range for low thermal expansion materials (Holcombe, 1980).

4.4 Concluding comments

The COXA analysis showed that the crystallization of $Nb_{6.7}W_{10.3}O_{47}$ initiated at 770˚C. This phase remained stable from its point of formation at 770˚C to the maximum temperature (900˚C). The phase is stable and does not change during cooling.

The lattice parameter response to various thermal stimuli was monitored and it was found that there was positive thermal expansion in the a and the b axis direction. The c axis direction was found to undergo a negative thermal expansion. This is represented graphically in Figure 4.13 – 4.15. The unit cell volume was then determined for all the different temperatures and it was found that the overall volume increased as the temperature increased. The values obtained were then used to calculate the volumetric coefficient of thermal expansion. The mean volumetric coefficient of thermal expansion was found to be 6.704 x 10^{-6} $^{\circ}C^{-1}$. This value falls into the range used to describe low thermal expansion materials (Holcombe, 1980). In conclusion, the niobium tungstate that has been successfully synthesised is $Nb_{6.7}W_{10.3}O_{47}$ and it has a low positive coefficient of thermal expansion.

4.5 References

Boyd, G.D., Lemons, R.A., Phillips, J.C., Remeika, J. P., Spencer, E. G.; Tungsten Niobate Electrochromic Device, United States Patent 4225216, September 30, **1980**

Coelho, A. A.; *TOPAS* **2007**, V 4.2, Bruker AXS

DIFFRAC.EVA: *The Next Era in Phase Analysis*, Bruker AXS, Karlsruhe, **2010**

England, P.J., Booth, J., Tilley, R. J. D., Ekström, T.; *J. Solid State Chemistry* **1982**; 44; 60-74

Fourquet, J.L., Le Bail, A., Gillet, P.A.; *Mat. Res. Bull.* **1988**; 23, 1163-1170

Holcombe, C.E. Jr.; American Ceramic Society Bulletin **1980**, 59, 1219

http://en.wikipedia.org/wiki/Ammonium_chloride (Last accessed 29 February 2012)

Krumeich, F., Hussain, A., Bartsch, C., Gruehn, R.; *Z. Anorg. Allg. Chem.* **1995**; 621; 799-806

Krumeich, F., Wörle, M., Hussain, A.; *J. Solid State Chemistry* **2000**, 149, 428-433

Makhura, N.B.; M.Sc. Dissertation, University of Witwatersrand, Johannnesburg, **2009**

Obayashi, H., Anderson, J.S.; *J. Solid State Chemistry* **1976**, 17, 79-89

Sayagués, M.J., Hutchison J.L., Krumeich F.; *J. Solid State Chemistry* **1999**; 143; 33-40

Sirdeshmukh D.B., Deshpande V.T; *Acta Crystallogr. Sec. B* **1970**, 26, 295

Stephenson N.C.; *Acta Cryst.* **1968**; B24; 637-653

Styles, M.J., Riley, D.P., Madsen, I.C, Kisi, E.H. **2010**, "Parametric Rietveld Refinement Applied to In Situ Diffraction Studies" *34th annual condensed matter and materials meeting* http://www.aip.org.au/info/sites/default/files/cmm/2010/p18.pdf

Van Uitert, L.G., Levinstein, H.J., Rubin, J.J., Capio, C.D., Dearborn, E.F., Bonner, W.A.; *Mat. Res. Bull.* **1968**; 3, 47-58

Viccary, M.W., Tilley R.J.D.; *J. Solid State Chemistry* **1993**; 104; 131-148

Winter, M.R., Clarke D.R.; *J. Am. Ceram. Soc.* **2007**; 90, 533-540

Yu, S., Fan, H., Huang, H., Chan, H.L.W., Yu S.; *J. Appl. Phys.* **2008**; 104, 024101

Chapter Five: Thermoresponsive behaviour of tantalum tungstates ($Ta_xW_yO_z$)

5.1 Introduction

Some of the interest in polycrystalline tantalum tungstates ceramics stems from their use as thermal-shock-resistant materials. They are suitable for this application due to their low thermal expansion property. The Ta_2O_5-WO_3 system is the parent structure of most of these tantalum tungstates (Wu et al., 1987; Holcombe & Smith, 1978).

Wu et al. (1987) synthesised a number of polycrystalline tantalum tungstate ceramics using tantalum pentoxide (Ta_2O_5) and tungsten trioxide (WO_3) as the starting materials. Their interest in these materials was due to their thermal-shock-resistance properties. The polycrystalline tantalum tungstate powders that they synthesized were $Ta_{16}W_{18}O_{94}$, Ta_2WO_8, $Ta_{22}W_4O_{67}$ and $Ta_{30}W_2O_{81}$. They found the average linear thermal expansion coefficients to be +1.4 x 10^{-6} $^{\circ}C^{-1}$, +0.5 x 10^{-6} $^{\circ}C^{-1}$, +3.6 x 10^{-6} $^{\circ}C^{-1}$ and +4.0 x 10^{-6} $^{\circ}C^{-1}$ respectively. From these values, the tantalum tungstates were concluded as having low anisotropic thermal expansion coefficients. The *a* and *b* axes expanded while the *c* axis contracted with increasing temperature. The thermal expansion of the tantalum tungstate ceramics was measured with an alumina or fused-silica dilatometer from room temperature to 1000 $^{\circ}C$. High temperature X-ray diffraction measurements were used for the determination of the lattice thermal expansion of the ceramics.

Due to the almost zero thermal expansion (ZTE) coefficient of Ta_2WO_8, microcrack formation is not necessary for it to exhibit low thermal expansion (Wu et al., 1987).

Holcombe & Smith (1978) carried out an investigation to study a number of properties of thermally contracting tungstates. The properties that were determined by them included refined lattice constants, micro-hardness, thermal expansion, calculated thermal conductivity, density, maximum use temperatures, heat capacity, diffusivity and electrical resistivity. The purpose of investigating all these properties was to clarify the link between the structures of the compounds and their thermal contraction behaviour. The tantalum tungstates that were investigated are Ta_2WO_8, $Ta_{16}W_{18}O_{94}$ and $Ta_{22}W_4O_{67}$. In their study, the tantalum tungstates were synthesised using appropriate amounts of H_2WO_4 and Ta_2O_5 and then subjected to atmospheric-sintering (AS). $TaWO_8$ was studied when subjected to two other types of heat treatment. The two heat treatments used were reactive hot-pressed (RHP) and hot-pressed (HP). Their average coefficients of thermal expansion ranged from -5.1 x 10^{-6} $^{\circ}C^{-1}$ to +0.6 x 10^{-6} $^{\circ}C^{-1}$ between room temperature and 1000 $^{\circ}$C. The conclusion of the study they carried out showed that the low thermal expansion and negative thermal expansion was independent of the density of the materials. It was stated that due to these properties, it was possible to adapt expansion by forming various mixtures for specific applications (Holcombe & Smith, 1978).

Chu et al. (1986b) studied the thermal expansion of a tantalum tungstate below room temperature within the -123 – 27 $^{\circ}$C range. The particular tantalum tungstate that was studied was $Ta_{16}W_{18}O_{94}$. The synthetic process used to make this product involved using a 1:2.25 ratio of Ta_2O_5 and WO_3 powders respectively. The powders were mixed mechanically, cold pressed and calcined to give a precursor product. When the

coefficient of thermal expansion (CTE) was determined, the precursor was prepared in two different ways. The one set of calcined discs was hot-pressed while the other set of calcined disks was sintered. These two treatments used to study the thermal expansion gave different results. The average CTEs were determined to be -1.52 x 10^{-6} $^{\circ}C^{-1}$ and -1.0 x 10^{-6} $^{\circ}C^{-1}$ respectively. A distinct difference in the products was the porosity. The porosity of the hot pressed calcined disk was 11%, just under one third of the porosity of 39% for the sintered calcined disk. Another difference was the hysteresis loop that was observed in the sintered but not in the hot-pressed calcined disk in the desired temperature range (Chu et al., 1986b). Holcombe & Smith (1978) stated that the hysteresis observed could result from grain reorientation and cyclic deformation. However, Chu et al. (1986b) suggested the reason for the hysteresis they observed in the sintered product they studied was opening and closing of interconnected pores and microcracking. The study of this tantalum tungstate was for the purpose of possibly using it in various space applications including space mirrors and telescopes. In order to reproduce the CTE within the -93 – 27 $^{\circ}C$ range, the material must be dense and the temperature ranges small (Chu et al., 1986b).

Holcombe (1980) compiled a list of low expansion oxides and listed them from the very low to the intermediate thermal expansion compounds. Dilatometry was used to determine the thermal expansion and a fused-silica dilatometer was used. In the list of compounds, two tantalum tungstates were included. The $Ta_{16}W_{18}O_{94}$ was listed as having the lowest CTE of all the low expansion oxides that were studied. Its CTE was reported as -5.1 x 10^{-6} $^{\circ}C^{-1}$ and had a porosity of 31%. It belongs to the tetragonal

crystal system. The $Ta_{22}W_4O_{67}$ was listed as also having a very low CTE. Its CTE was reported as 0.6 x 10^{-6} $^{\circ}C^{-1}$ and its porosity was 40% but it belongs to the orthorhombic crystal system. The synthesis of these tantalum tungstates and all the other low expansion oxides studied involved a co-hydrolysis of the appropriate starting compounds which produced coprecipitated products. These products were then calcined, pressed and sintered (Holcombe, 1980).

Chu et al. (1986a) carried out another study in which they intended to synthesise a metal matrix composite that would be isotropic with high conductivity and a low CTE. This composite would possess these characteristics in the narrow range of -123 – 27 $^{\circ}C$.

The various observations from the different groups showing the CTEs and porosities, within particular temperature ranges, for various tantalum tungstates are presented in Table 5.1.

Table 5.1: Literature review comparing properties from studies of various $Ta_xW_yO_z$.

Table shows CTE and porosity within various temperature ranges.

TaxWyOz	**CTE (˚C $^{-1}$)**	**Temperature Range (˚C)**	**Porosity (%)**	**Reference**
$Ta_{16}W_{18}O_{94}$ hot-pressed	-1.52 x 10^{-6}	-123 – 27	11	Chu et al., 1986(b)
$Ta_{16}W_{18}O_{94}$ sintered	-1.10 x 10^{-6}	-123 – 27	39	Chu et al., 1986(b)
$Ta_{22}W_4O_{67}$	+0.62 x 10^{-6}	RT – 1000	40.3	Holcombe Jr & Smith, 1978
Ta_2WO_8 (AS)	-2.00 x 10^{-5}	RT – 1000	35.5	Holcombe Jr & Smith, 1978
Ta_2WO_8 (HP)	-2.12 x 10^{-6}	RT – 930	5.0	Holcombe Jr & Smith, 1978
Ta_2WO_8 (RHP)	-3.17 x 10^{-6}	RT – 840	1.0	Holcombe Jr & Smith, 1978
$Ta_{16}W_{18}O_{94}$	-5.08 x 10^{-6}	RT – 1000	30.7	Holcombe Jr & Smith, 1978
Ta_2WO_8	+0.50 x 10^{-6}	RT – 1000	-	Wu & Yamai, 1987
$Ta_{30}W_2O_{81}$	+4.00 x 10^{-6}	RT – 1000	-	Wu & Yamai, 1987
$Ta_{16}W_{18}O_{94}$	+1.40 x 10^{-6}	RT – 1000	-	Wu & Yamai, 1987
$Ta_{22}W_4O_{67}$	+3.60 x 10^{-6}	RT – 1000	-	Wu & Yamai, 1987

5.2 Synthesis of $Ta_xW_yO_z$

2.358 g of $TaCl_5$ (white crystalline powder) was dissolved in 20 ml of absolute ethanol in a 50 ml beaker and set aside. This gave a colourless solution which effervesced and gave off heat as the $TaCl_5$ dissolved. As it dissolved it underwent an exothermic reaction. 0.836 g of H_2WO_4 (yellow powder) was placed into another 50 ml beaker with 10 ml absolute ethanol. This gave a yellow suspension. To this beaker, NH_4OH was added dropwise with stirring until the H_2WO_4 dissolved. A total amount of 6 ml of NH_4OH was added and this gave a paler yellow milky solution. The tantalum ethoxide ($TaCl_5$ + C_2H_5OH) was then added to this solution with vigorous stirring and this gave a white suspension resulting from a white product precipitating out of the mixture. White fumes were given off when the solutions were mixed. The mixture was allowed to stand in a fume cupboard for 12 hours to allow the solvent (ethanol) to evaporate.

Figure 5.1: Beaker showing the white fumes coming off as the reactant solutions were mixed by stirring vigorously.

A white precipitate was obtained and it was analysed by PXRD to determine the composition of the precipitate. The white precipitate subsequently underwent heat treatment in order to drive off (decompose) the ammonium chloride precipitate, confirmed via PXRD (Figure 5.2), and to crystallise the desired product.

5.3 Results and Discussion

The precipitation reaction carried out gave a white precipitate. PXRD analysis showed that crystalline ammonium chloride was present in the precipitate. This is shown in the diffractogram below (Figure 5.2) that shows the search match carried out in DIFFRAC EVA (Karlsruhe, 2010) to identify the precipitate. The XRD diffractogram was measured at room temperature on a Bruker D2 Phaser diffractometer.

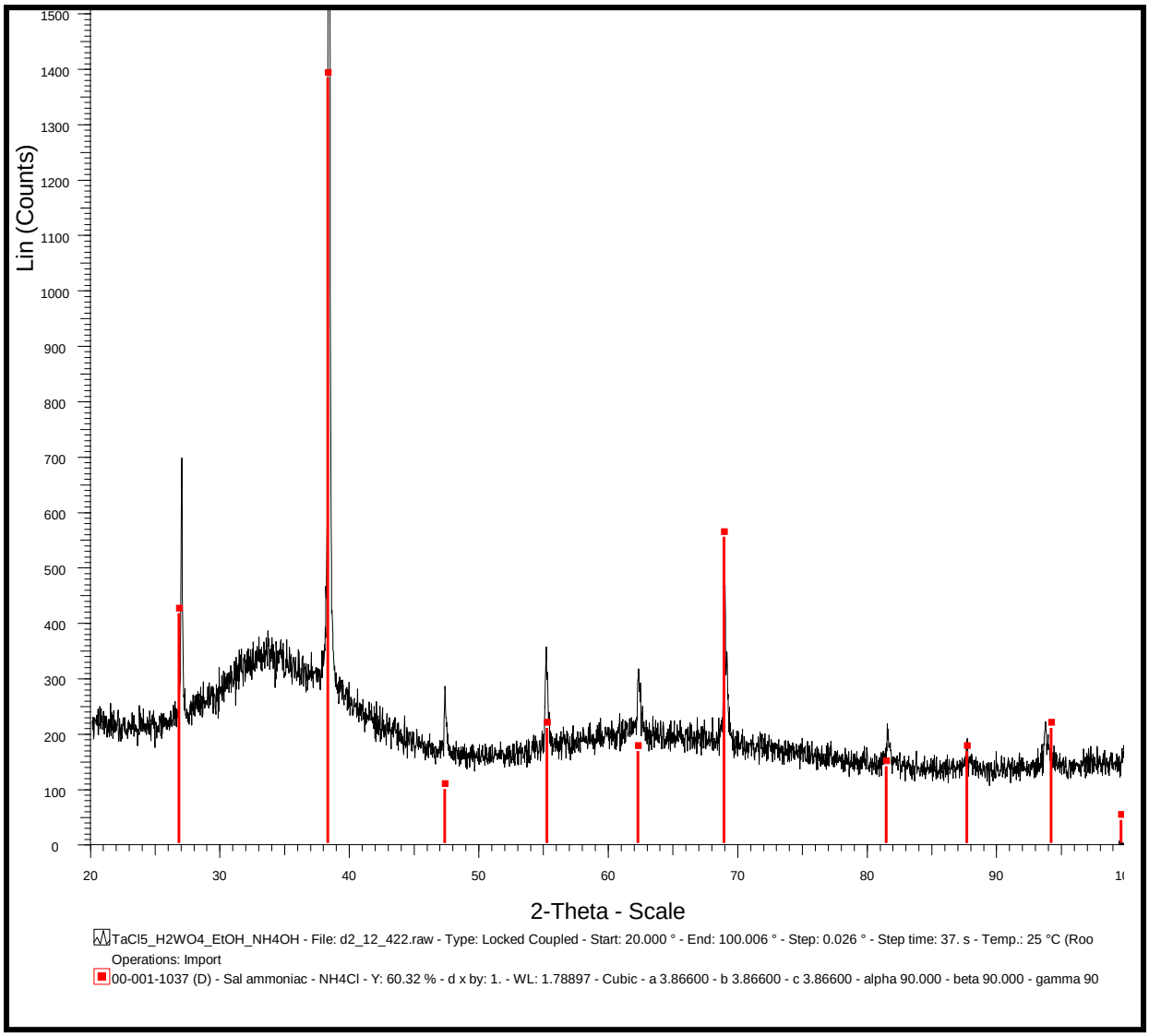

Figure 5.2: Diffraction pattern of the precipitation reaction product, showing presence of crystalline ammonium chloride and some amorphous compound.

The qualitative PXRD analysis showed our product contains salammoniac (NH_4Cl). The measured XRD pattern matched the 01-001-1037 reference pattern from the PDF-2 database (Havighurst et al., 1924).

An ex situ study involving heat treatment of the product was carried out. This analysis involved heating the product to various temperatures in a furnace, removing the product from the furnace, allowing it to stand and cool and then carrying out a PXRD analysis on it. The various temperatures at which this was done was 600 °C, 800 °C and 900 °C as shown in Figure 5.3. 900 °C was the cut-off temperature used as the D8 Advance diffractometer has a maximum operational temperature of 900 °C associated with the XRK heating chamber. This was also the temperature at which the precipitate was later discovered (section 5.4) to have fully converted to the desired product. At 600 °C, the PXRD pattern reflected the presence of amorphous matter based on the presence of the very broad peaks. At 600 °C, all the NH_4Cl has decomposed as its melting point is 338 °C (Ammonium chloride, 2012). At 800 °C the product began to convert to its crystalline form and this was observed via the sharpening of peaks. Though the peaks were sharper, they were still quite broad and therefore heat treatment was continued. At 900°C, the product had fully converted to the final desired crystalline product. XRD traces recorded as part of the ex-situ study as shown in Figure 5.3.

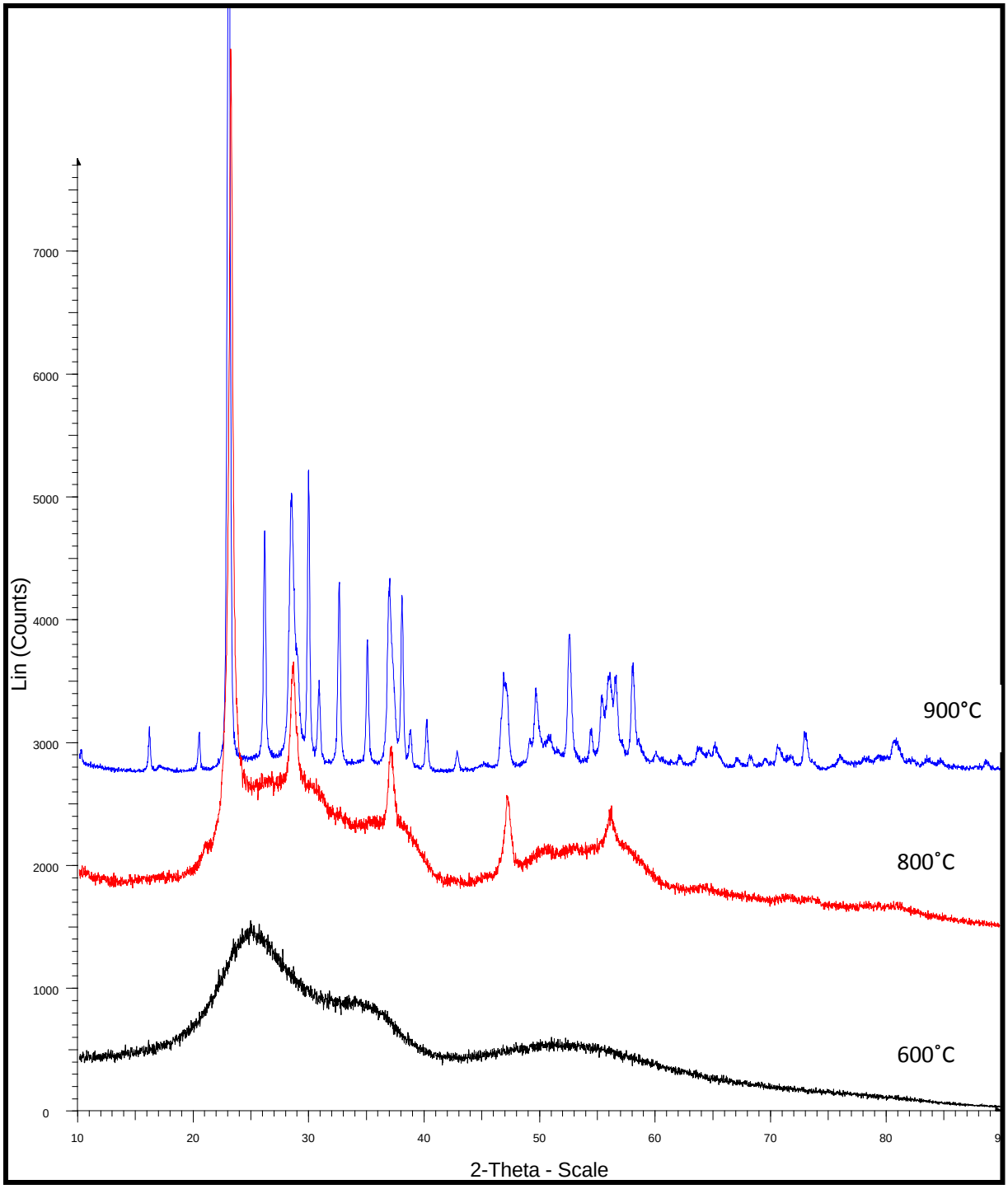

Figure 5.3: Overlay of the ex situ PXRD pattern of the ammonium-chloride containing product analysed at the various temperatures as labelled

The search match of the pattern at 900 ˚C was carried out and it was found that there were two phases of tantalum tungstates that are present in the final product. This is shown in Figure 5.4. The two phases of tantalum tungstates are $Ta_{14.6}W_{1.2}O_{40.6}$ and $Ta_{16}W_{18}O_{94}$.

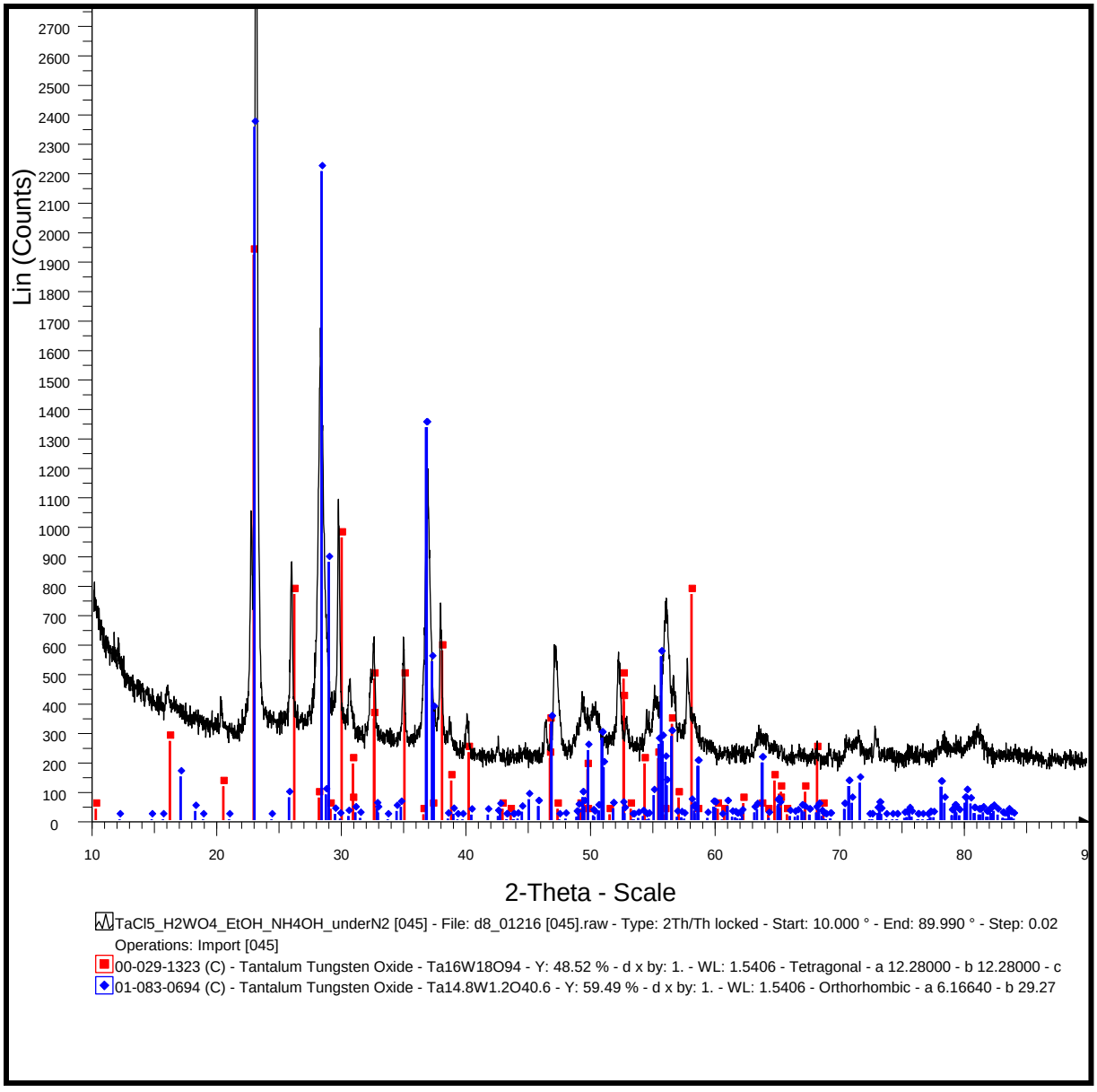

<u>Figure 5.4:</u> Search match of the 900 ˚C pattern from the ex situ analysis showing that the product contains $Ta_{16}W_{18}O_{94}$ and $Ta_{14.8}W_{1.2}O_{40.6}$.

5.4 In situ Study of $Ta_xW_yO_z$

To further investigate the mechanism via which the product formed, it was decided to perform an in situ study. This would reveal whether or not intermediate/transition state products were formed and the temperature at which the final product formed. The in situ study would also show whether the product could be obtained as a single product or a mixture of tantalum tungstates.

The in situ studies were carried out on a Bruker D8 Advance diffractometer equipped with the Anton Paar XRK 900 reaction chamber and Vantec 1-D detector. The diffractometer was also equipped with a divergence slit of 0.6 mm and a receiving slit of 10.6 mm. Ni filtered Cu Kα radiation (40 kV, 40 mA) was used.

Figures 5.5 and 5.6 show the in situ study to investigate the formation of the tantalum tungstates starting with the white ammonium chloride-containing product. The study involved passing N_2 gas over the sample as the scans were run. The scans seen in figure 5.5 and 5.6 are scans from 30 ˚C, heating up to 900 ˚C and cooling back down to 30 ˚C with 20 ˚C intervals. The instrumental parameters used as the diffraction data was collected at each different temperature are a step size of 0.021˚ on a 10 - 90˚ range and a step time of 0.5 $s.step^{-1}$. Figure 5.6 is the 3D view of the Figure 5.5.

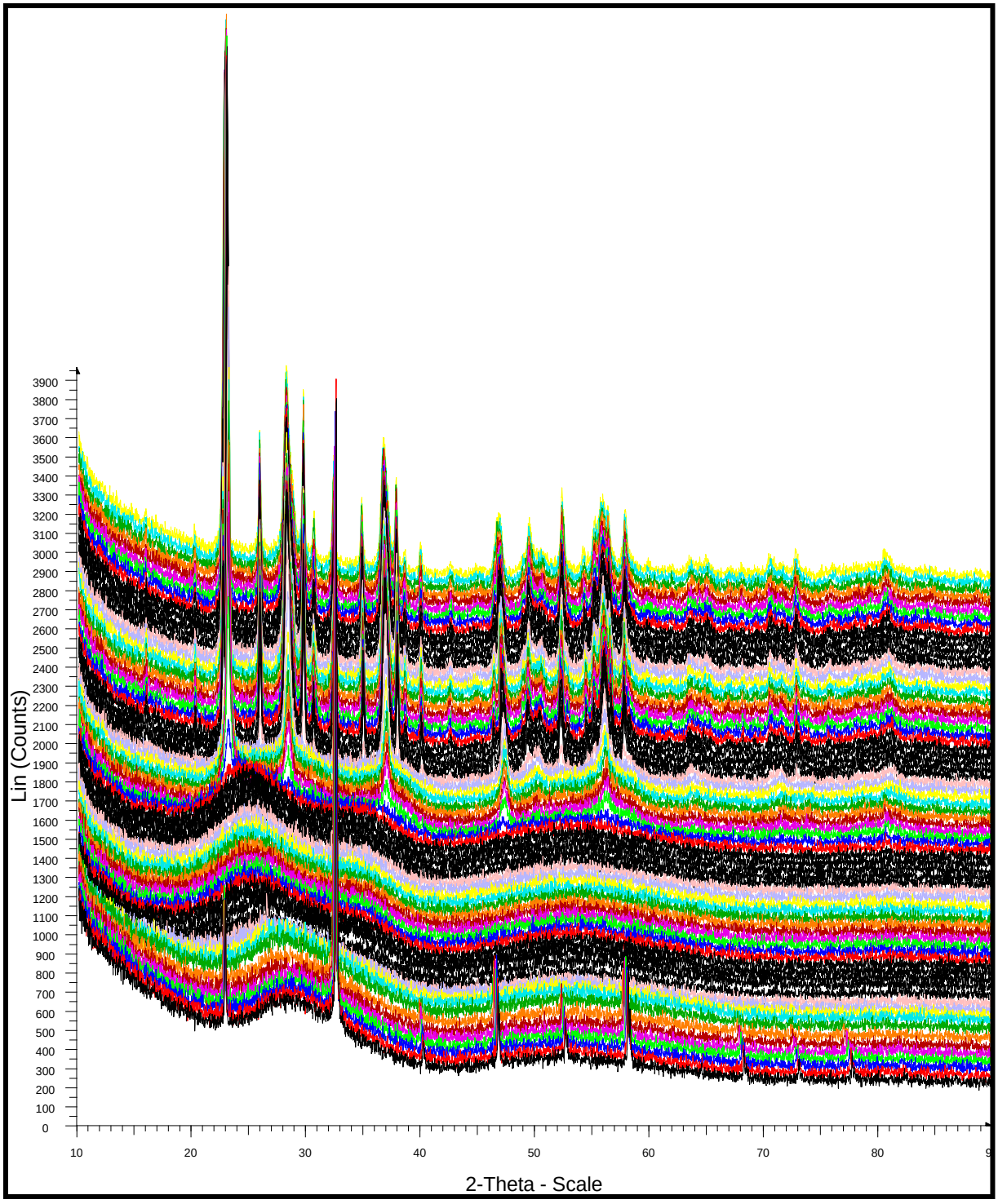

Figure 5.5: In situ VT-PXRD experiment starting with the ammonium chloride containing product undergoing its conversion to the product containing the tantalum tungstates.

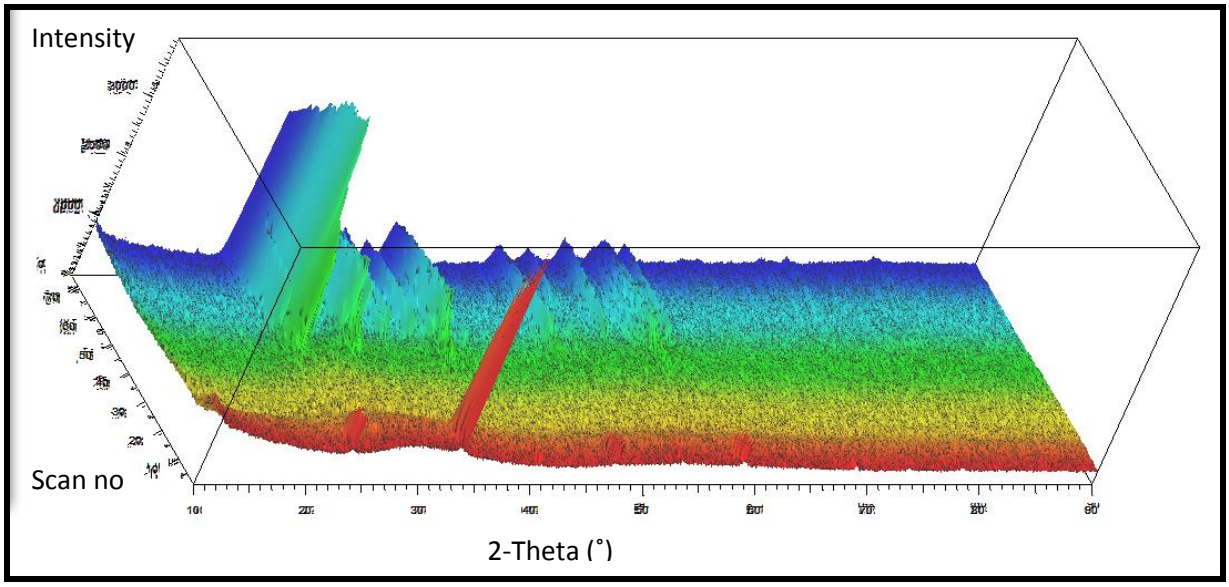

Figure 5.6: 3D view of the VT-PXRD showing the reaction from ammonium chloride containing product to the final product with the two tantalum tungstate phases. As the in situ experiment proceeded, it is shown here that the ammonium chloride was present in the red region, decomposes completely and is driven off in the yellow and green region and finally the desired product is formed in the turquoise and blue region.

The 900 ˚C ex situ heat treated sample was used in an in situ study as shown in Figure 5.7 and 5.8. During this COXA analysis, N_2 gas was passed over the sample. It involved the sample being heated from 30 ˚C to 900 ˚C using 20 ˚C increments and cooling it down back to 30 ˚C using 30 ˚C decrements. The instrumental parameters included a step size of 0.021˚ on a 10˚ - 90˚ range and a step time of 183 $s.step^{-1}$. Some mass loss was observed at the end of the in situ study.

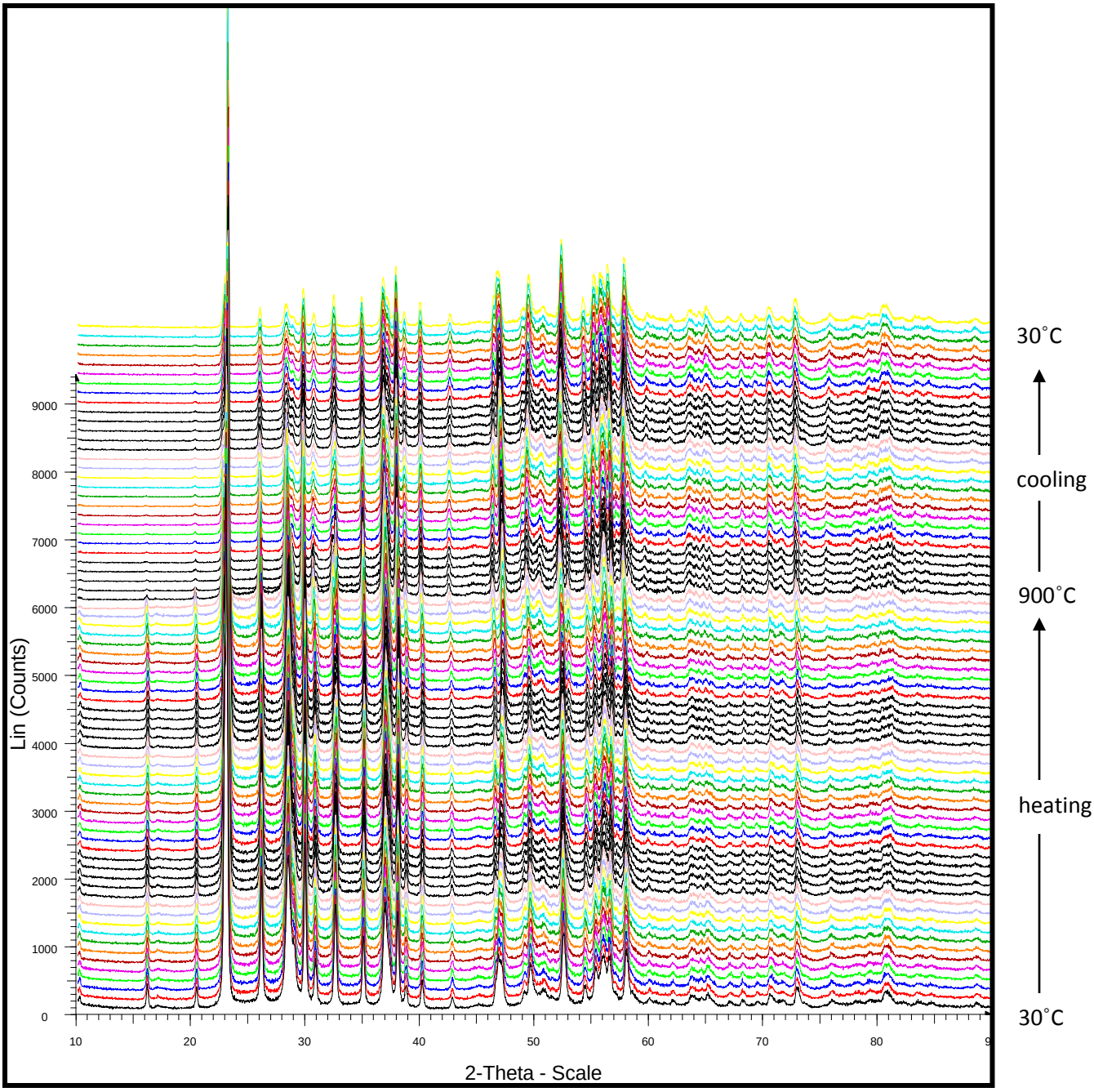

Figure 5.7: In situ VT-PXRD run of the 900 ˚C ex situ heat treated $Ta_xW_yO_z$ sample in a N_2 atmosphere heating from 30 °C to 900 °C and cooling back down to 30 °C.

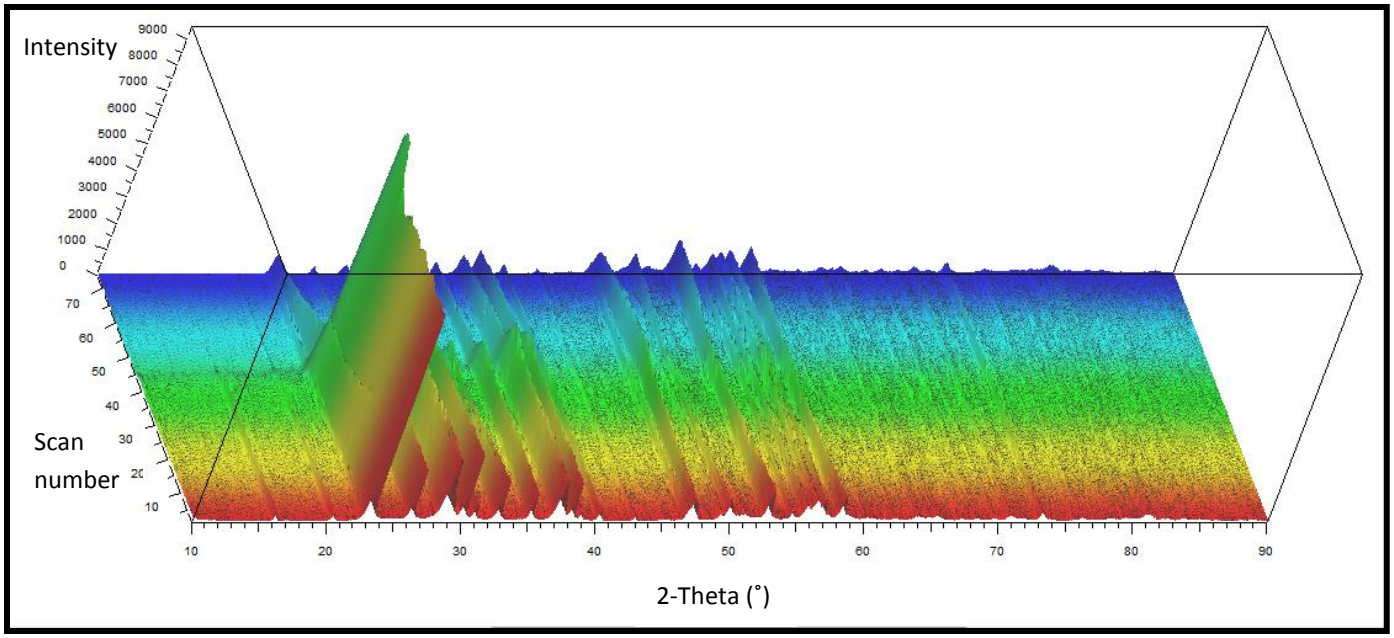

Figure 5.8: 3D view of the in situ VT-PXRD runs of the $Ta_xW_yO_z$ sample in a N_2 atmosphere (d8_12_35.raw). Observations seen in Figure 5.7 are shown clearly in this 3D view of the in situ study. The scan numbers 10, 20, 30, 40, 50, 60, 70, correspond with scans that were carried out while heating at 210 ˚C, 410 ˚C, 610 ˚C, 810 ˚C, and cooling down at 750 ˚C, 450 ˚C and 150 ˚C respectively. When heating up, the temperature was increased by 20 ˚C and when cooling was decreased by 30 ˚C.

The 30 ˚C scan [001], from the COXA analysis shown in Figure 5.7 and 5.8, was used to carry out a search match to investigate which $Ta_xW_yO_z$ phases were present. The search match showed the presence of two tantalum tungstate phases as shown in Figure 5.9.

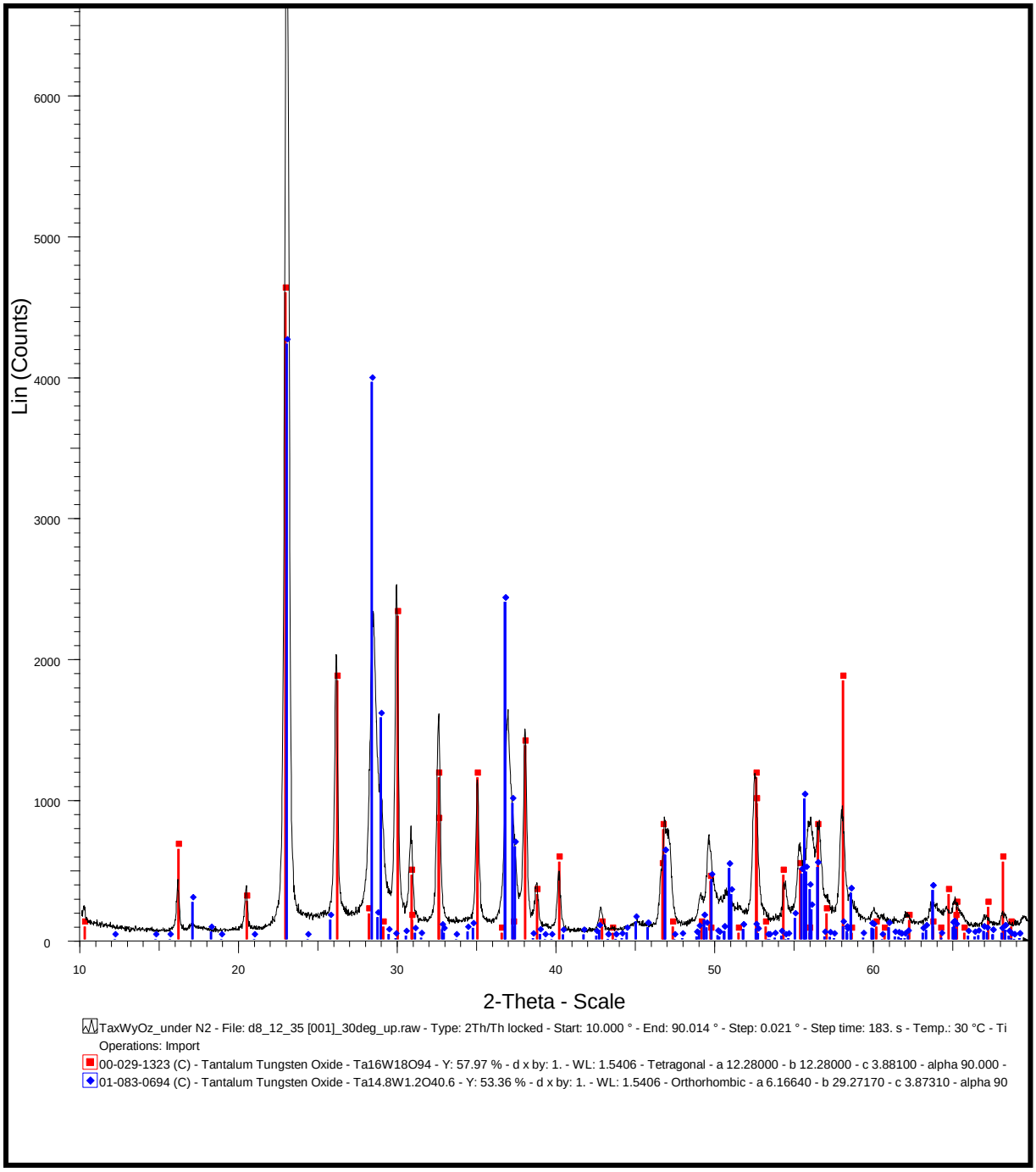

Figure 5.9: Search match of the scan carried out 30 ˚C (d8_12_35.raw) showing that the tantalum tungstates that are present are $Ta_{16}W_{18}O_{94}$ *and* $Ta_{14.8}W_{1.2}O_{40.6}$.

Comparison with the reference patterns from the PDF-2 using DIFFRAC EVA (2010) showed that the tantalum tungstates that were present in the prepared sample were $Ta_{14.6}W_{1.2}O_{40.6}$ and $Ta_{16}W_{18}O_{94}$. From Figure 5.7, it is observed that the peaks in the 10 – 20° 2θ range appear to disappear as the in situ experiment begins to take scans as it cools down. This may be the result of the crystallinity changing during cooling. All other peaks appear to be present and stable throughout the entire in-situ study.

5.5 Rietveld Refinement of $Ta_xW_yO_z$

The cif files were sought but only the one for the $Ta_{14.6}W_{1.2}O_{40.6}$ was found. A cif file is a crystallographic information file. The cif files when acquired are used as the starting model for the Rietveld refinement process.

Once the starting model has been introduced to the refinement, the various parameters are refined appropriately as to give the best refinement. The difference plot representation shown in TOPAS (Coelho, 2007) assists in showing visually the agreement of the progress of the refinement while the refinement indices give the numerical values for the agreement of the observed pattern with that of the calculated pattern.

The refinement was initiated using the structure of $Ta_{14.6}W_{1.2}O_{40.6}$ (Schmid et al., 1995) and the refinement details followed the order explained in the PXRD chapter. Structural details in the form of a CIF file were obtained from the online Inorganic Crystal Structure Database (ICSD, 2013) website. It was clear that the refinement was not complete as the other phase needed to be included in the refinement. Unfortunately the structure of

$Ta_{16}W_{18}O_{94}$ has not yet been reported and hence no structural details could be found either within the ICSD or any of the literature searched. The so-called “hkl phase” approach was thus used to complete the refinement of the product obtained.

The process of using the “hkl phase” approach for the refinement involved using the details provided in the DIFFRAC EVA PDF 2 database (2010). When using the hkl phase approach, it is important to emphasise that the refinement results seen here are understood as being the result of refining hkl values and not through the result of refining actual structural data. The information that was required for this stage of the refinement was the space group and the lattice parameter values which were entered and “fixed”. Once run, the lattice parameters were subsequently refined followed by the crystallite size L (nm). The completion of this gave the refinement model that would then be used for the sequential refinements for each of the temperatures in the in situ VT-PXRD scan. The results of this refinement were used to obtain the thermal response of the lattice parameters of each tantalum tungstate. The changes of the lattice parameters in response to different temperatures were therefore used to calculate the CTE for each. Use of the value obtained from $Ta_{16}W_{18}O_{94}$ is to be done with the full knowledge that the values calculated are for the hkl phases and not from the structure itself. This means that the resultant CTE is relative and is not the actual CTE of $Ta_{16}W_{18}O_{94}$. The difference plots from the Rietveld refinements for the 30 ˚C and the 900 ˚C patterns confirmed that the two phases that had been synthesized were $Ta_{14.6}W_{1.2}O_{40.6}$ and $Ta_{16}W_{18}O_{94}$ as shown in Figure 5.10 and 5.11.

The mass loss that was observed from some of the samples may be due to one of the phases present having a higher rate of volatilization (Holcombe and Smith, 1978).

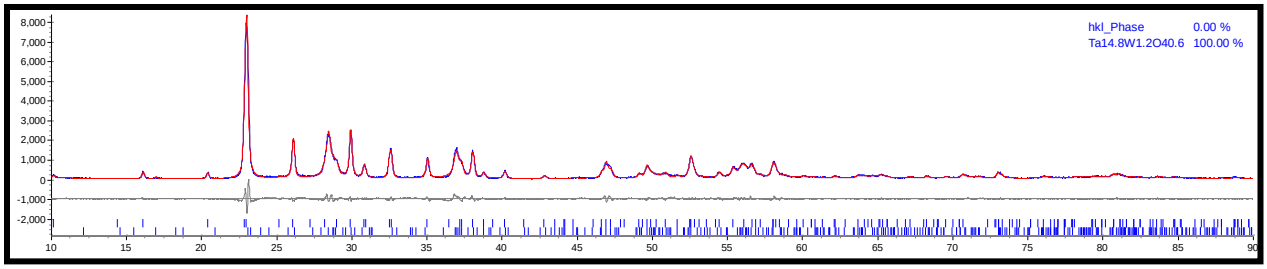

Figure 5.10: Difference plot from the Rietveld refinement of the 30 ˚C pattern for the two tungstates using the cif file for $Ta_{14.6}W_{1.2}O_{40.6}$ and the hkl values of the $Ta_{16}W_{18}O_{94}$.

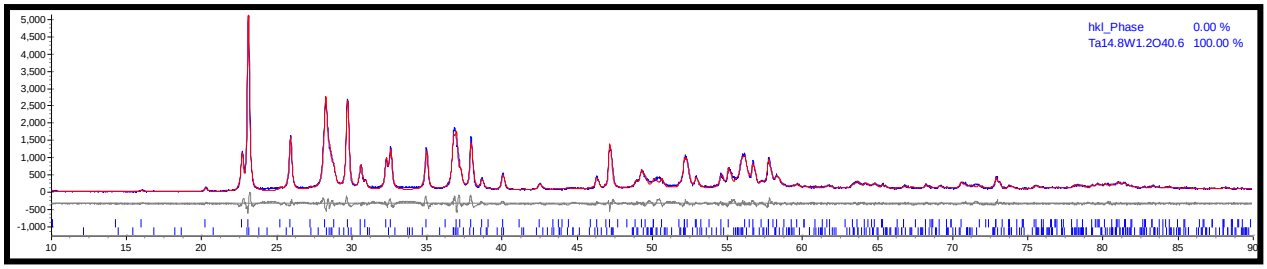

Figure 5.11: Difference plot from the Rietveld refinement of the 900 ˚C pattern for the two tungstates using the cif file for $Ta_{14.6}W_{1.2}O_{40.6}$ and the hkl values of the $Ta_{16}W_{18}O_{94}$.

For **$Ta_{14.8}W_{1.2}O_{40.6}$:**

Table 5.2: Rietveld refinement results of the $Ta_{14.8}W_{1.2}O_{40.6}$ phase from the COXA analysis of the raw data.

Temp. (˚C)	a (Å)	b (Å)	c (Å)	GOF	R_{exp}	R_{wp}
30	6.182467(5)	29.143366(4)	3.850111(4)	1.83	6.01	11.01
50	6.200893(0)	29.121266(9)	3.849065(6)	1.82	6.01	10.92
70	6.211176(2)	29.111752(1)	3.847336(7)	1.82	6.01	10.93
90	6.215314(9)	29.109827(7)	3.847837(6)	1.79	6.02	10.78
110	6.223446(9)	29.113346(4)	3.847096(2)	1.79	6.02	10.75
130	6.220866(9)	29.115940(7)	3.846938(6)	1.76	6.02	10.63
150	6.222655(7)	29.111485(3)	3.844633(2)	1.74	6.02	10.49
170	6.225394(8)	29.109693(5)	3.844412(8)	1.76	6.03	10.60
190	6.222319(5)	29.115418(3)	3.845756(4)	1.75	6.04	10.57
210	6.225040(2)	29.113423(0)	3.845128(0)	1.71	6.05	10.35

230	6.222728(8)	29.113250(6)	3.845426(0)	1.72	6.05	10.42
250	6.226508(2)	29.115974(3)	3.843656(3)	1.72	6.06	10.42
270	6.227922(1)	29.113566(2)	3.844035(7)	1.74	6.08	10.56
290	6.227968(1)	29.125003(0)	3.843634(5)	1.73	6.09	10.54
310	6.227473(4)	29.120765(0)	3.843594(0)	1.72	6.11	10.51
330	6.229807(5)	29.115623(8)	3.844175(3)	1.72	6.11	10.47
350	6.230531(7)	29.124793(6)	3.842881(5)	1.74	6.12	10.66
370	6.229662(3)	29.123984(7)	3.842617(7)	1.73	6.14	10.61
390	6.234166(5)	29.119053(2)	3.842722(2)	1.69	6.16	10.38
410	6.232127(3)	29.128415(1)	3.842977(6)	1.74	6.19	10.71
430	6.231777(2)	29.131561(8)	3.842969(6)	1.75	6.19	10.81
450	6.234049(5)	29.146450(3)	3.843293(2)	1.75	6.20	10.84
470	6.232587(5)	29.136353(3)	3.843371(6)	1.73	6.21	10.76
490	6.237820(7)	29.136659(5)	3.842252(0)	1.72	6.22	10.68
510	6.239486(5)	29.130944(7)	3.841967(4)	1.71	6.24	10.67
530	6.243657(8)	29.134756(5)	3.842035(4)	1.69	6.26	10.55
550	6.240335(6)	29.135963(8)	3.843900(3)	1.72	6.27	10.78
570	6.245137(1)	29.143628(8)	3.841984(6)	1.73	6.30	10.88
590	6.224650(0)	29.135524(3)	3.842880(5)	1.67	6.31	10.57
610	6.247448(7)	29.142500(3)	3.843296(8)	1.68	6.34	10.68
630	6.247280(3)	29.134668(1)	3.843296(8)	1.71	6.36	10.91
650	6.247380(3)	29.141053(5)	3.843296(8)	1.71	6.39	10.93
670	6.247694(8)	29.143722(4)	3.843640(3)	1.69	6.40	10.84
690	6.250303(2)	29.145300(4)	3.843820(9)	1.69	6.39	10.79
710	6.251391(8)	29.158185(1)	3.845182(9)	1.71	6.40	10.95
730	6.255630(9)	29.154114(0)	3.843999(0)	1.73	6.37	11.04
750	6.256940(4)	29.148847(8)	3.844778(6)	1.74	6.34	11.00
770	6.258088(7)	29.153950(0)	3.845696(1)	1.74	6.28	10.95
790	6.259572(1)	29.153003(2)	3.846407(6)	1.77	6.21	10.99
810	6.262566(4)	29.148999(6)	3.847551(8)	1.79	6.12	10.98
830	6.264411(7)	29.161380(7)	3.846150(5)	1.78	6.01	10.68
850	6.264357(8)	29.164846(7)	3.849513(7)	1.80	5.94	10.69
870	6.258025(6)	29.179055(2)	3.856349(6)	1.80	5.92	10.65
890	6.258269(6)	29.185523(6)	3.860476(0)	1.87	5.94	11.10
900	6.259979(6)	29.205222(7)	3.865141(4)	1.91	6.26	11.98

The thermal response of the $Ta_{14.8}W_{1.2}O_{40.6}$ that was synthesized in this study is shown graphically in figures 5.12 - 5.16:

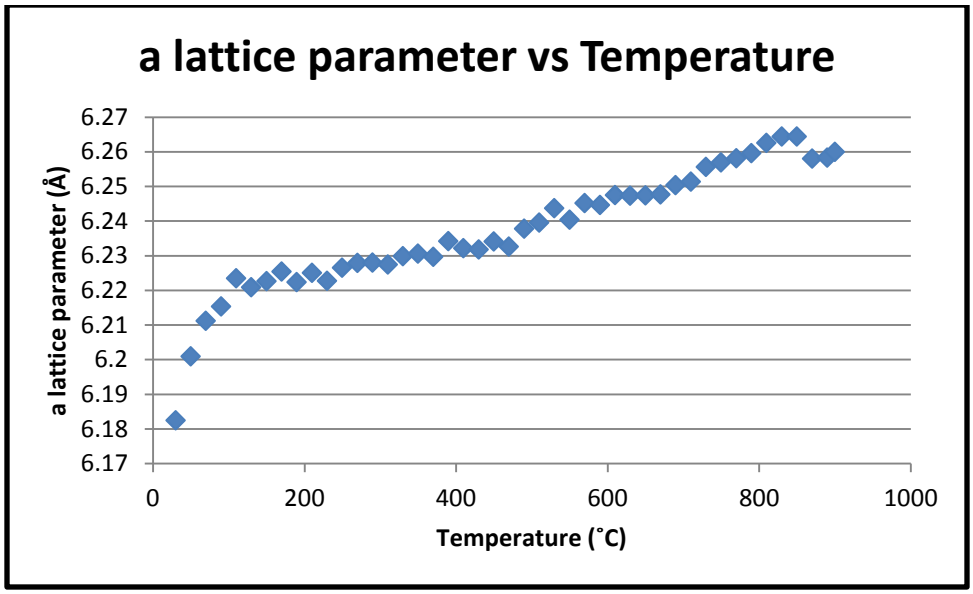

Figure 5.12: Thermal response of the a lattice parameter. The a lattice parameter increases as the temperature increases and therefore has positive thermal expansion.

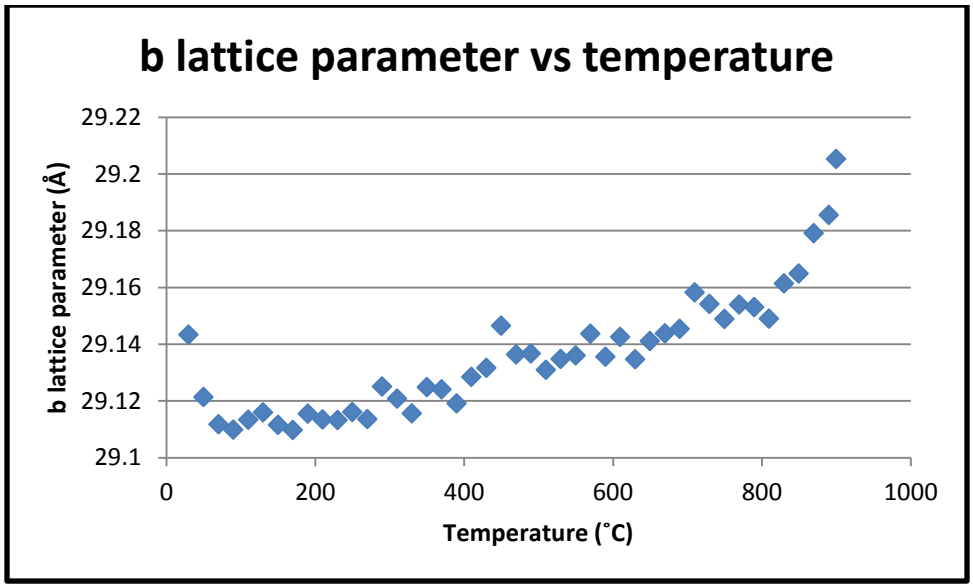

Figure 5.13: Thermal response of the b lattice parameter. The b lattice parameter decreases initially then increases as the temperature increases and therefore has an overall positive thermal expansion.

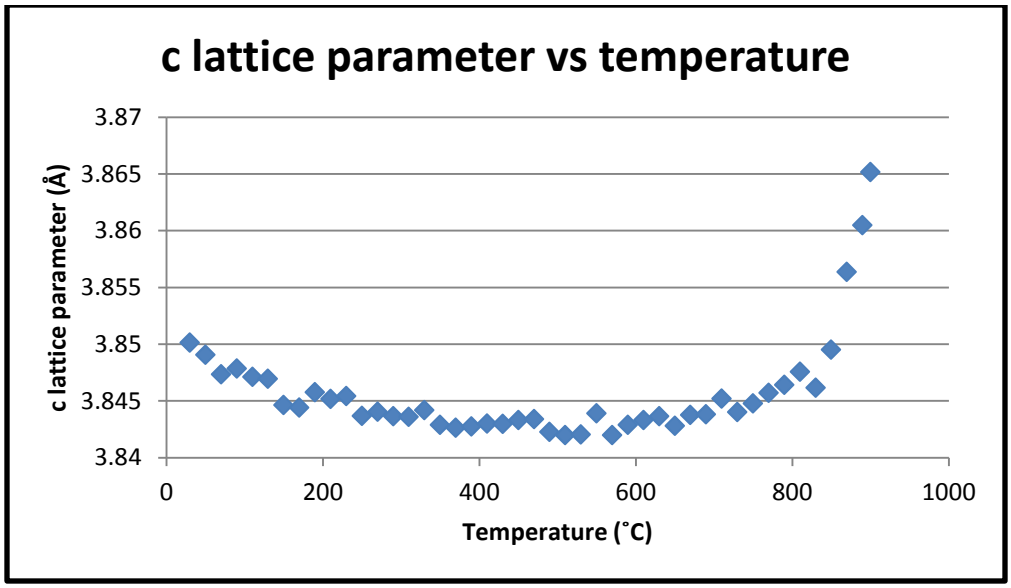

Figure 5.14: Thermal response of the c lattice parameter. The c lattice parameter decreases gradually as the temperature increases until 700 ˚C then it increases as the temperature increases.

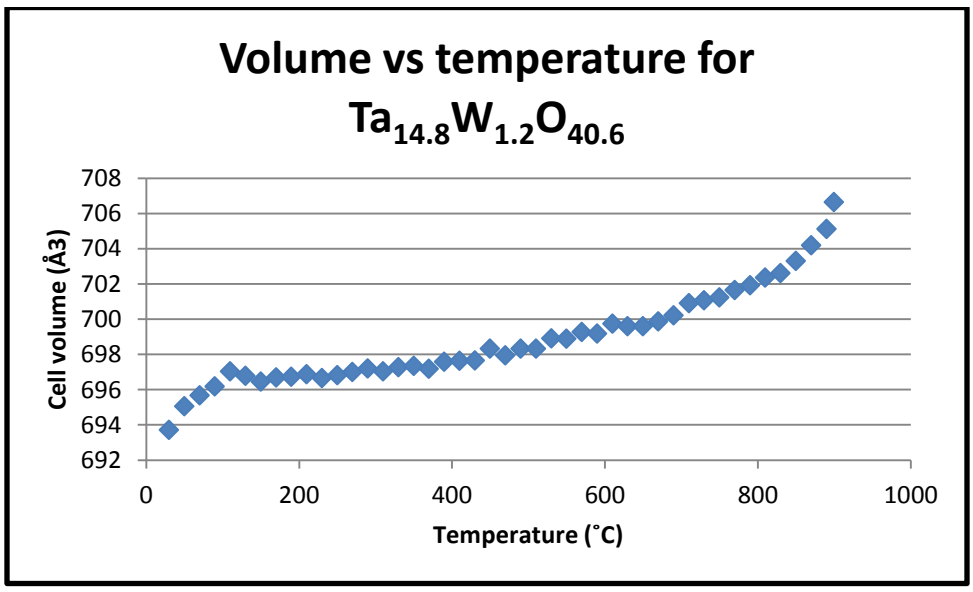

Figure 5.15: The volume of the unit cell increased as the temperature increased and this confirmed that the $Ta_{14.8}W_{1.2}O_{40.6}$ had a positive volumetric thermal expansion.

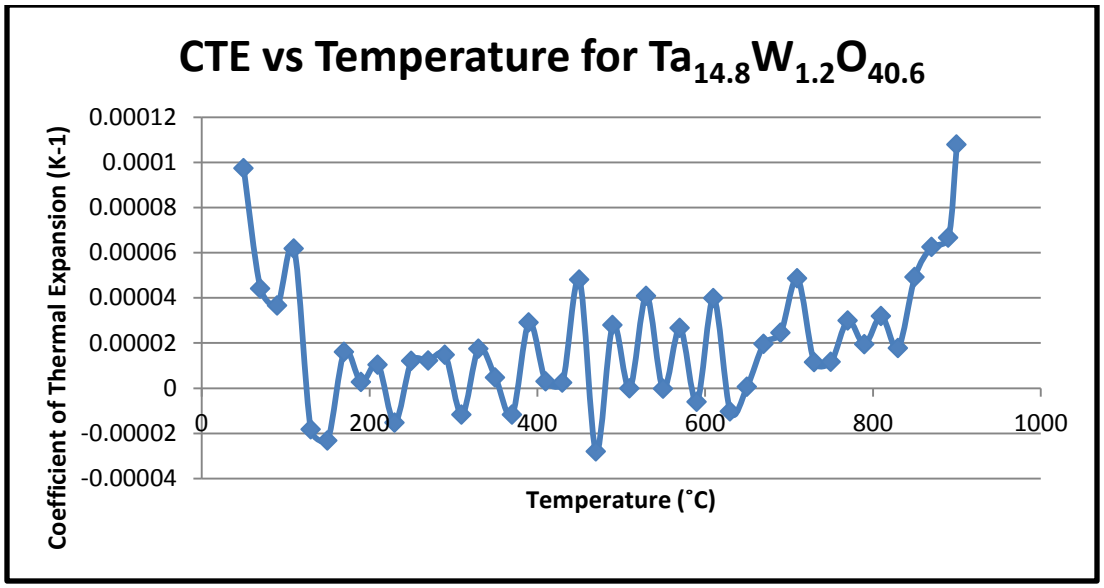

Figure 5.16: Relationship between the CTE and temperature for $Ta_{14.8}W_{1.2}O_{40.6}$

The various lattice parameters responded differently to the thermal stimuli. Table 5.2 shows the values for each lattice parameter at the various temperatures including the agreement indices for the values given. From Figure 5.12, it is clear that the a lattice parameter increased as the temperature increased. It went from 6.18 Å – 6.26 Å. Figure 5.13 shows that the b lattice parameter decreased initially then it increased. In the in situ study, it went from 29.14 Å – 29.21 Å. The c lattice parameter, shown in Figure 5.14, decreased as the temperature increased until approximately 700 ˚C. From there, it increased drastically as the temperature increased. The c lattice parameter went from 3.85 Å – 3.87 Å. When the volume of the cell was calculated, it was found that it increased as the temperature increased as shown in Figure 5.15. The volume went from 694 $Å^3$ – 707 $Å^3$.

The overall percentage change in the *a, b* and *c* lattice parameters is 1.25%, 0.21% and 0.39% respectively. From Figure 5.16, it is clear that the CTE fluctuates but the overall thermal expansion shows low positive thermal expansion

For **$Ta_{16}W_{18}O_{94}$**:

Table 5.3: Rietveld refinement results of the $Ta_{16}W_{18}O_{94}$ phase from the COXA analysis of the raw data.

Temp. (˚C)	a & b (Å)	c (Å)	Cry size (nm)	GOF	R_{exp}	R_{wp}
30	12.315210(2)	3.870478(0)	83.8	1.83	6.01	11.01
50	12.317578(9)	3.870869(4)	78.6	1.82	6.01	10.92
70	12.317905(9)	3.870299(3)	79.0	1.82	6.01	10.93
90	12.319681(9)	3.870325(1)	77.8	1.79	6.02	10.78
110	12.321810(6)	3.870374(1)	76.4	1.79	6.02	10.75
130	12.322250(6)	3.869900(1)	76.2	1.76	6.02	10.63
150	12.321450(1)	3.868237(4)	78.0	1.74	6.02	10.49
170	12.321871(5)	3.867750(1)	78.8	1.76	6.03	10.60
190	12.325437(5)	3.868061(6)	78.6	1.75	6.04	10.57
210	12.325563(2)	3.867037(7)	77.8	1.71	6.05	10.35
230	12.327200(9)	3.866265(9)	77.7	1.72	6.05	10.42
250	12.329288(0)	3.865987(7)	78.1	1.72	6.06	10.42
270	12.330502(6)	3.865368(4)	78.4	1.74	6.08	10.56
290	12.332123(6)	3.864766(5)	77.0	1.73	6.09	10.54
310	12.332649(6)	3.864008(8)	77.9	1.72	6.11	10.51
330	12.334073(2)	3.863504(0)	78.8	1.72	6.11	10.47
350	12.336217(3)	3.863146(7)	79.6	1.74	6.12	10.66
370	12.336062(8)	3.862128(6)	79.9	1.73	6.14	10.61
390	12.338685(1)	3.861987(6)	78.4	1.69	6.16	10.38
410	12.341614(1)	3.860895(9)	78.9	1.74	6.19	10.71
430	12.342018(6)	3.861016(0)	78.5	1.75	6.19	10.81
450	12.344720(7)	3.860925(3)	79.8	1.75	6.20	10.84
470	12.345233(6)	3.860067(5)	79.0	1.73	6.21	10.76
490	12.345970(8)	3.859126(6)	79.5	1.72	6.22	10.68
510	12.347275(2)	3.858863(9)	79.9	1.71	6.24	10.67
530	12.349959(1)	3.858608(7)	80.8	1.69	6.26	10.55
550	12.352338(7)	3.856817(4)	77.9	1.72	6.27	10.78
570	12.353604(1)	3.856457(7)	78.8	1.73	6.30	10.88
590	12.354694(0)	3.855950(6)	79.9	1.67	6.31	10.57

610	12.357176(9)	3.856259(6)	78.6	1.68	6.34	10.68
630	12.357620(9)	3.855453(8)	79.2	1.71	6.36	10.91
650	12.359200(9)	3.855083(6)	80.6	1.71	6.39	10.93
670	12.360934(3)	3.855084(2)	80.0	1.69	6.40	10.84
690	12.363015(0)	3.855181(8)	81.1	1.69	6.39	10.79
710	12.366486(3)	3.855175(6)	78.9	1.71	6.40	10.95
730	12.366942(2)	3.854739(2)	83.0	1.73	6.37	11.04
750	12.369087(0)	3.854390(8)	82.3	1.74	6.34	11.00
770	12.372993(7)	3.854167(1)	81.2	1.74	6.28	10.95
790	12.374945(1)	3.853462(4)	82.9	1.77	6.21	10.99
810	12.379000(5)	3.852971(5)	82.7	1.79	6.12	10.98
830	12.381156(5)	3.852035(7)	84.7	1.78	6.01	10.68
850	12.384919(1)	3.851151(0)	81.8	1.80	5.94	10.69
870	12.388957(6)	3.850872(0)	80.5	1.80	5.92	10.65
890	12.392553(3)	3.850832(1)	77.5	1.87	5.94	11.10
900	12.399397(1)	3.852441(7)	62.8	1.91	6.26	11.98

It is important to note that the results given in the table above and illustrated in the graphs to follow are based on the refinement using the hkl values and not on solved crystal structure values. This is due to the fact that the $Ta_{16}W_{18}O_{94}$ crystal structure has not been solved.

The thermal response of the $Ta_{16}W_{18}O_{94}$ that was synthesised in this study is shown in the graphs below.

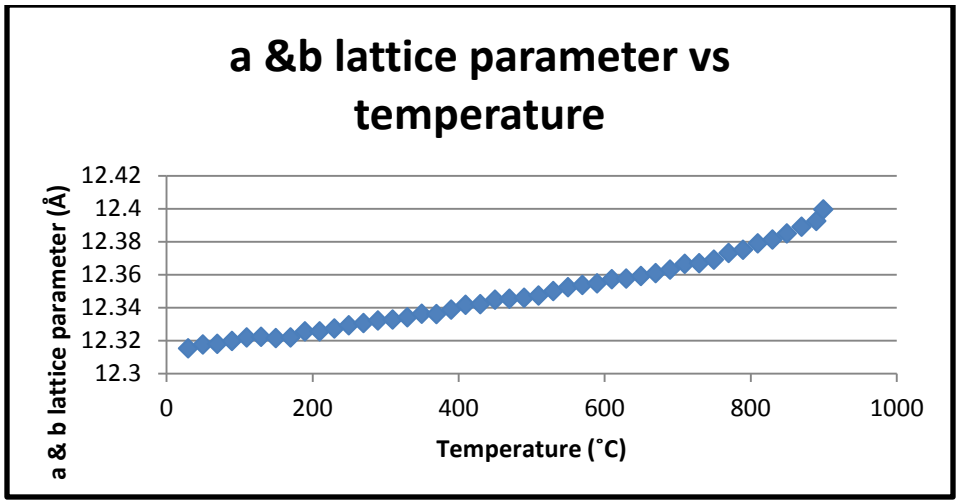

Figure 5.17: Thermal response of the a and b lattice parameters. The a and b lattice parameters increase as the temperature increases and therefore undergo positive thermal expansion.

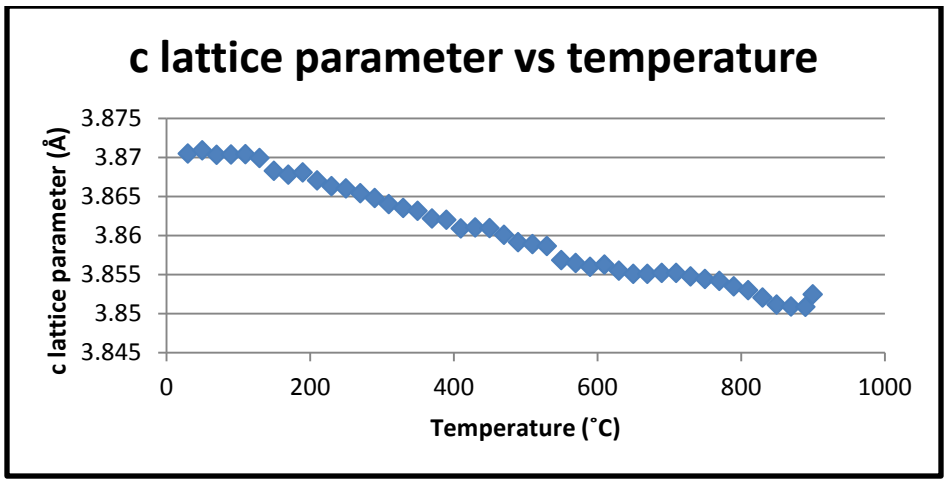

Figure 5.18: Thermal response of the c lattice parameter. The c lattice parameter decreases as the temperature increases and therefore undergoes negative thermal expansion.

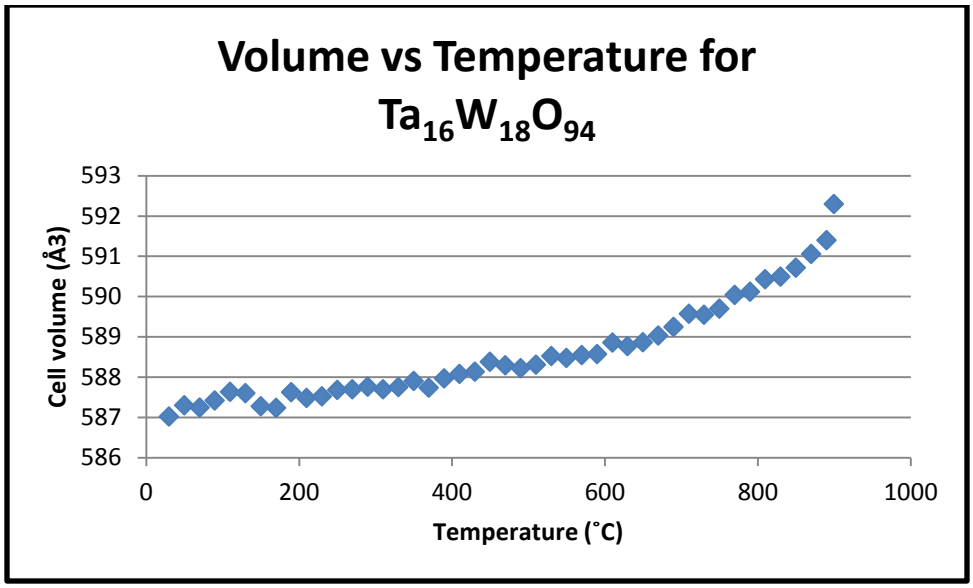

Figure 5.19: The volume of the unit cell increased as the temperature increased and this confirmed that the $Ta_{16}W_{18}O_{94}$ had a positive volumetric thermal expansion.

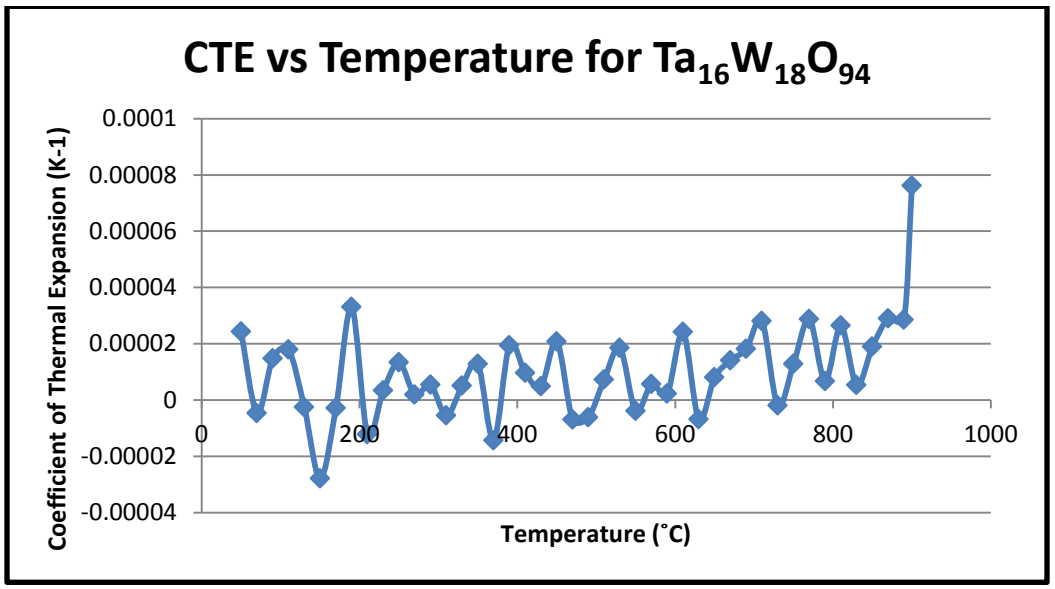

Figure 5.20: Relationship between the CTE and temperature for $Ta_{16}W_{18}O_{94}$

The various lattice parameters responded differently to the thermal stimuli. The a and b lattice parameters have the same values while the c lattice parameter is different. Table 5.3 shows the values for each lattice parameter at the various temperatures including the crystallite size and agreement indices for the values given. From Figure 5.17, it is clear that the a and b lattice parameters increased as the temperature increased. They went from 12.32 Å – 12.40 Å. The c lattice parameter, shown in Figure 5.18, decreased as the temperature increased. It went from 3.87 Å – 3.85 Å. When the volume of the cell was calculated, it was found that it increased as the temperature increased as shown in Figure 5.19. The volume went from 587 $Å^3$ – 592 $Å^3$.

The overall percentage change in the *a, b* and *c* lattice parameters is 0.68%, 0.68% and -0.47% respectively. Though the *c* lattice parameter decreases in size as the temperature increases, due to anisotropic expansion, the *a* and *b* lattice parameters increase in length. From Figure 5.20, it is clear that the CTE fluctuates. Though there is some thermal contraction, it is not sufficient to overcome the positive thermal expansion observed in the *a* and *b* lattice parameters and so low positive thermal expansion is observed (Figure 5.19).

5.6 Conclusion

Two tantalum tungstates were successfully synthesized via the precipitation reaction used and subsequent heat treatment. The ex situ study showed that at 900 ˚C the reaction precipitate had fully converted to the desired crystalline product. This desired crystalline product comprised of two phases of tantalum tungstates, $Ta_{14.6}W_{1.2}O_{40.6}$ and $Ta_{16}W_{18}O_{94}$. The in situ study of the 900 ˚C ex situ heat treated sample confirmed the presence of the two tantalum tungstate phases.

Rietveld refinement, of the two phase tantalum tungstate sample, involved use of the cif file for $Ta_{14.6}W_{1.2}O_{40.6}$ and “hkl phase” approach for $Ta_{16}W_{18}O_{94}$. $Ta_{14.6}W_{1.2}O_{40.6}$ showed low positive thermal expansion with the overall percentage change in a, b and c lattice parameters as 1.25%, 0.21% and 0.39% respectively. $Ta_{16}W_{18}O_{94}$ results are based on hkl values and not on solved crystal structure values. $Ta_{16}W_{18}O_{94}$ shows low positive thermal expansion. Though there is some thermal contraction in the c lattice parameter, it was insufficient to overcome the a and b lattice parameters increasing in length. The overall percentage change for the a, b and c lattice parameters was 0.68%, 0.68% and -0.47%.

5.7 References

Chu, C. N., Saka, N., Suh. N. P.; J. Eng. Mater. Technol.; 108, **1986a**, 270-274

Chu, C. N., Saka, N., Suh. N. P.; J. Eng. Mater. Technol.; 108, **1986b**, 275-278

Coelho, A. A.; *TOPAS* **2007**, V 4.2, Bruker AXS

DIFFRAC.EVA: *The Next Era in Phase Analysis*, Bruker AXS, Karlsruhe, **2010**

Havighurst, R.J., Mack, E., Blake, F.C.; *J. Am. Chem. Soc.* **1924**, 46, 2368-2374

Holcombe, C.E. Jr.; American Ceramic Society Bulletin **1980**, 59, 1219

Holcombe C.E. & Smith D.D.; Journal of the American Ceramic Society **1978**, 61, 163-169

http://en.wikipedia.org/wiki/Ammonium_chloride (Last accessed 29 February 2012)

ICSD, International Crystal Structure Database, Karlsruhe, http://icsd.fiz-karlsruhe.de/ (Last accessed 7 March 2013)

Schmid, S., Thompson, J.G., Rae, A.D., Butler, B.D., Withers, R.L., Acta Crystallogr., Sec. B: Structural Science **1995**, 51, 698

Wu J.Z., Yamai I. & Ota T.; Journal of Material Science **1987**, 22, 2816-2822

Chapter Six: Crystal Chemistry of $BaPbO_3$

6.1 Literature Review

$BaPbO_3$ and $SrPbO_3$ are tetravalent plumbates that have been studied extensively (Fu & Idjo, 1995; Shannon, 1971; Ropp, 2012; Korolkov et al., 2002). Interest in these plumbates is due to their electronic properties and the possible magnetic properties that they possess (Fu & Ijdo, 1995; Hester et al., 2002). $BaPbO_3$ has even been considered a host lattice for superconductors. The superconductive property was observed at 0.5 K, while at room temperature it showed metallic conductivity (Ritter et al., 1989). It is a metallic perovskite that possesses increasing electronic conductivity as the number of perovskite-like layers increase. $SrPbO_3$, on the other hand, has a distorted perovskite structure and shows poor conductivity. At low temperatures it also exhibits semiconductor-like properties (Fu, 1995).

In general perovskites are ceramic materials with a wide range of applications, due to their flexibility to accommodate almost all the elements in the periodic table as well as the wide variety of properties they possess. These materials were named perovskites after a geologist from Russia called Count Lev Aleksevich von Perovski (Feng et al., 2008). The general stoichiometry for a perovskite structure is ABX_3 where “A” and “B” are cations and “X” is an anion. A wide number of cations have led to a large number of related compounds with the perovskite structure (Johnsson & Lemmens, 2008). The charges possessed by the cations may vary but the perovskite of interest, $BaPbO_3$, possesses the same charges as of the original perovskite mineral, $CaTiO_3$. These charges mean that the A cation is divalent and tends to be bigger while the B cation is

tetravalent and smaller. “X” is usually oxygen but it can also be F^- and Cl^-. An established view is one where the lattice consists of smaller B cations that form oxygen octahedra, while the bigger A cations are12-fold coordinated by oxygen (Feng et al., 2008; Levy, 2005).

The ideal cubic perovskite would ideally be described as corner linked BO_6 octahedra with interstitial A cations. Figure 6.1 shows an ideal cubic perovskite where the A cations occupy the corners while the oxygen atoms occupy the face-centred positions and the B cation is in the centre (Levy, 2005).

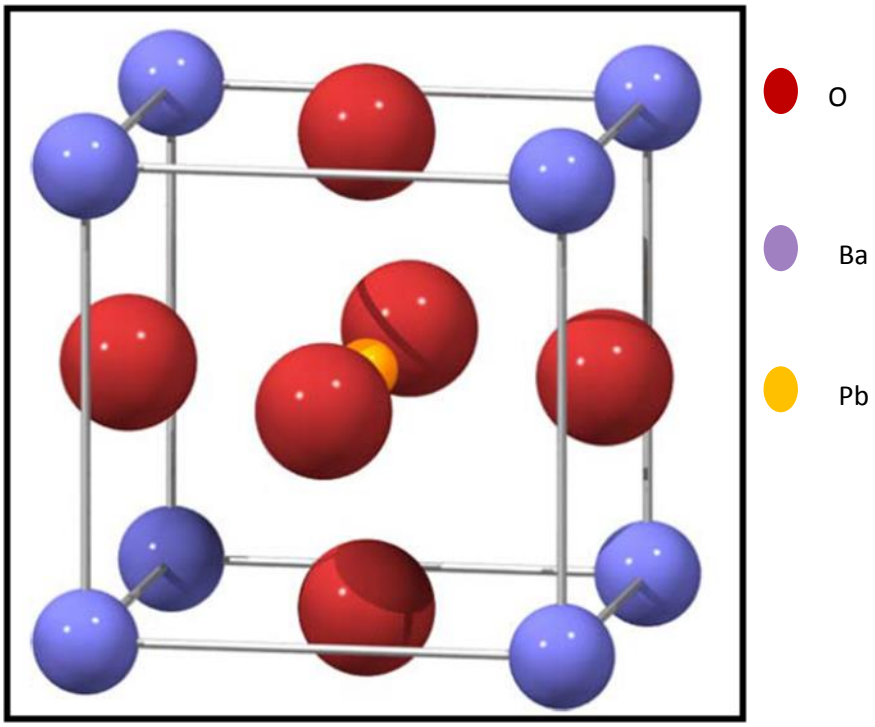

Figure 6.1: Cubic perovskite unit cell for $BaPbO_3$.

Though the original perovskite is relatively simple, the family of perovskites include a large number of variations and modifications in their structures, while still remaining related to the mineral perovskite $CaTiO_3$ (Johnsson & Lemmens, 2007). Distortions that

occur with perovskites are caused by a number of factors. The two main factors are the size effects and the Jahn-Teller effects.

Firstly, the size of the cations is important because decrease in size of the A cation can reach an extent where it is no longer in contact with the oxygen anions. This leads to the B-O-B links bending, resulting in the octahedra tilting just to restore the contact between the A cations and the oxygen anions. When these distortions occur and the octahedra tilt, this introduces a tolerance factor, t, which is used as a measure of the degree of distortion of a perovskite from cubic which is the ideal. It is also known as the Goldschmidt tolerance factor (Johnsson & Lemmens, 2008). Unity indicates that the perovskite has no distortion so the further from unity the t value, the less cubic the perovskite. The equation by which the tolerance factors are calculated is:

$$\mathbf{R_a + R_o = t \sqrt{2}\,(R_b + R_o)} \qquad (6.1)$$

where, R_a, R_b and R_o are the relative ionic radii of the A site and the B site and oxygen ion respectively. This equation can also be represented as:

$$\mathbf{t} = \frac{(\boldsymbol{R_a} + \boldsymbol{R_o})}{\sqrt{\boldsymbol{2}}(\boldsymbol{R_b} + \boldsymbol{R_o})} \qquad (6.2)$$

Decrease of the radius of the A cation, while the B cation's radius increases, leads to a decrease in the tolerance factor. This translates into the octahedra tilting to fill the space that has come about from the decrease in the size of the A cation resulting in lower symmetry orientations. This is what is observed when a perovskite distorts from being cubic to being orthorhombic (Levy, 2005; Johnsson &Lemmens, 2008).

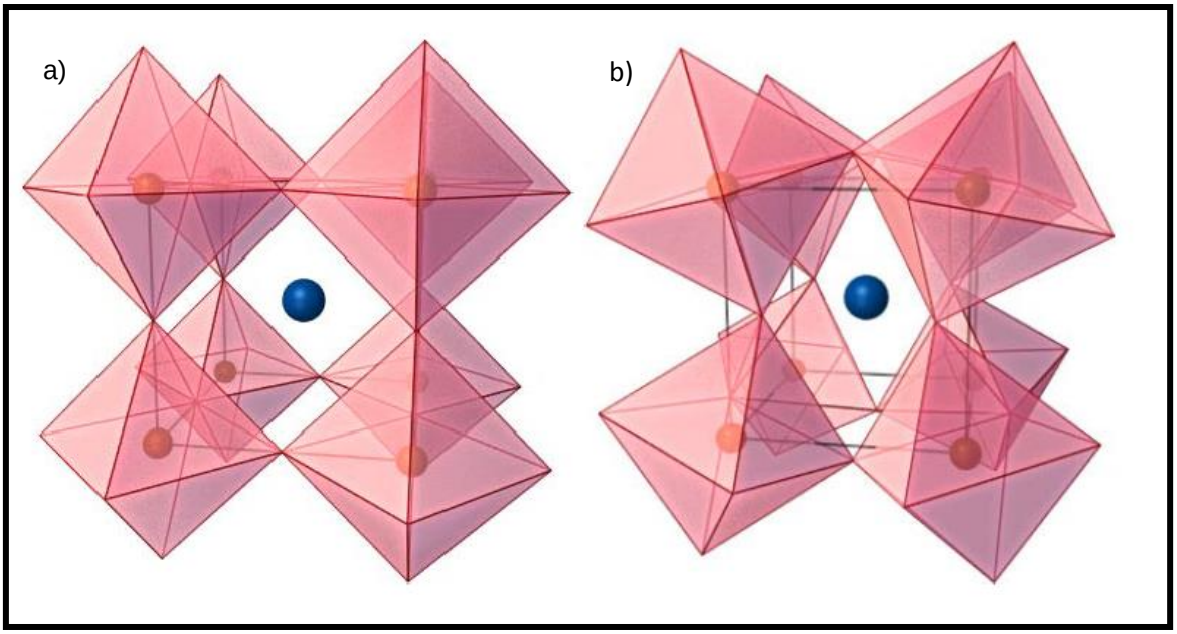

Figure 6.2: (a) Cubic perovskite. (b) Orthorhombic perovskite resulting from distortion of the cubic perovskite (Levy, 2005).

The distortions can lead to even lower symmetry arrangements than orthorhombic, e.g., hexagonal symmetry. Magnetic and electronic properties of perovskites are influenced as the symmetry is reduced due to these distortions. There are some limiting values that have been determined through various experiments that can be used as a guideline when analysing tolerance factors. 1.0 > t > 0.89 represents tolerance factors for a cubic perovskite. 0.89 > t > 0.75 represents tolerance factors for an orthorhombic perovskite. If t > 1.0, the compound will tend to stabilise the hexagonal-type perovskite structure resulting from a small B ion and a large A ion (Johnsson & Lemmens, 2008; Levy, 2005) A general conclusion is that a decrease in the size of cation A leads to a decrease in the tolerance factor as well as a lowering in the symmetry of the compound. The limitations for the use of this analysis is that 2+, 4+ perovskites will adhere to these observations better than 3+, 3+ perovskites. The other limitation is based on the fact that perovskites

are not truly ionic and so the tolerance factor is a rough estimate as it is based on calculations using ionic radii. Due to the perovskites not being truly ionic, the nature of the A and B ions affects the structure (Johnsson &Lemmens, 2008).

Secondly, the Jahn-Teller effect can be responsible for the distortion observed in perovskites if the compound has Jahn-Teller active ions at the B cation position. An example of a perovskite compound that possesses this effect is $NbMnO_3$ where the Mn^{3+} ion has to divide its $3d^4$ electrons into $3t_g$ and $1e_g$ electron. Elongation of the $[MnO_6]$ octahedron results from the odd number of electrons in the e_g orbital (Johnsson & Lemmens, 2007; 2008).

Distortion of perovskites is important because most perovskites are distorted and due to the reduced symmetries, interesting magnetic and electrical properties make perovskites industrially important.

A great many techniques have been used to study the perovskite $BaPbO_3$ including neutron powder diffraction (Fu & Idjo, 1995; Thornton & Jacobson, 1976), X-ray single crystal diffraction (Keester & White, 1970) and high-resolution X-ray powder diffraction studies (Hester et al., 2002; Ritter et al., 1989).

The suggested structure symmetries of $BaPbO_3$ were orthorhombic by Cox & Sleight (1976) and Thornton & Jacobson (1976), with the space group Imma, while Ritter et al. (1989) suggested that the structure symmetry is monoclinic, with the space group I2/m. The conclusions made by Cox & Sleight (1976) and Thornton and Jacobson (1976) were obtained at 27 ˚C and -268.8 ˚C respectively. Due to the apparent conflict in the results reported about the structure of $BaPbO_3$, Fu and Ijdo (1995) carried out a study,

using neutron powder diffraction, of the compounds $APbO_3$ (A=Ba and Sr). Their findings were that both these compounds have orthorhombic structures at room temperature (27 ˚C). They acknowledged that a monoclinic distortion could not be observed by X-ray or neutron powder diffraction. In order to investigate what the actual space group was for $BaPbO_3$; the proposed space groups were investigated by Rietveld refinements (Fu, 1995).

In another variable temperature study carried out by Hester et al. (2002), using high resolution synchrotron X-ray diffraction methods, they showed that the structure of $BaPbO_3$ undergoes a first order phase transition to form an intermediate structure at about 275 ˚C then followed by a transition at about 475 ˚C. The structure transforms as follows: orthorhombic Imma at room temperature to I4/mcm (intermediate) to cubic Pm-3m at temperatures higher than 500 ˚C. Hester et al. (2002) observed that $SrPbO_3$ remained in the orthorhombic space group Pmna from room temperature to 760 ˚C though they had found suggestions that it underwent either a first order transition to tetragonal at 450 ˚C or a first order transition to a cubic structure at 750 ˚C (Keester & White, 1970).

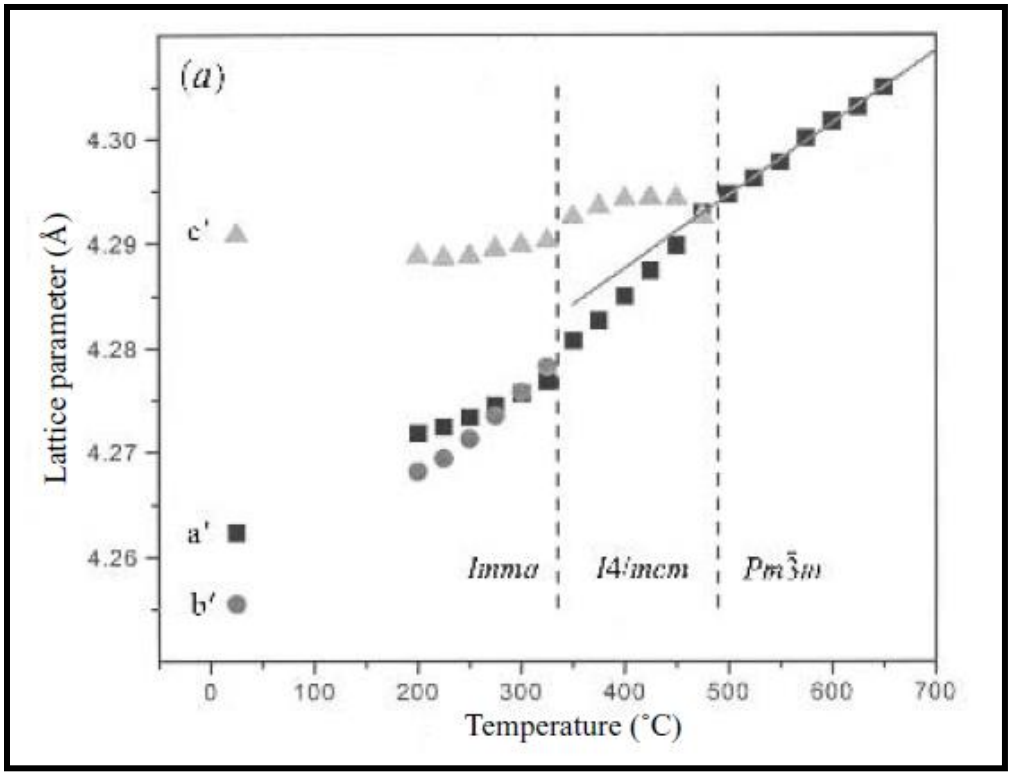

Figure 6.3: Hester et al.'s illustration of the temperature dependence of the lattice parameters (reproduced from Hester et al., 2002).

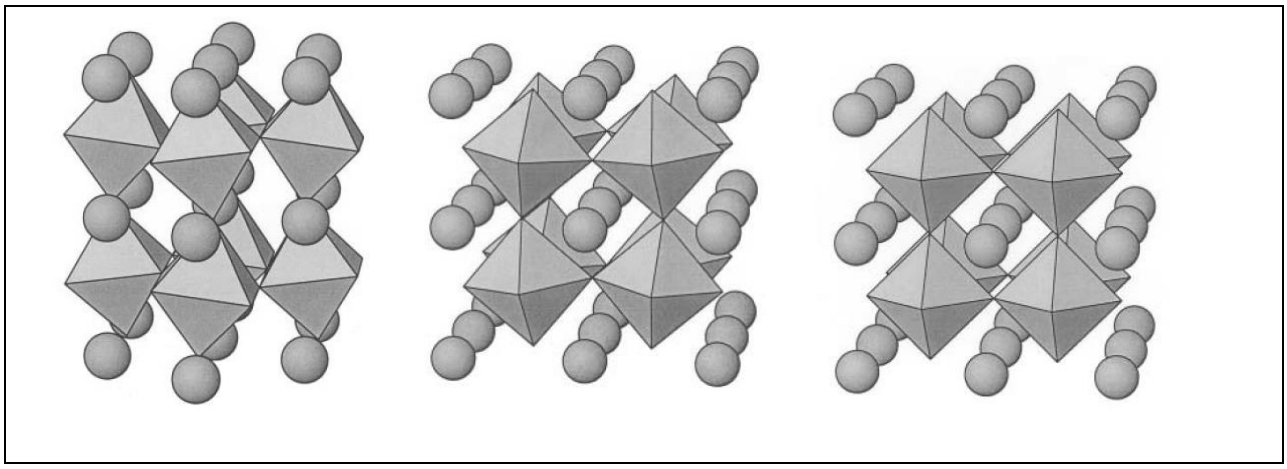

Figure 6.4: Illustration of the tilts in the polyhedra in each of the suggested phases for the BaPbO3 as suggested by Hester et al. (2002) The representations are for Imma (left), I4/mcm (middle) and Pm-3m (right). The tilting for each phase is $a^0 b^- b^-$, $a^0 a^0 c^-$ and $a^0 a^0 a^0$ respectively

using Glazer notation. This notation for describing the polyhedra tilting was developed by Glazer (1972). (Reproduced from Hester et al., 2002)

The results of the study by Fu and Ijdo (1995) concluded that both $APbO_3$ structures (A = Sr or Ba), are orthorhombic distortions of the ideal cubic-perovskite. Both structures have octahedral tilting. The difference in the extent and type of tilting observed is due to the Ba and Sr cations being different sizes. The smaller the ionic radius of a cation the larger the tilting angle of the PbO_6 octahedra (Fu & Ijdo, 1995). In a more recent study Fu et al. (2007) investigated the phase transitions for the perovskite $BaPbO_3$. A substantial amount of detail about the phase transitions was obtained through the use of high-resolution time-of-flight neutron powder diffraction. The room temperature Imma structure was found to be derived from the ideal cubic perovskite by tilting the PbO_6 octahedra around a two-fold axis and the presence of micro twins led to the observed anisotropic line broadening. At 300˚C a discontinuous phase transition to tetragonal I4/mcm resulted from the tilting of the PbO_6 octahedra about the four-fold axis of the cubic arisotype. A continuous transition was observed at 400˚C to a simple Pm-3m cubic structure.

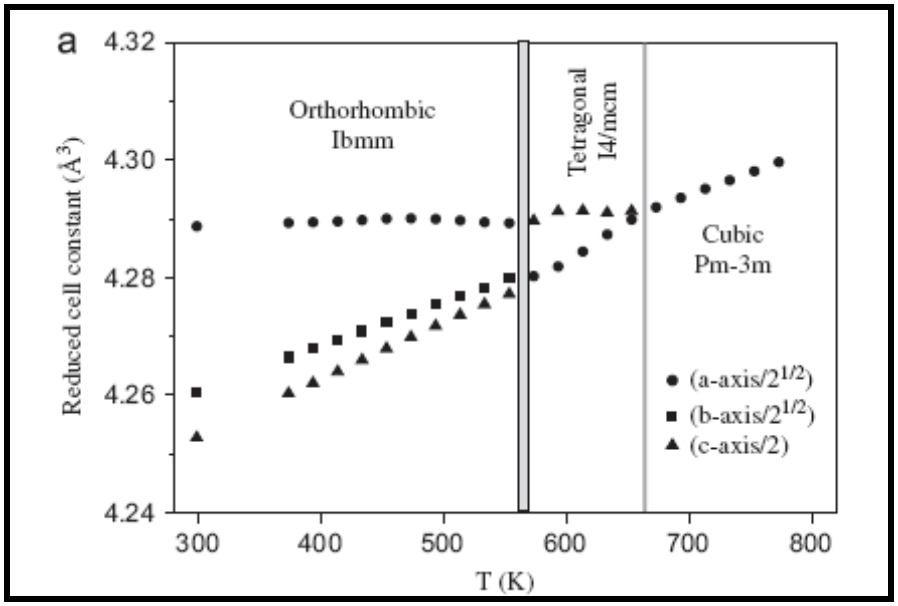

Figure 6.5: Fu et al.'s illustration of the temperature dependence of the reduced cell constants (reproduced from Fu et al., 2007).

Thornton and Jacobson (1976) suggested that the $BaPbO_3$ structure belongs to the space group Imma and not to Pbnm. They confirmed the orthorhombic nature of the distortion but found that the higher symmetry space group Imma described the structure better. The space group Pbnm is popular for many other orthorhombic perovskite systems. The perovskite structure is frequently observed with compounds with the general ABO_3 stoichiometry but a few exceptions are perfectly cubic. The A belongs to a large divalent or trivalent ion and B to a transition or B subgroup element. The space group Pm-3m is common for cubic perovskites. The deductions made by Thornton and Jacobson were the result of profile analysis of powder neutron diffraction data of $BaPbO_3$ at -268.8˚C (Thornton & Jacobson, 1976).

The phase transitions proposed by these various research groups can be illustrated by examining graphical representations of the space groups (Hahn, 2006).

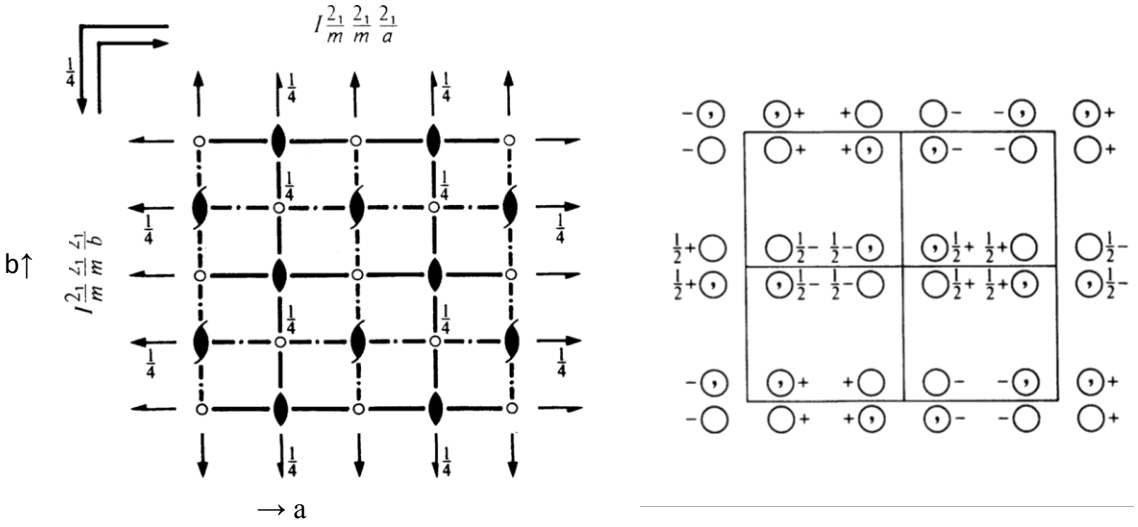

Figure 6.6: Diagram showing space group number 74 which is the Imma space group (IT 74, 2013).

This space group has four key symmetry operators or symmetry elements. These operators are centre of inversion (◦), two-fold rotation axis ( ), two-fold screw axis ( ) and mirror planes ( ). The space group is centrosymmetric and belongs to the orthorhombic crystal system.

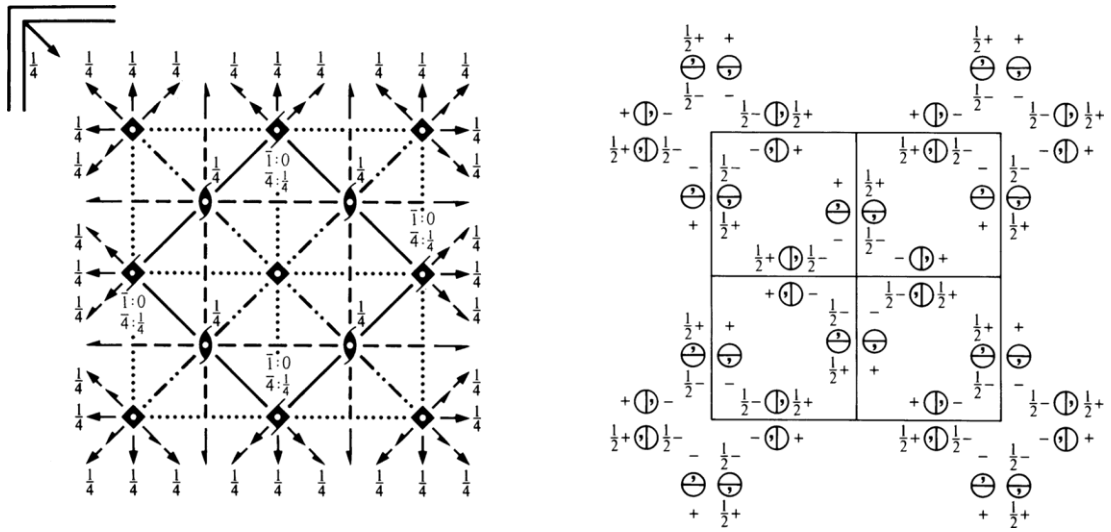

<u>Figure 6.7:</u> Illustration of space group number 140 which is space group I4/mcm (IT 140, 2013).

The space group I4/mcm has five key symmetry operators namely centres of inversion, four-fold rotation axis (), two- () and four-fold () screw axes and mirror planes. Due to the centre of inversion, the space group is centrosymmetric. This space group belongs to the tetragonal crystal system.

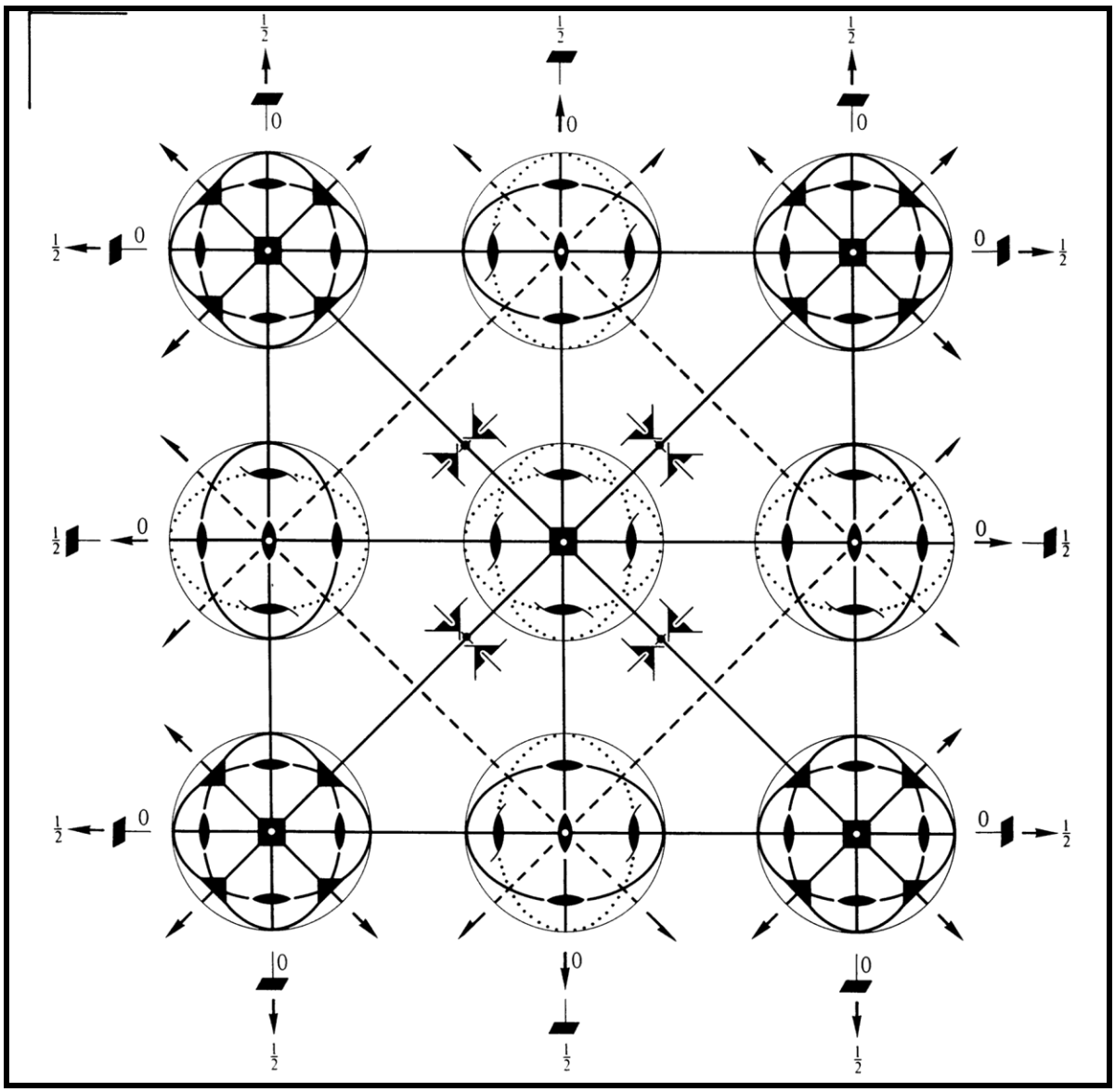

Figure 6.8: Diagram of space group Pm-3m which is space group number 221 (IT 221, 2013).

The space group Pm-3m has seven key symmetry operators. These are centres of inversion, two-, three- and four- fold rotation axes, two- () and three- () fold screw axes and mirror planes.

The results observed by the various groups concurred with the fact that the majority of the perovskites distort from the cubic symmetry at room temperature and below (Fu et al., 2007). Contradictory views on the phase transitions observed leads to one of the aims of this study which is aimed at resolving these contradictions.

Possible explanations for the tilting of the anion octahedral, distortion of the BO_6 octahedra, A and B cation ion displacements are stereochemically active lone pairs or the Jahn-Teller effect. This is just to name a few. With neutron diffraction, the tilting of the anion octahedral always results in the doubling of at least two simple cubic axes and therefore the appearance of superlattice reflections. With X-ray diffraction these would be overlooked because the reflections are usually weak due to the dominance of scattering from the heavy metal atoms. The sensitivity to weak reflections arising from oxygen-atom displacements is one of the advantages of neutron diffraction over XRD (Thornton & Jacobson, 1976).

6.2 Aims

Apparent contradictions about the temperatures at which phase changes occur for $BaPbO_3$ are reported by various groups.

- Determine phase transition temperatures.
- Determine the structural symmetry
- Resolve the contradictions in the results observed by the various research groups
- Investigate the ability of the lab XRD to be used for the above

6.3 Experimental

A serendipitously discovered bottle of $BaPbO_3$ was used as the stock sample for this research study. It was discovered during a cleanup of chemical stores during preparation for this research. A sample from the bottle was analysed using PXRD to identify if the product was indeed $BaPbO_3$ as well as its level of purity as shown in Figure 6.9.

6.4 Results and Discussion

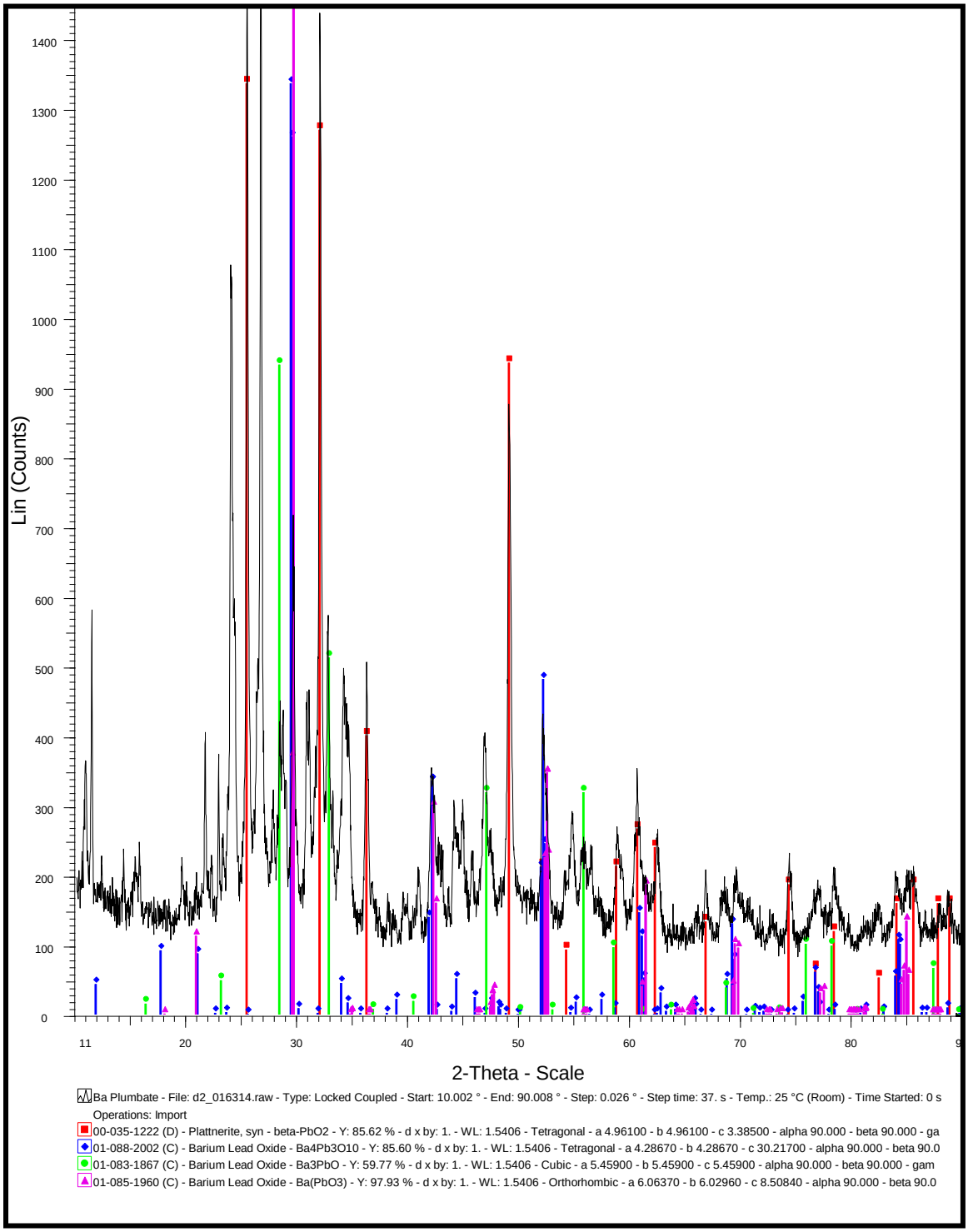

Figure 6.9: Search match of the $BaPbO_3$ sample found serendipitously prior to heat treatment to improve purity.

Figure 6.9 is a PXRD diffractogram of an untreated sample from the serendipitously found bottle suspected of containing $BaPbO_3$.It is seen that the sample had converted to a wide number of oxides. These oxides include, in varying stoichiometries, lead oxides as well as barium lead oxides. Ultimately there are some peaks that could not be matched. To investigate if the sample's purity could be improved, the sample was heat treated at 900 ˚C for 72 hours in a static air furnace and was analysed using PXRD. The effectiveness of the heat treatment is seen in Figure 6.10.

Heat treatment of the sample was good as it "cleaned" up the sample leaving a purer product. This is seen in the more resolved, less noisy Figure 6.10. This diffractogram is more resolved because the peaks are sharper and separated out clearly and less noisy because there is less background than in Figure 6.9.

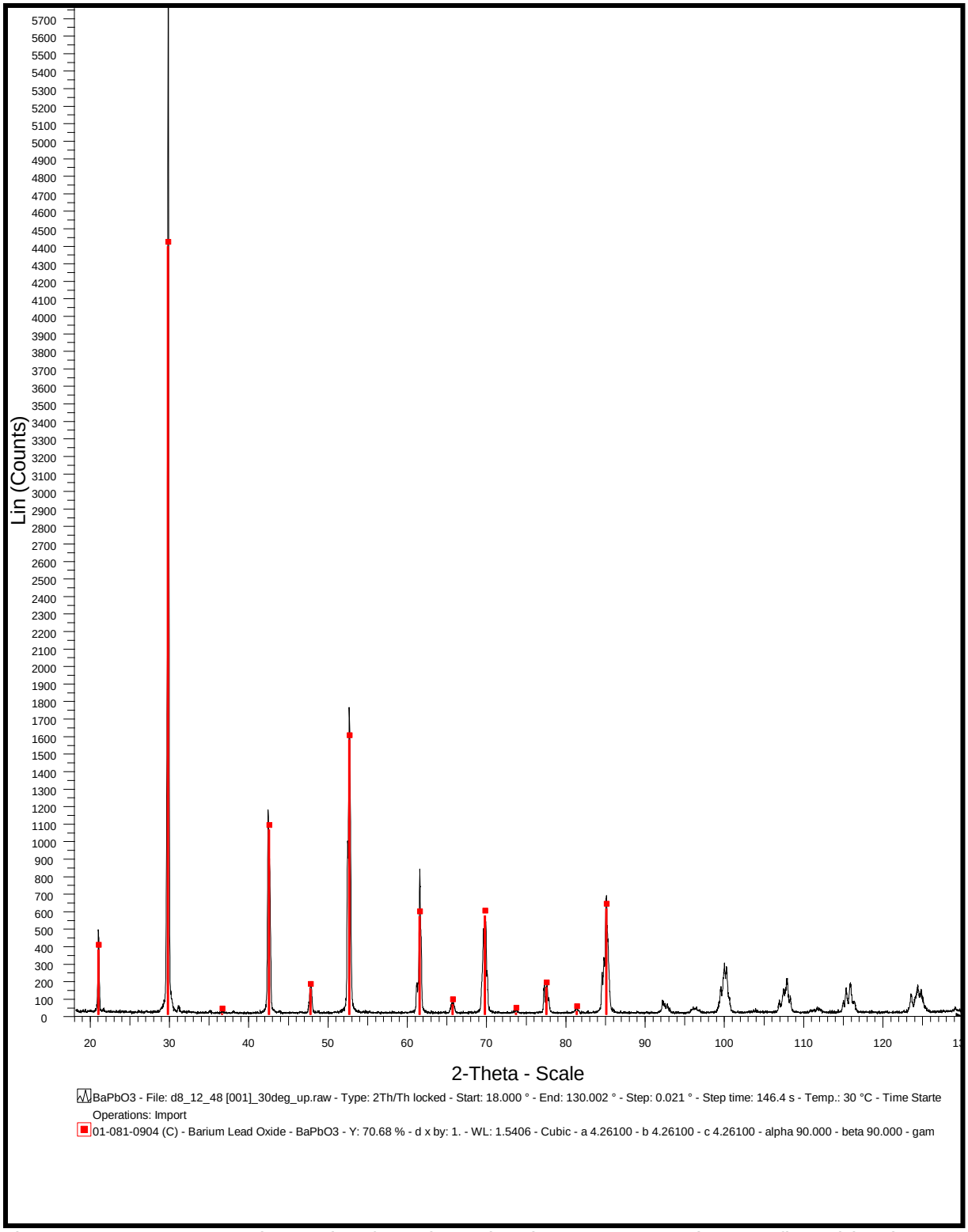

Figure 6.10: Heat treated sample of $BaPbO_3$ showing a purer product confirmed by the match showing the successful effectiveness of the heat treatment.

DIFFRAC EVA software (2010) was used to carry out the search match on the data that had been collected (Figure 6.10) and the results showed that the sample could be considered X-ray pure. All the other types of oxides had therefore either decomposed or converted to this form of barium lead oxide also known as barium plumbate. $BaPbO_3$ has the perovskite structure thus the possibility of being LTE/NTE. From the results observed, the heat treatment of the sample was deemed successful in providing a sample of $BaPbO_3$ that would be used for a VT-PXRD study to determine the phase behaviour and CTE.

Phase transitions had been observed by different groups (Fu & Ijdo, 1995; Hester et al., 2002; Fu et al., 2007). From the results observed by these groups, temperature ranges of interest were determined inorder to find the phase transition temperatures of our sample. These temperature ranges were between ~ 260 ˚C – 310 ˚C for the first phase transition and ~ 390 ˚C – 490 ˚C for the second phase transition. A COXA experiment was then carried out on the sample.

The basic details of the COXA experiment (d8_12_31.raw) involved scanning from 18˚C - 130˚ 2θ, with a step size of 0.021˚ from 30 ˚C to 550 ˚C. The experiment involved 38 scans. The 38 scans resulted from a scan being run after each 20 ˚C increment from 30˚C to 550˚C while heating and each 50˚C decrement from 550 ˚C back to 30˚C while cooling. The results of this COXA experiment are shown graphically in Figure 6.11 and in 3D view in Figure 6.12.

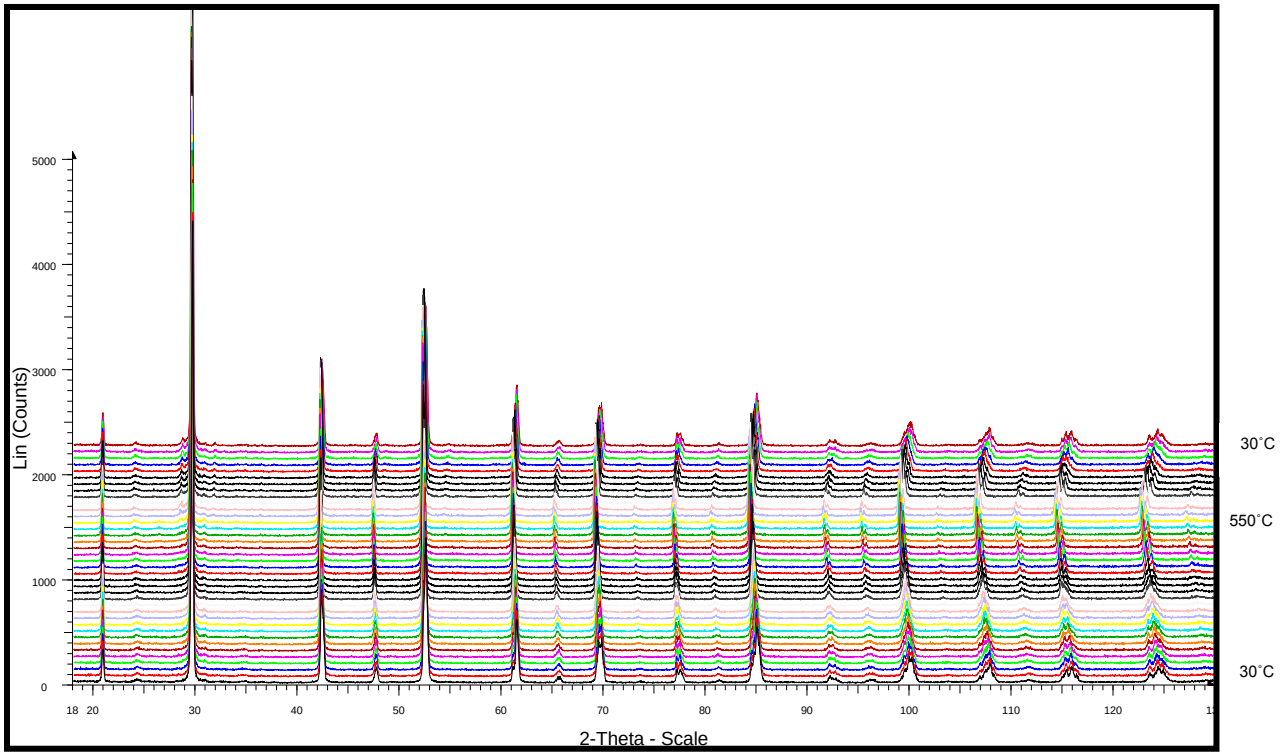

Figure 6.11: The VT-run (d8_12_31.raw) complete range of scans plotted as a function of temperature.

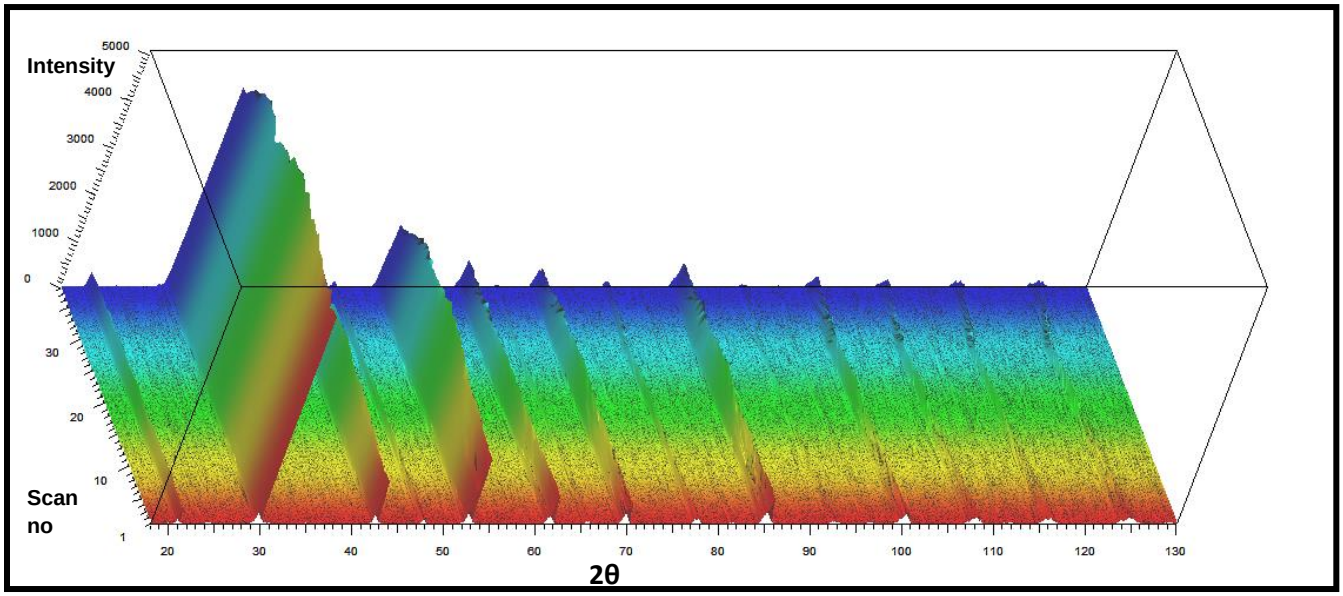

Figure 6.12: 3D view of the d8_12_31 data showing the phase transitions occurring between 30 ˚C to 550 ˚C.

Rietveld refinement analysis of the data from the COXA experiment showed that a phase transition occurred at ~ 270 ˚C and another phase transition at ~ 390 ˚C. Rietveld refinements per XRD pattern involved a total of 11 independent parameters, for the data from 30 ˚C to 270 ˚C with an additional parameter being included in the refinement from 270 ˚C to 550 ˚C. The 15 parameters were: a 2^{nd} order Chebychev background polynomial, three lattice parameters, one histogram scale factor, crystallite size, a single fundamental peak shape parameter, 8^{th} order preferred orientation spherical harmonics parameter, a zero set point correction and a description for absorption correction. The zero set point correction is also known as the sample displacement parameter. The additional parameter that was refined in the higher temperature data is the thermal parameter B_{eq}. Being a thermal parameter, its importance and effect is more of a factor at higher temperatures which is why, it was introduced in the refinement from 270 ˚C to 550 ˚C.

The positions of the atoms are reported using the Wyckoff positions for the site occupied and these give the ideal occupation of sites by the atoms.

Upon heating, before $BaPbO_3$ undergoes the phase transitions, it has an orthorhombic Imma space group. The ideal positions are, Pb is in position 4a, 0, 0, 0; Ba atoms are in the 4e, 0, ¼, z; the O1 atoms are in the 4e, 0, ¼, z and the O2 atoms are in the 8g, ¼, y, ¼. The Wyckoff position of Ba atoms is the same as that of the O1 atoms. This means that these atoms have the same symmetry position but not the same physical position.

Once $BaPbO_3$ has undergone its first phase transition, at ~ 270 ˚C, it is now a tetragonal I4/mcm space group perovskite. The ideal positions are: Pb is in 4c, 0, 0, 0; Ba atoms are in the 4b, ½, 0, ¼; the O1 atoms are in the 4a, 0, 0, ¼ and the O2 atoms are in the 8h, x, y, 0. The Ba, Pb and O1 atoms are in special positions.

When the $BaPbO_3$ has undergone the various phase changes, at ~270 ˚C and ~ 390 ˚C, it is now a cubic Pm-3m space group perovskite, the atoms ideally are in these positions: Pb atoms are in the 1a, 0, 0, 0; Ba is in the 1b, ½, ½, ½; and the O atoms are in the 3d ½, 0, 0; 0, ½, 0; 0, 0, ½. All these atoms are in special positions (Johnsson & Lemmens, 2007).

Rietveld refinement values suggested where the phase transitions occurred and therefore the powder patterns at these suggested temperatures were extracted. These powder patterns are shown in Figure 6.13. From Figure 6.13 it is clear that the differences are very slight and are therefore not very visible. An example of the slight differences that can be observed, in Figure 6.13, is seen with the peak at 61˚ 2θ. This peak had a shoulder peak at 30 ˚C showing that the peak is in fact a doublet but as the phase transitions took place, the peaks merged and sharpened. At 390˚C there is a single sharp peak observed at 61˚ 2θ.

Figure 6.13 showed that most of the changes could be observed in the high angle region of the powder pattern with peaks from ~ 83˚ 2θ to 113˚ 2θ. This section of the powder patterns was zoomed in and is shown in Figure 6.14. The clearest change was seen in how the peak multiplicities decreased from Imma (30 ˚C) to I4/mcm (270 ˚C) to Pm-3m (390 ˚C). An example is observed in Figure 6.14 with the 93˚ 2θ peak. This peak

is a broad multiplet in the Imma phase at 30 ˚C then it converted to a triplet in the I4/mcm phase at 270 ˚C. It converts to a doublet in the Pm-3m phase at 390 ˚C.

An experiment was set up to investigate specifically how a single high angle peak (~ 125˚ 2θ) behaved and is shown in Figure 6.15. This experiment showed clearly how there was a change observed in the shape, position and number of the peak(s). The purpose of this experiment was to pin-point where exactly the phase transition occurs. The results from this experiment agreed with those from the COXA experiment.

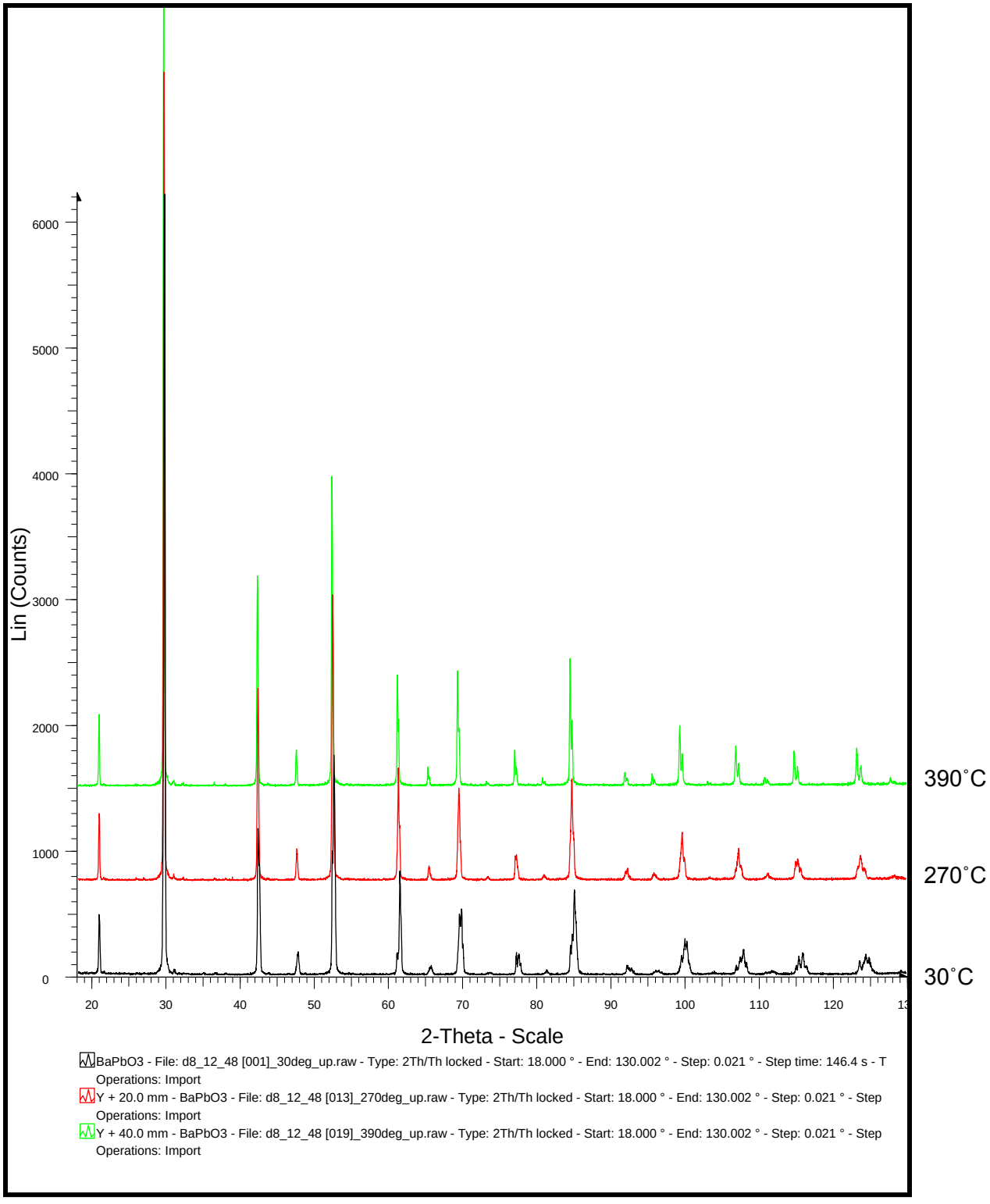

Figure 6.13: Plot of the powder patterns representative of the different phases and the temperature at which they are measured

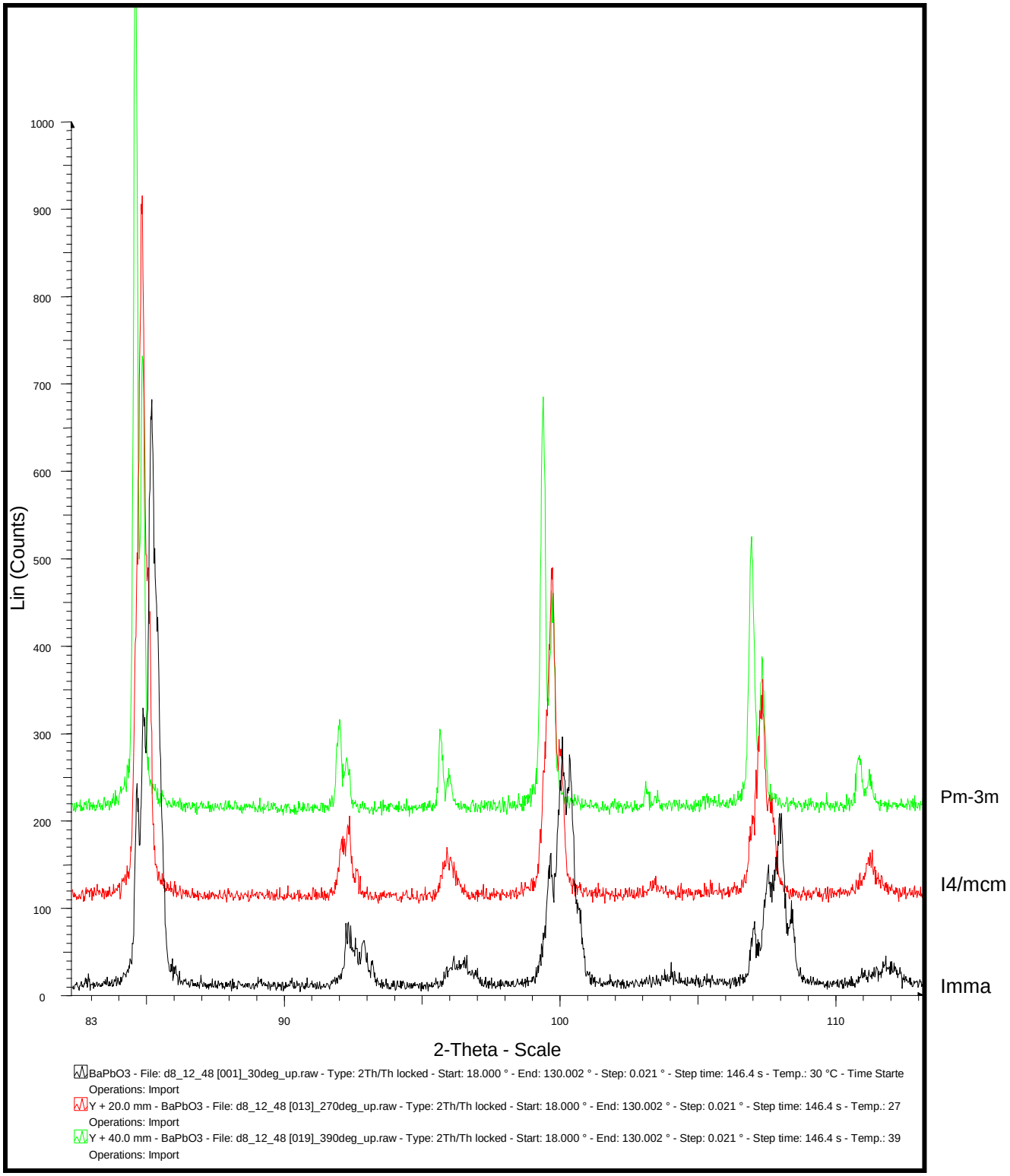

Figure 6.14: Plot of the powder patterns at the temperatures where the phase changes occur showing the zoomed in region between 83˚ - 103˚ (2-theta) to reflect the subtlety of the changes

in the powder patterns reflecting the phase changes. Imma, I4/mcm and Pm-3m patterns correlate to 30 ˚C, 270 ˚C and 390 ˚C respectively.

It is seen that symmetry is increasing as the temperature increases. The phase transitions undergone by $BaPbO_3$ are typical due to the increased motion of the atoms as they vibrate at the higher temperature and this allows them to assume a higher symmetry. The peak resolution improves as the temperature increases and the $BaPbO_3$ assumes higher symmetry. The improvement of the peak resolution is seen in the peaks sharpening as shown in Figure 6.15.

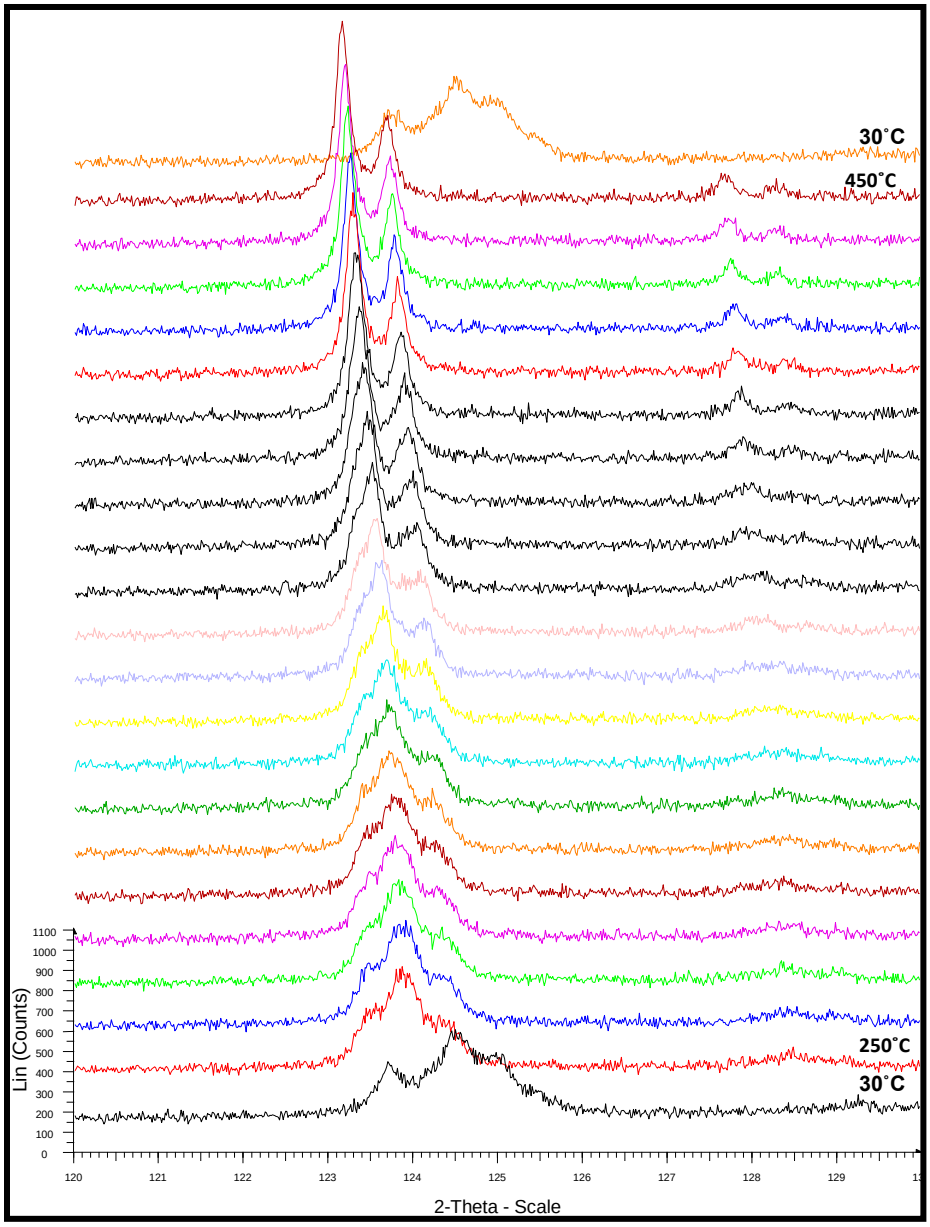

Figure 6.15: An experiment that focused on one high angle peak to show the phase changes as the experiment proceeded. Scans above show the 30 ˚C, then the 250 ˚C scans, and then each scan after that goes up by 10 ˚C till 450 ˚C then the final scan which was run at 30 ˚C.

6.5 Conclusion

From the results of the Rietveld refinement, the following conclusions could be made addressing the aim of this research. The proposed phase transitions that take place with $BaPbO_3$ go from the orthorhombic Imma to the cubic Pm-3m with an intermediate I4/mcm space group. Hester et al. (2002) had suggested that the transitions take place at 275 ˚C and 475 ˚C while Fu et al. (2007) suggested that the transitions occurred at 300 ˚C and 400 ˚C. The results from this study did not confirm any one group's results. Rather, they proved that in each group, one observation matched what was observed with the sample found. The results obtained agree with Hester's group that the first transition occurs at ~270 ˚C and with Fu's group that the second transition occurs at ~390 ˚C. These results therefore disagree with Fu's group that the first transition takes place at 300 ˚C and with Hester's group that the second transition occurs at 475 ˚C.

The conclusions that were reached and observed in this study were done at the very limit and to the full extent of what information can be obtained from the instruments that we have. Lengthy experiments were run with very small step sizes as well as longer counting times to improve the accuracy of the data that was obtained. The goal was to obtain data that would assist in detecting the phase transition temperatures as precisely as possible. This was necessary as the phase transitions crystallographically didn't give distinct powder patterns and this complicated the phase transition determination.

6.6 References

Cox, D.E., Sleight, A.W.; *Solid State Commun.* **1976**, 19, 969-973

DIFFRAC.EVA: *The Next Era in Phase Analysis*, Bruker AXS, Karlsruhe, **2010**

Feng, L. M., Jiang, L. Q., Zhu, M., Liu, H. B., Zhou, X., Li, C. H.; *J. Phys. Chem. Solids* **2008**, 69, 967-974

Fu, W.T., Ijdo, D.J.W.; *Solid State Communications* **1995**, 95, 581-585

Fu, W.T., Visser, D., Knight, K.S. & Ijdo, D.J.W.; *J. Solid State Chemistry* **2007**, 180, 1559-1565

Glazer, A.M.; Acta Cryst. **1972**, B28, 3384

Hester, J.R., Howard, C.J., Kennedy, B.J., Macquart, R.; *Aust. J. Chem.* **2002**, 55, 543-545

Hahn, Th.; *International Tables of Crystallography*, Volume A: Space-group symmetry; First online edition (**2006**) http://it.iucr.org/A/ (accessed Feb 2013)

IT74: http://it.iucr.org/Ab/ch7o1v0001/sgtable7o1o074/ (accessed Feb 2013)

IT140: http://it.iucr.org/Ab/ch7o1v0001/sgtable7o1o140/ (accessed Feb 2013)

IT221: http://it.iucr.org/Ab/ch7o1v0001/sgtable7o1o221/ (accessed Feb 2013)

Johnsson, M., Lemmens, P.; Handbook of Magnetism and Advanced magnetic Materials, [Online] **2007**, 1-11

Johnsson, M., Lemmens, P.; *J. Phys. Condens. Matter* **2008**, 20, 264001-264006

Keester, K. L., White, W. L.; *J. Solid State Chem.* **1970**, 2, 68

Korolkov D.V., Kostikova G.P., Kostikov Y.P.; *Physica C* **2002**. 383, 117-121

Levy, M.; Ph.D. Thesis, Imperial College, London, United Kingdom, **2005**

Ritter, H., Ihringer, J., Maichle, J.K., Prandl, W., Hoser, A., Hewat, A.W.; *Z. Phys B – Condensed Matter* **1989**, 75, 297-302

Ropp, R.; Encyclopedia of the Alkaline Earth Compounds; Newnes, **2012**; 475-478

Shannon, R.D.; *J. Solid State Chemistry* **1971**, 3, 184-185

Thornton, G., Jacobson, A.J.; Mat. Res. Bull. **1976**, 11, 837-842

Chapter Seven: Conclusions

The main aim of this study was to use in situ PXRD to study the thermoresponsive behavior of a niobium tungstate, tantalum tungstates and barium plumbate. We have successfully done this for the three groups of selected mixed metal oxides.

The niobium tungstate ($Nb_{6.7}W_{10.3}O_{47}$) was synthesized using a precipitation reaction and heat treatment from $NbCl_5$ and H_2WO_4. $Nb_{6.7}W_{10.3}O_{47}$ was formed and then analyzed using in situ PXRD. COXA analysis showed that the crystallization of $Nb_{6.7}W_{10.3}O_{47}$ initiated at 770 ˚C. Positive thermal expansion was observed in the a and b axis direction while the c axis direction was found to undergo negative thermal expansion. The overall percentage change in the a, b and c lattice parameters is 0.43%, 0.37% and -0.21% respectively. It was found that $Nb_{6.7}W_{10.3}O_{47}$ possesses low positive thermal expansion with a mean volumetric coefficient of thermal expansion (CTE) of 6.704×10^{-6} ˚C^{-1}. $Nb_{6.7}W_{10.3}O_{47}$ does not undergo any phase changes within the temperature range 30 ˚C to 900 ˚C. Possible PDF scattering studies can be done on the sample at these lower temperatures to investigate the local order present in the amorphous precursor.

The tantalum tungstates, $Ta_{14.8}W_{1.2}O_{46}$ and $Ta_{16}W_{18}O_{94}$, were synthesized using a precipitation reaction and heat treatment from $TaCl_5$ and H_2WO_4. Ex situ study showed

that at 900 ˚C, the reaction precipitate had fully converted to the desired crystalline product. In situ PXRD study, of the 900 ˚C ex situ heat treated sample, was used to analyze the product which was found to contain both the $Ta_{14.8}W_{1.2}O_{46}$ and $Ta_{16}W_{18}O_{94}$ phases. Both phases were found to possess low positive thermal expansion. Rietveld refinement of $Ta_{14.8}W_{1.2}O_{46}$ involved use of its cif file which showed the overall percentage change in the a, b and c lattice parameters as 1.25%, 0.21% and 0.39% respectively. Rietveld refinement of $Ta_{16}W_{18}O_{94}$ used the “hkl phase” approach which showed the overall percentage change in a, b and c lattice parameters as 0.68%, 0.68% and -0.47%. Though there was some thermal contraction in the c lattice parameter, it wasn’t sufficient to overcome the thermal expansion in the a and b lattice parameters. Therefore the mean volumetric coefficients of thermal expansion (CTEs) for $Ta_{14.8}W_{1.2}O_{46}$ and $Ta_{16}W_{18}O_{94}$ are 2.101 x 10-5 $˚C^{-1}$ and 9.851 x 10-5 $˚C^{-1}$ respectively. No phase changes were observed within the 30 ˚C to 900 ˚C temperature range used for the analysis. The CTE value reported for $Ta_{16}W_{18}O_{94}$ is based on Rietveld refinement of the hkl phase values and not on the crystal structure. Possible investigation into solving for the structure of the $Ta_{16}W_{18}O_{94}$ and calculation of its CTE and porosity can be done.

Barium plumbate, $BaPbO_3$, was studied to determine the temperature at which phase transitions occur, and the structural symmetries. This was essential to resolve the contradictions in the reported results observed by other research groups. It was found that $BaPbO_3$ undergoes two phase transitions within the 30 ˚C to 550 ˚C temperature range. $BaPbO_3$ goes from orthorhombic Imma to I4/mcm to cubic Pm-3m. The two

phase transitions occur at 270 ˚C and 390 ˚C. The results obtained agree with Hester's group (2002), at 275 ˚C, for the temperature of the first phase transition and with Fu's group (2007), at 400˚C for the temperature of the second transition. Results were obtained at the very limit of the information that can be obtained from the Bruker D8 Advance. Possible further investigation can be done using more powerful and advanced instrumentation like a synchrotron.

Appendices

Files on the disc accompanying this dissertation:

- 0514016J_Dissertation.pdf
- d8_12_46.raw (Data for $Nb_xW_yO_z$)
- d8_12_35.raw (Data for $Ta_xW_yO_z$)
- d8_12_31.raw (Data for $BaPbO_3$)